

**USE AND DEVELOPMENT OF A CW TITANIUM
SAPPHIRE LASER FOR NONLINEAR OPTICS**

Sara Shepherd

**A Thesis Submitted for the Degree of PhD
at the
University of St Andrews**



1994

**Full metadata for this item is available in
St Andrews Research Repository
at:**

<http://research-repository.st-andrews.ac.uk/>

Please use this identifier to cite or link to this item:

<http://hdl.handle.net/10023/9931>

This item is protected by original copyright

Use and Development
of a CW Titanium Sapphire Laser
for Nonlinear Optics

A thesis presented by
Sara Shepherd
to the
University of St. Andrews
in application for the degree of
Doctor of Philosophy
September 1993

Declaration

I, Sara Shepherd, hereby certify that this thesis has been composed by myself, that it is a record of my own work, and that it has not been accepted in partial or complete fulfilment of any other degree of professional qualification. I was admitted to the Faculty of Science of the University of St. Andrews under Ordinance General No. 12 on 1st October 1989 and as a candidate for the degree of Ph.D on 1st October 1990.

Sara Shepherd
September 1993

I hereby certify that the candidate has fulfilled the conditions of the Resolution and Regulations appropriate to the Degree of Ph.D.

Dr. B D Sinclair
September 1993

In submitting this thesis to the University of St. Andrews I understand that I am giving permission for it to be made available for use in accordance with the regulations of the of the University Library for the time being in force, subject to any copyright vested in the work not being affected thereby. I also understand that the title and abstract will be made and supplied to any bona fide library or research worker.

Abstract

A cw titanium sapphire laser pumped by an argon ion laser was used for experiments both in second harmonic generation using a non-linear crystal and for sum-frequency generation in an atomic vapour. In addition the laser was stabilised to sub-MHz levels.

Using a crystal of potassium niobate (KNbO_3), the Ti:sapphire laser was frequency doubled over the range 860nm-905nm using an intracavity scheme. The crystal was temperature tuned to achieve near non-critical phase-matching and powers of up to 50mW were obtained, with a constant conversion efficiency per Watt over the doubling range. The thermal properties of potassium niobate in frequency doubling were examined and the effect of the crystal on the ring cavity during temperature tuning was investigated.

The laser cavity was frequency stabilised using a 'side of fringe' locking scheme with a confocal Fabry-Perot etalon as the reference discriminator. The cavity length control elements were two Brewster-angled tilt plates and a piezo mounted mirror. Using this scheme the frequency noise was reduced from tens of MHz to 550kHz. Methods of obtaining a 30GHz frequency scan were also evaluated and an experimental 10GHz scan achieved. It was concluded that only dither and lock schemes are good enough to achieve reliable 30GHz scans.

Using both a Ti:sapphire laser and a dye laser, two contrasting schemes for sum-frequency generation in sodium vapour were investigated, in which a magnetic field was used to break the symmetry of the medium. Using one of these resonantly enhanced routes, powers of $17\mu\text{W}$ in the UV were obtained from a classically 'forbidden' quadrupole transition. The effects of phase-matching on each of the transitions was examined in detail, and it was found that in general there are at least six factors which affect the phase-matching behaviour of the frequency mixing scheme. It was also found that on the route which had two sources of dispersion there was a significant distortion of the output line profiles at high temperatures due to a variation in phase-matching across the line profile itself.

Acknowledgements

I wish to thank my supervisor, Bruce Sinclair, for his encouragement and enthusiasm during this work. I would also like to thank Prof. Malcolm Dunn and Richard Moseley for all the discussions and suggestions. There are many others who helped along the way and my thanks go to them, including; Bill Sleat, the Workshops both mechanical and electrical, Fritz, Miles Padgett and Ian Botheroyd.

In particular I would like to thank my office and lab mates; Gordon, Neil and Richard, and including the interloper, Angus, for withstanding the fan heater and decorating my life - literally and figuratively. Also, the combined D and W Squads for their general good humour and sundry equipment. And finally, both my family and Christian for always being supportive.

Table of Contents

Chapter 1 - Introduction	1
References.....	8
Chapter 2 - Theory of Second Harmonic Generation and Frequency Stabilisation	10
Second Harmonic Generation	10
Intensity Dependence.....	13
Phase-Matching.....	14
Birefringent Crystals.....	15
Length Dependence	21
Effective Non-Linear Coefficient, d_{eff}	23
Conclusions.....	26
Frequency Stabilisation	27
Passive Stabilisation.....	28
Active Stabilisation.....	29
Discriminators.....	29
Cavity Length Control Elements	32
Control Electronics	34
References.....	35
Chapter 3 - Equipment and Laser Development	37
Titanium Sapphire Laser.....	37
Tuning Equipment	40
Stabilisation Equipment.....	42
Second Harmonic Equipment.....	46
Ancillary Equipment.....	49
References.....	50
Chapter 4 - Intracavity Second Harmonic Generation of a Ti:Sapphire Laser using Potassium Niobate	51
Phase-Matching in Potassium Niobate	53
Refractive Indices and Temperature Tuning.....	56
Acceptance Bandwidths.....	59
Changes in Power with Angle.....	60
Changes of Power with Frequency/Wavelength.....	62
Changes of Power with Temperature.....	62

Table of Contents

Chapter 4 -	Efficiency and Power.....	69
Continued	Power Variations.....	72
	Conclusion.....	74
	References.....	75
Chapter 5 -	Frequency Stabilisation and Scanning of Laser	76
	Frequency Stabilisation	76
	Passive Stabilisation.....	76
	Active Stabilisation.....	78
	Residual Noise Levels.....	80
	Conclusion.....	85
	Laser Scanning	86
	'Dead Reckoning' Method of Scanning.....	87
	Alternative Schemes.....	88
	Conclusion.....	89
	References.....	90
	Circuit Diagrams.....	91
Chapter 6 -	Theory of Sum Frequency Generation in Vapours	93
	Three Wave Mixing in Vapours.....	94
	The Energy Levels of Sodium and their Behaviour in a Magnetic Field.....	96
	Selection Rules.....	105
	Sub-Components of Emission.....	106
	Derivation of Output Power at Sum Frequency.....	109
	The DDQ (3S-3P-3D) Route for Sum Frequency Mixing.....	112
	The DQD (3S-3P-4P) Route for Sum Frequency Mixing.....	121
	Effects of Phase-Matching, Dispersion and Focusing on Output Power.....	122
	Weak/No Focusing.....	123
	Focused Case.....	126
	Conclusion.....	129
	Relations Between Coupling Coefficients.....	130
	References.....	131

Table of Contents

Chapter 7 - Sum Frequency Generation in Sodium Vapour via Two Contrasting Routes	133
Experimental Equipment	133
Wavelengths - Vacuum or Air.....	136
Lineshapes and Power.....	137
Phase-Matching - Focusing and Dispersion Sources.....	143
Effect of Focusing.....	143
Dispersion on Sum Frequency Route	152
Conclusion	155
References.....	156
Conclusion	157
Reference	159

Since the Ti:sapphire laser was first reported in 1982 by Moulton¹ it has rapidly developed from being a novel laser material to one of the essentials of any laser laboratory. The beginnings of the Ti:sapphire laser gave little indication of the importance it would assume. The first system² was pumped by a pulsed Coumarin 504 dye laser operating at 503nm and the poor crystal quality limited both the conversion efficiency to 3% (1mJ out for 36mJ pump), and the tuning range to just 10nm from 750nm to 760nm. Nowadays, however, the tuning range covers more than 400nm between 700nm and 1100nm and output powers range from an average of hundreds of kW's in pulsed operation³ to tens of Watts in continuous wave (cw) operation⁴. The work contained in this thesis looks at the use of a cw Ti:sapphire laser in the field of nonlinear optics. This involves intra-cavity frequency doubling of the laser by use of the nonlinear crystal potassium niobate, stabilisation of the laser frequency by reference to an external cavity, and the use of the Ti:sapphire laser and a dye laser in sum-frequency mixing within an atomic vapour.

The Ti:sapphire laser is one of the most widely tunable lasers available and with its tunability has come a host of applications. This near-infrared range between 660nm and 1180nm was previously only commercially covered by dye laser systems, and to achieve the same tunability four separate dyes were required⁵. Figure 1.1 is a chart of the materials most commonly used to give tunable radiation in the near infrared region. The first two (LiF and NaF) are colour centre lasers⁶, the second two⁷ are alternative transition metal doped materials, and the last four are dye lasers.

Solid state lasers such as the Ti:sapphire laser and the other two popular near-infrared sources Cr:LiSrAlF₆ and Cr:Li:CAF, have obvious advantages over both colour centre and dye lasers in terms of their ease of use. Many colour centre lasers require cooling to cryogenic temperatures to inhibit deterioration of the material and dye lasers are usually poisonous and often have lifetimes of weeks or even hours. In the far infrared and the visible colour centre and dye lasers are still the most standard tunable sources, but in the near infrared the most popular source is the Ti:sapphire laser.

Much of the research into Ti:sapphire laser systems is concerned with the development of ultra-short pulses both for telecommunications and optical switching, in which shorter pulses save both time and money. However Ti:sapphire lasers are

increasingly finding uses in the fields of medicine⁸, material characterisation⁹ and general spectrometry¹⁰.

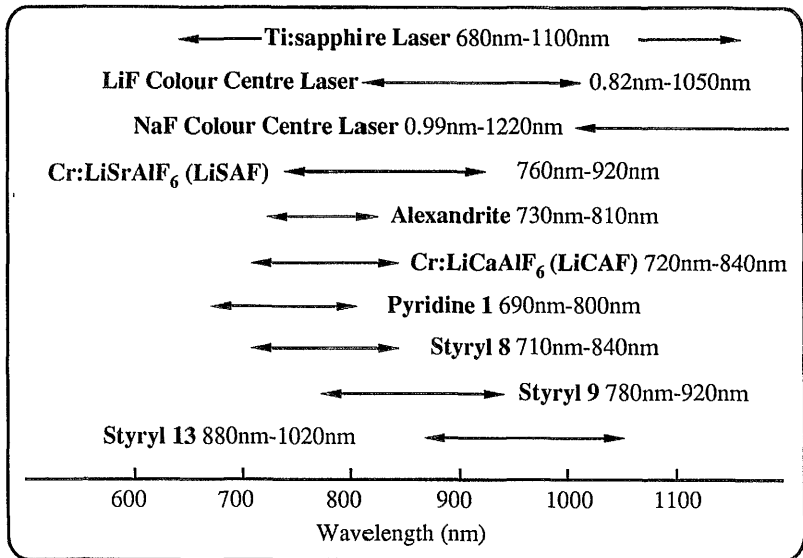


Figure 1.1 - Tunable Lasers in the 700nm - 1100nm region

The Ti:sapphire laser crystal is made by doping small amounts^{11,12} ($2 \cdot 10 \times 10^{18}$ atoms per gram) of the Ti^{3+} ion into a crystal host of sapphire (Al_2O_3). The titanium ion substitutes for aluminium within a surrounding octahedron of oxygen atoms. This crystalline arrangement is shown in figure 1.2.

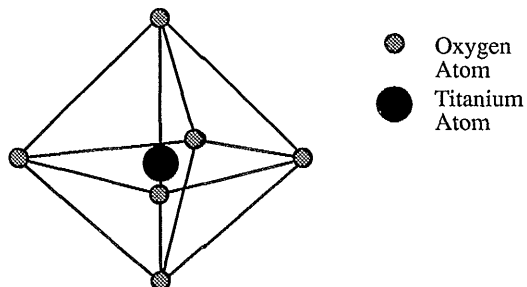


Figure 1.2 - Position of titanium ions within sapphire host (Ti^{3+} substitutes for Al^{3+} to give doped compound $Ti:Al_2O_3$)

Sapphire is an extremely good host for a laser crystal as it is widely transparent, very hard (9 on the Mohs scale on which diamond is 10), a good thermal conductor ($34\text{W/m}^\circ\text{C}$) and has a high thermal stress resistance ($3400\text{W/m}^{1/2}$)¹³. The electronic structure of the Ti^{3+} ion consists of three closed shells and a single electron in the outer d shell. Because this electron is outside the screening effect of the closed shells (unlike that of the Nd^{3+} ion in a Nd:YAG laser) the energy levels of the ion are split by the influence of the crystal's field. When not doped into a crystal the Ti^{3+} ion has five fold degeneracy¹⁴. The crystal splits these degenerate levels into a doublet (excited) and a triplet (ground) state, separated by an energy equivalent to 19000cm^{-1} , which corresponds to blue-green photons. These two levels are each further split by the Jahn-Teller effect^{15,16} in which ionic distortions¹⁷ lift the degeneracy of both the excited and ground states. The magnitude of the splitting of the upper state is 1850cm^{-1} , which is large enough to lead to two overlapping absorption bands. The splitting of the ground state is very much smaller and is classed as a dynamic Jahn-Teller effect, in which the thermal energy of the crystal lattice, $k_{\text{B}}T$, is large enough to cause interchange between the three levels. Each of the five levels corresponds to a different arrangement of the electronic orbitals of the 3d shell of the titanium ion within the crystalline host.

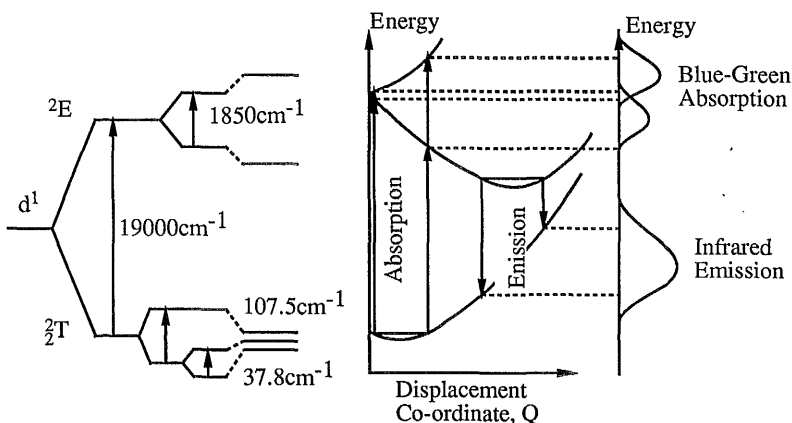


Figure 1.3 - Broadened Energy Levels of Ti^{3+} ion in Crystal Field

For each arrangement of electronic orbitals there is an average displacement of the titanium ion from its nearest neighbours. This displacement is characterised by a displacement co-ordinate, Q . The energy of each level can be approximated by a well in which the minimum energy is at the average displacement, Q_0 . At normal room temperatures several of the vibrational levels of the lattice are excited, and the ions vibrate about the average displacement, so that the displacement at any instant can have

a range of values about the average displacement. The optimum average displacement of the titanium ion from its neighbours changes with a rearrangement of the electronic orbitals, and so the well for each level is displaced in terms of Q from each other level. For the Ti:sapphire levels however the three levels in the ground state are so close they are effectively indistinguishable. The lifting of the degeneracy of the five levels, firstly by the crystal field and secondly by the Jahn-Teller effect, is shown in figure 1.3. This figure also shows the displacement of the energy wells for the two excited states and the three(indistinguishable) ground states.

When the ion emits or absorbs a photon the rearrangement of the electronic orbitals happens much faster than the titanium or oxygen ions can respond. During absorption or emission therefore the displacement co-ordinate is unchanged. This means that although the vibrational energy of the ion at the bottom of the well is within a small thermal range, the corresponding range of displacement values is equivalent to a large range of energies in the final level. This leads to the spread of wavelengths over which absorption can occur. After absorption the ions are not at the lowest energy displacement of the upper level and so lose energy via phonons to the lattice until they occupy the lowest energy position of the excited band. The ions then vibrate about the lowest energy displacement position of the upper level until they emit a photon. As in absorption, the spread of energies in the emitted photons can be large, which leads to the large emission bandwidth of the Ti:sapphire crystal. For the main lasing transition of Ti:sapphire the absorbed photons corresponds to the blue/green part of the spectrum and the emitted photons to the infrared part of the spectrum. (It is also possible to excite fluorescence in the visible part of the spectrum by pumping in the ultraviolet¹⁸, but as this corresponds to the main absorption band of Ti:sapphire these fluorescence bands are of no use as laser transitions.)

The main absorption and emission bands are shown in more detail in figure 1.4. The absorption and emission can be measured for pump light which is polarised either parallel (π) or perpendicular (σ) to the c axis of the Ti:sapphire crystal. The former has roughly twice the absorption of the latter and so is the usual choice for pumping and the one shown in the following figure. This has a double benefit when it comes to using Ti:sapphire as a laser crystal, as the crystal is birefringent and only orientation of the polarisation along the c axis eliminates waveplating action¹⁹. It can be seen that the peak of absorption is centred around 490nm. This makes Ti:sapphire ideal for pumping by blue/green laser sources such as the argon ion laser, dye and frequency-doubled Nd:YAG laser^{2,20}.

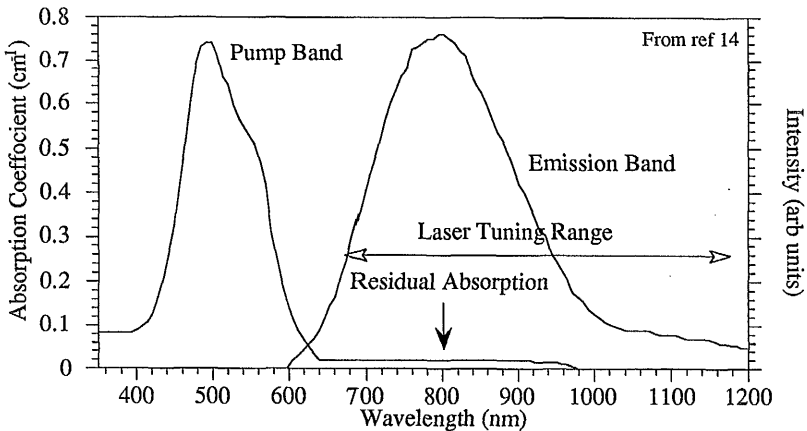


Figure 1.4 - Absorption and emission bands of Ti:sapphire

Although the major absorption band of Ti:sapphire lies in the blue-green part of the spectrum, there is also a small residual absorption in the infrared²¹. This residual absorption has been the focus of most of the work on developing Ti:sapphire laser crystals. It can be characterised by a commonly used figure of merit (FOM), which is given by the ratio of the absorption in the main absorption band to that in the infrared. (The wavelength of absorption in the visible is slightly different depending on the researcher. Rapoport et al^{22,23} define the FOM as $\frac{\alpha_{532}}{\alpha_{800}}$, which will always be slightly smaller than that defined by Alfrey²⁴, $\frac{\alpha_{514}}{\alpha_{800}}$ or Harrison²⁵, $\frac{\alpha_{490}}{\alpha_{800}}$). The residual absorption is known to be caused by the inclusion of small amounts of Ti⁴⁺ within the crystal during doping. The absorption is not however due to just the Ti⁴⁺ ions, but is caused by the formation of Ti³⁺ - Ti⁴⁺ pairs and reaches its maximum when there are equal amounts of each present in the crystal. The earliest growth techniques were the Czochralski and Heat Exchange Methods^{18,23} the first of which involves pulling a crystal from a melt and the second a direct solidification technique. To overcome the problems caused by the residual infrared absorption the Lincoln Laboratories developed a Vertical-Gradient Freeze Technique^{14,21} in which the smaller residual absorption is further improved by annealing the resulting crystal in a chemically reducing atmosphere such as hydrogen.

The absorption at the lasing wavelengths makes cw operation of a Ti:sapphire laser difficult. Lasing was initially observed only at liquid nitrogen temperatures². By use of the VGF technique to reduce the residual absorption, true room temperature cw operation was observed for the first time in 1986²⁶. An additional problem was encountered when trying to use a flashlamp as the pump source, as the energy absorbed by the crystal with a spectrally broad flashlamp was too low to allow the gain of the

cavity to exceed the losses. Indeed, flashlamp pumping was only achieved when a dye was used as a fluorescent converter, in which the dye absorbs the broadband flashlamp radiation and re-radiates most of the energy at the peak of the Ti:sapphire absorption²⁷. The problem with the low gain lies in the upper state lifetime, which at $3.2\mu\text{s}$ ²⁸ is $\frac{1}{70}$ that of Nd:YAG. This, despite a gain cross-section, σ , of between^{29,23} 3 and $3.8 \times 10^{-19}\text{cm}^2$, makes achievement of a population inversion relatively difficult, which is why most pumping of Ti:sapphire lasers is by another laser source. The upper state lifetime, τ , decreases sharply around room temperature due to thermal quenching so most crystals are cooled by contact with a water cooled conducting surface. Ti:sapphire itself has the same thermal conductivity as sapphire which, at $34\text{W/m}^\circ\text{C}$, is larger than many other crystal hosts. The temperature change of the upperstate lifetime is shown in figure 1.5.

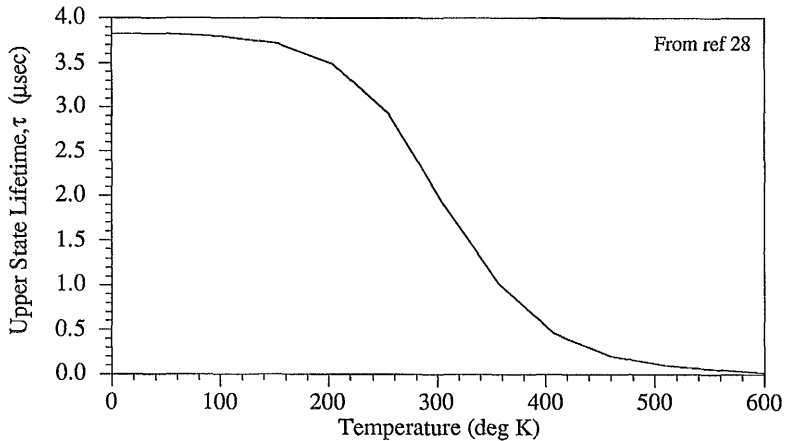


Figure 1.5 - Temperature Dependence of Upper State Lifetime, τ

Even though the upper state lifetime is small the conversion of energy from the visible to the infrared as expressed by the quantum efficiency, η , is excellent and is typically around 74%²⁸. It was therefore not long before high power, single longitudinal mode, cw Ti:sapphire lasers began to appear³⁰. Most of the subsequent work on cw Ti:sapphire lasers has been on stabilisation, frequency conversion and applications and it is these topics which are the subject of this thesis.

Although this work is solely concerned with continuous wave Ti:sapphire lasers, no introduction to the Ti:sapphire laser can fail to mention the work done in ultra-short-pulse laser systems. The exceptionally large gain bandwidth is a dream come true for researchers working on the generation of ultra-short pulses. Since the discovery in 1990 that Ti:sapphire lasers will self-mode-lock³¹, this technique has become the standard

and is responsible for the shortest pulses³², 11fsec, generated by any laser system to date.

A summary of some of the properties of Ti:sapphire lasers is given in Table 1.1.

Emission Cross-section	$3 \times 10^{-19} \text{ cm}^2$	Absorption Cross-section	$9.3 \times 10^{-20} \text{ cm}^2$
Quantum Efficiency	74 %	Lifetime	3.2 μs
Gain Peak	800 nm	Absorption Peak	490 nm
Absorption Coefficient (dependent on ion conc)	2-3 cm^{-1} (typ) up to 5 cm^{-1}	Refractive Index Change dn/dt	$+1.6 \times 10^{-6} / ^\circ\text{C}$
Refractive Index	1.76	Thermal Conductivity	34 $\text{W/m}^\circ\text{C}$
Fracture Toughness	2.2 $\text{MPa/m}^{1/2}$	Thermal Stress Resistance	3400 $\text{W/m}^{1/2}$

Table 1.1 - Properties of Ti:sapphire Lasers

The work described in the following chapters is concerned with the development and use of a cw Ti:sapphire laser in nonlinear optics. There have been three main parts to the work: the first involves using a nonlinear crystal to frequency double the laser; the second involves methods of stabilising and scanning the laser cavity; and the third is the use of the Ti:sapphire laser and a dye laser in a detailed study of sum-frequency conversion in an atomic vapour.

The next chapter of this thesis examines the general theory behind frequency conversion in nonlinear crystals, and the various experimental parameters which have to be optimised to ensure efficient conversion of energy from one frequency to another. This chapter also looks at some of the ways to stabilise the output of a laser so that the frequency deviations are kept to sub-MHz levels to allow more accurate spectroscopic measurements to be taken. The third chapter describes the equipment used in the experiments, and the modifications necessary to allow both intracavity second harmonic generation and also stabilisation and scanning of the laser cavity. The fourth and fifth chapters then describe the experimental work and results for intracavity second harmonic generation and stabilisation of the laser. Finally, the laser was used for an extended series of experiments into frequency mixing in an atomic vapour and the theory and results are presented in chapters six and seven respectively. The results contain a comparison between two quite different resonant enhancement routes within the atomic energy levels in the vapour, and a study of the bulk effects of phase-matching on each of the two routes.

References

- 1 P Moulton - Optics News, Nov/Dec, pg. 9, 1982
- 2 P F Moulton - Spectroscopic and laser characteristics of Ti:Al₂O₃ - J. Opt. Soc. Am. B, Vol. 3, No. 1, pgs 125-132, 1986
- 3 B E Lemoff and C P J Barty - Generation of high-peak-power 20-fsec pulses from a regeneratively initiated, self-mode-locked Ti:Sapphire laser - Opt. Lett, Vol. 17, No. 19, pgs 1367-1369, 1992
- 4 G Ebert et al - 43-W cw Ti:Sapphire laser - Paper CThH4, CLEO Technical Digest, Vol. 10, pgs 390-392, 1991
- 5 Ti:Sapphire is moving onto dye-laser territory - Laser Focus World, pg 23, 1989
- 6 Tunable Lasers - Editor: L F Mollenauer, Springer-Verlag, Berlin, 1987
- 7 Tunability makes vibronic lasers versatile tools - Laser Focus World, Vol. 28, No. 10, pgs 93 - 103, 1992
- 8 K S Frederickson et al - Precise Ablation of skin with reduced collateral damage using the femtosecond-pulsed, Terrawatt Titanium laser - Archives of Dermatology, Vol. 129, No. 8, pgs 989-993, 1993
- 9 Z X Jiang et al - Laser Characterisation of Chromium-doped Forsterite with Ti:Sapphire laser excitation - J. Mod. Opt., Vol. 40, No. 7, pg 1411, 1993
- 10 X Zhan et al - High-Resolution photoacoustic Ti:Sapphire/dye ring laser spectrometer - Rev. Sci. Instrum, Vol. 63, No. 12, pgs 5546-5551, 1992
- 11 R L Aggrawal, A Sanchez et al. - Magnetic and optical measurements on Ti:Al₂O₃ crystals for laser applications: Concentration and absorption cross section of Ti³⁺ ions - Appl. Phys Lett., Vol. 48, NO. 20, pgs 1345-1347, 1986
- 12 A Sanchez, A Strauss et al - Crystal Growth, Spectroscopy, and Laser Characteristics of Ti:Al₂O₃ - IEEE J-QE, Vol. 24, no. 6, pgs 995-1002, 1988
- 13 Encyclopedia of Lasers and Optical Technology - Academic Press Inc, Harcourt Brace Jovanovich Publishers, San Diego, 1991
- 14 K F Wall and A Sanchez - Titanium Sapphire Lasers - The Lincoln Laboratory Journal, Vol. 3, No.3, pgs 447-462, 1990
- 15 B F Gachter and J A Koningsstein - Zero phonon transitions and interacting Jahn-Teller photon energies from the fluorescence spectrum of α -Al₂O₃ :Ti³⁺ - J Chem Phys., Vol. 60, No.5, pgs 2003-2006, 1974
- 16 R R Joyce and P L Richards - Far-Infrared spectra of Al₂O₃ Doped with Ti, V, and Cr* - Phys. Rev. Vol. 179, No. 2, pgs 375-380, 1969
- 17 M C M O'Brien - The Jahn-Teller effect: An Introduction and Current Review - Am. J. Phys, Vol. 61, No. 8, pg 688, 1993

References

- 18 P Lascovara, L Esterowitz and M Kokta - Growth, Spectroscopy and Lasing of Titanium-Doped Sapphire - IEEE J-QE, Vol. QE-21, No. 10, pgs 1614-1618, 1985
- 19 P.F. Moulton - CW Ti:Sapphire Laser Tuning: A Straightforward Task - Photonics Spectra, pp 119-122, March 91
- 20 J M Eggleston - Characteristics and Kinetics of Laser-Pumped Ti:Sapphire Oscillators - IEEE JQ-E, Vol. 24, No. 6, pgs 1009-1015, 1988
- 21 R L Aggrawal, A Sanchez et al - Residual Infrared Absorption in As-Grown and Annealed Crystals of Ti:Al₂O₃ - IEEE J-QE, Vol. 24, No. 6, pgs 1003-1008, 1988
- 22 W R Rapoport and C P Khattak - Efficient, Tuneable Ti:Sapphire Laser - Proc. Top. Meet. Tun. Solid State laser systems, Zigzag, Or., pgs 212-217, Jun 86
- 23 W R Rapoport and C P Khattak - Titanium Sapphire Laser Characteristics - Appl. Opt., Vol. 27, No. 13, pgs 2677-2684, 1988
- 24 J Alfrey - Modeling of Longitudinally Pumped CW Ti:Sapphire Laser Oscillators - IEEE J-QE, Vol. 25, No. 4, pgs 760-766, 1989
- 25 J Harrison, A Finch et al. - A Low-Threshold, CW, All-Solid-State Ti:Al₂O₃ Laser - Opt. Lett., Vol. 16, No. 3, pgs 581-583, 1991
- 26 A Sanchez R E Fahey et al - Room-Temperature continuous-wave operation of a Ti:Al₂O₃ laser - Opt. Lett., Vol. 11, No. 6, pgs 363-364, 1986
- 27 P Lascovara et al - Flash-lamp-pumped Ti:Al₂O₃ laser using fluorescent conversion - Opt. Lett., Vol. 10, No. 6, pgs 273-275, 1985
- 28 P Albers et al - Continuous -Wave laser operation and quantum efficiency of titanium-doped sapphire - J. Opt. Soc. Am. B, Vol. 3, no. 1, pgs 134-139, 1986
- 29 K F Wall - Small-Signal Gain Measurements in a Ti:Al₂O₃ Amplifier - IEEE J-QE, Vol. 24, No. 6, pgs 1016-1020, 1988
- 30 P A Schulz - Single-Frequency Ti-Al₂O₃ Ring Laser - IEEE J-QE, Vol. 24, No. 6, pgs 1039-1043, 1988
- 31 D E Spence, P N Kean and W Sibbett - 60-fsec pulse generation from a self-mode-locked Ti:Sapphire laser - Opt. Lett., Vol. 16, No. 1, pgs 42-44, 1991
- 32 M Asaki et al - Generation of 11-fsec pulses from a self-mode-locked Ti:Sapphire Laser - Opt. Lett., Vol. 18, No. 12, pgs 977-979, 1993

Chapter 2

Theory of Second Harmonic Generation and Frequency Stabilisation

Second Harmonic Generation

Generating the second harmonic of any laser source is one obvious way of extending the wavelength range of that laser. This is particularly useful if no other laser operates well over the second harmonic range. The Ti:sapphire laser gives high cw powers between 700nm and 1.1 μ m, so that second harmonic generation (SHG) can lead to a cw source tuneable between 350nm and 550nm. This range is usually covered by a number of dye lasers, with the associated problems of dye degradation, jitter and the poisonous nature of the dyes themselves. A Ti:sapphire laser with a SHG option could in future be a useful all-solid-state system covering most of the range from the UV to the near-IR. (Conveniently, the gap between 550nm and 700nm is covered by some of the most reliable dyes available, the Rhodamines). The theory behind SHG has been described many times before¹⁻⁵ and will here be discussed only briefly. Instead this chapter explores the more practical aspects involved in obtaining efficient conversion of radiation from the fundamental to the second harmonic.

Second harmonic generation is usually achieved by exploiting the second-order nonlinearity of an optically nonlinear crystal. In order to obtain the best transfer of energy from the fundamental to the second harmonic wave, the two waves must travel with the same phase velocity. As dispersion is itself wavelength dependent this is not generally realisable. However, by using a birefringent crystal the effects of birefringence and dispersion can be balanced against each other to achieve the same phase velocity in both the fundamental and second harmonic waves. This process is called *phase-matching* and is one of the characteristics for which a nonlinear crystal is chosen. For such a widely tuneable source as the Ti:sapphire laser there are a range of different crystals which can be used in SHG, but no single crystal which efficiently covers all wavelengths. In the experimental work described in chapter 4 a crystal of KNbO₃ was used to double the range 860nm to 905nm, but at lower wavelengths this crystal cannot achieve phase-matching and other crystals must be used instead. In the latter part of this thesis is described an investigation of sum frequency generation (SFG) using an atomic vapour. Many of the practical factors are similar although using a strongly quantised medium causes the SFG to vary rapidly as the excitation source is tuned across a resonantly enhancing transition. Both SHG and SFG are types of three-wave mixing. Other types

are difference frequency mixing (DFM) and optical parametric amplification (OPA). The generation of new frequencies comes about from the interaction of the fundamental electro-magnetic waves with the matter through which they are passing.

If one or more electromagnetic (EM) waves pass through a dielectric crystal, the electrons within the crystal are excited into dipole oscillations which themselves generate radiation. The induced polarisation⁶ is given by the following expression:

$$P = \epsilon_0 [\chi^{(1)}E + \chi^{(2)}E^2 + \chi^{(3)}E^3 + \dots] \quad \text{Eqn. (2.1)}$$

The $\chi^{(1)}$ term is the linear susceptibility of the crystal and has physical significance in that it describes the origin of the refractive index of the medium as seen by that field. The $\chi^{(2)}$ term is the second order nonlinearity and describes three wave mixing in which two electromagnetic fields waves produce a third or vice versa. In general $\chi^{(2)}$ is quite small, but by use of the intense electric fields associated with focused laser beams the output at the frequencies generated through $\chi^{(2)}$ interactions can be significant. The factors which affect efficient generation of new frequencies through $\chi^{(2)}$ interactions are the subject of this chapter. Although the emphasis here is on SHG, most of the concepts also apply to SFG, DFG and OPA's. The $\chi^{(3)}$ term is the third order susceptibility and describes such effects as four wave mixing. In the experiments described here this is negligible, as the $\chi^{(3)}$ susceptibilities are extremely small when compared to $\chi^{(2)}$.

For three wave mixing in which two waves combine to produce a third generated wave, the emitted wave has (neglecting higher order susceptibilities) two components, a linear component and a nonlinear component. These are related to the input fields E_1 and E_2 such that :

a)

$$E_3^{(1)} \propto \chi^{(1)} [E_1 e^{i(k_1 x - \omega_1 t)} + E_2 e^{i(k_2 x - \omega_2 t)} + \text{complex conjugates}] \quad \text{Eqn. (2.2)}$$

This is the linear term proportional to $\chi^{(1)}$. It has both a real and an imaginary part. The real part describes the dispersion of the two waves by the medium, and the imaginary part the absorption (or gain) as they propagate.

b) The nonlinear term is given by:

$$\begin{aligned} E_3^{(2)} \propto \chi^{(2)} [& E_1 \cdot E_1 e^{2i(k_1 x - \omega_1 t)} + E_2 \cdot E_2 e^{2i(k_2 x - \omega_2 t)} + E_1 \cdot E_1^* + E_2 \cdot E_2^* + \\ & 2E_1 \cdot E_2 e^{i([k_1 + k_2]x - [\omega_1 + \omega_2]t)} + 2E_1 \cdot E_2^* e^{i([k_1 - k_2]x - [\omega_1 - \omega_2]t)} + \\ & 2E_1^* \cdot E_2 e^{-i([k_1 + k_2]x - [\omega_1 - \omega_2]t)} + 2E_1^* \cdot E_2^* e^{-i([k_1 - k_2]x - [\omega_1 - \omega_2]t)}] \end{aligned} \quad \text{Eqn. (2.3)}$$

These derivations are described in more detail in texts⁷ but it can be seen that there are four main parts to the generated wave, whose frequencies are given below:

- | | |
|---|--|
| a) $\omega_3=2\omega_1$
$\omega_3=2\omega_2$ | Second Harmonic Generation
of Input Waves |
| b) $\omega_3=0$ | Optical Rectification |
| c) $\omega_3=\omega_1+\omega_2$ | Sum Frequency Mixing |
| d) $\omega_3=\omega_1-\omega_2$ | Difference Frequency Mixing |
- Eqn. (2.4)

These are the components which are proportional to the nonlinear susceptibility, $\chi^{(2)}$. Not all media have a $\chi^{(2)}$ component. In general only those media which are non-centrosymmetric allow three-wave interactions. (This is always true and in chapters six and seven are described the theory and experimental results of a sum frequency generation in an atomic vapour in which the symmetry of the vapour system is broken by the application of a magnetic field). In a nonlinear medium the polarisation of the waves produced by the oscillating dipoles is not linearly dependent on the exciting waves and a frequency analysis of the output gives the four components listed above.

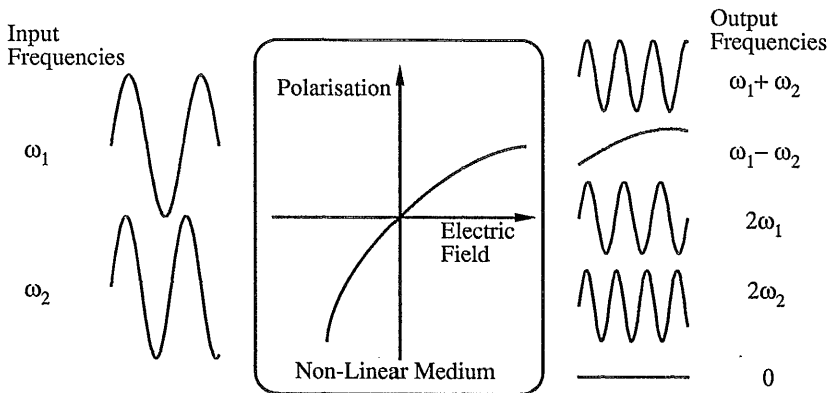


Figure 2.1 - Frequency Conversion by Nonlinear Material

Although all of the effects described above occur whenever two waves pass through a nonlinear material, often only those dependent on the linear susceptibility

(dispersion and absorption) are strong enough to be observed. The strength of the nonlinear conversion depends on a number of variables and the importance of each of these is described below for the particular case of second harmonic generation. In SHG the two input waves are identical and the power generated in the absence of pump depletion is given by the expression:

$$P_{2\omega} = \frac{2\omega^2 d_{\text{eff}}^2 \ell^2 P_{\omega}^2 \text{Sinc}^2(\Delta k \ell / 2)}{\pi w_0^2 \epsilon_0 n_{\omega}^2 n_{2\omega} c^3} \quad \text{Eqn. (2.5)}$$

where the different components given are as follows:

- $P_{2\omega}$ = Power at second harmonic frequency, 2ω
- d_{eff} = effective nonlinear coefficient
- ℓ = length of medium (or effective length if appropriate)
- P_{ω} = Power at fundamental frequency, ω
- Δk = phase mismatch ($k_{2\omega} - 2k_{\omega}$)
- w_0 = waist size of fundamental beam
- ϵ_0 = permittivity
- n_{ω} = refractive index experienced by fundamental wave
- $n_{2\omega}$ = refractive index experienced by second harmonic wave
- c = speed of light in vacuum

This expression has been theoretically derived in detail in many texts and will be discussed here only in terms of the physical significance of the various factors affecting the second harmonic power when choosing the best material for frequency conversion.

Intensity dependence

From equation 2.1 it can be seen that the polarisation(**P**), and hence the amplitude(**E**), of the wave generated by three wave mixing is proportional to the square of the fundamental amplitude. The output power at the second harmonic is therefore dependent on the square of the fundamental power and this leads to the P_{ω}^2 term in the SH power equation. As this generated power is also proportional to $(\pi w_0^2)^{-1}$, which is the area into which the fundamental beam is focused, the conversion efficiency from the fundamental to the second harmonic($P_{2\omega}/P_{\omega}$) is directly proportional to the fundamental intensity within the beam. At first it may seem that even a low powered source can give comparable output powers to that of a higher powered source, provided it is focused tightly enough. In practice there is a limit as to how tightly a Gaussian beam can be focused before the resulting divergence of the beam limits the effective interaction length of the medium (these limitations are discussed later in this chapter). For this reason SHG is often enhanced by placing the nonlinear medium either inside the laser cavity or in an

external resonant cavity. In either case the fundamental power passing through the medium is greatly increased, resulting in more efficient SH conversion.

Phase-Matching

The term $\text{Sinc}^2(\Delta k \ell / 2)$ reflects the effect of phase-matching upon the second harmonic power. Although, by the conservation of energy, there is a strict relation between the frequencies such that $\omega_2 = 2\omega_1$, the wavevectors of the three waves are dependent on the refractive index of the medium, which is itself frequency dependent. In general this means that the two waves travel with different phase velocities, and the phase difference between the fundamental and second harmonic changes as the beams propagate through the medium. This rate at which the phase difference changes is called the phase mismatch and is measured by the value of $k_{2\omega} - 2k_{\omega} = \Delta k$. Initially the fundamental will convert to the SH by the dipole oscillations described above and the phase between the two is fixed to maximise this conversion. However, the process can work both ways and as the beams propagate through the crystal and the phase difference shifts, the conversion from ω to 2ω becomes less favourable while that from 2ω to ω increases. This results in a decrease of the SH power generated from the maximum possible and gives rise to the distinctive $\text{Sinc}^2(\Delta k \ell / 2)$ behaviour. For a fixed (non-zero) Δk value the term $\text{Sinc}^2(\Delta k \ell / 2)$ is at a maximum when $\ell = 0$. As the power is also directly proportional to ℓ^2 as well as $\text{Sinc}^2(\Delta k \ell / 2)$, a variation in ℓ alone produces a Sin^2 variation rather than the Sinc^2 variation produced by altering Δk . Figure 2.2 shows the dependence of the SH power on the crystal length and the regions for which forward and back conversion dominate.

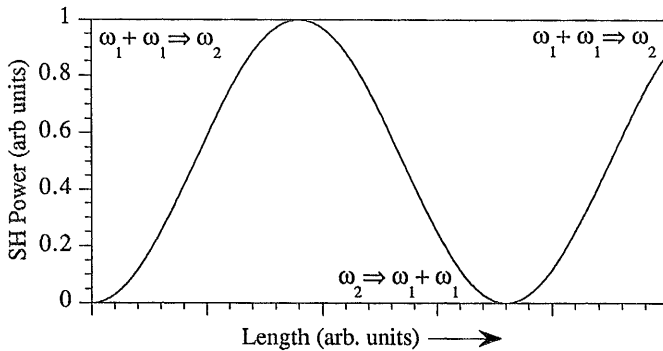


Figure 2.2- Length Dependence of Second Harmonic Power when not Phase -Matched

In order to keep the phase shift between the two waves constant along the length of the nonlinear medium the value of Δk must be zero. This is usually attempted by use of a birefringent crystal. In a birefringent material the refractive index is dependent on the direction of polarisation as well as wavelength and so it is possible to offset one effect by use of the other. In refractive index terms the phase mismatch condition Δk is given by:

$$\Delta k = k_{2\omega} - 2k_{\omega} = \frac{2\pi n_{2\omega}}{\lambda_{2\omega}} - 2 \frac{2\pi n_{\omega}}{\lambda_{\omega}} = \frac{4\pi}{\lambda_{\omega}} (n_{2\omega} - n_{\omega}) = \frac{4\pi}{\lambda_{\omega}} \Delta n.$$

The choice of crystal is determined by the wavelength of the fundamental as each crystal can only achieve phase matching over a limited range, not all of which will give a good conversion efficiency. Figure 2.3 shows the variation in second harmonic power as the refractive index difference varies for a 1cm long medium at $\lambda=800\text{nm}$.

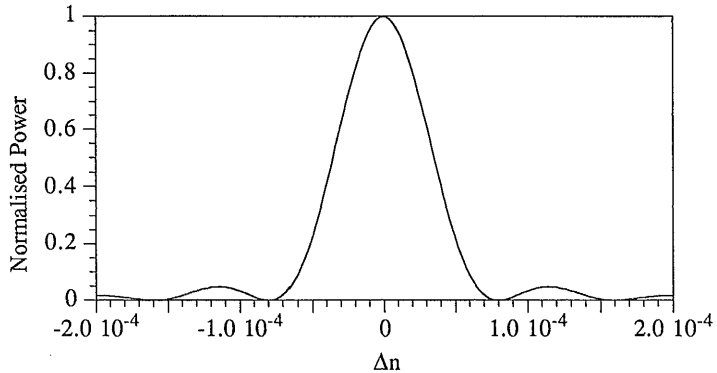


Figure 2.3 - Power Variation with Refractive Index Mismatch

The factors which can change the value of Δn from perfect phase-matching include the wavelength, the crystal temperature and the angle of propagation to the crystal's axes. The amount each of these factors can change before the second harmonic power drops to half its maximum value is called the acceptance bandwidth and is dependent on the crystal used.

Birefringent Crystals

To be able to equalise the refractive indices of the two waves it is necessary to know the crystal's refractive index for any polarisation and wavelength. The refractive indices of the crystal are specified for each of the axes within the crystal, which are usually labelled 1,2,3 or a,b,c or x,y,z. (It is not necessarily true that the conventions are related such that 1=a=x, but by convention n_y never has either the largest or smallest

refractive index). The variation of the three refractive indices, n_x , n_y , and n_z , with wavelength(λ) are given by the Sellmeier equation which is generally of the form:

$$n_i^2(\lambda) = 1 + \frac{S_1 \lambda_1^2}{1 - \left(\frac{\lambda_1}{\lambda}\right)^2} + \frac{S_2 \lambda_2^2}{1 - \left(\frac{\lambda_2}{\lambda}\right)^2} \quad (i = x, y \text{ or } z) \quad \text{Eqn. (2.6)}$$

where S_1 , S_2 , λ_1 and λ_2 are constants, specific to each crystal. Each material has a unique Sellmeier equation which is given in the data for that crystal.

If two of the three refractive indices are the same then the crystal is uniaxial (it has one optic axis), if all are different it is a biaxial crystal. An optic axis is a direction of propagation for which the refractive index is independent of the direction of polarisation. (Biaxial crystals are the general case and have two optic axes. Uniaxial crystals are a special case where the two optic axes coincide.) For phase matching to occur the fundamental must propagate at an angle to the optic axes or the refractive indices at the fundamental and second harmonic cannot be matched. The refractive index experienced by a wave propagating off the optic axis is illustrated by means of the index ellipsoid. Figure 2.4 shows the ellipsoids of both biaxial and uniaxial crystals. The optic axes are always in the x-z plane, at equal angles to the z axis.

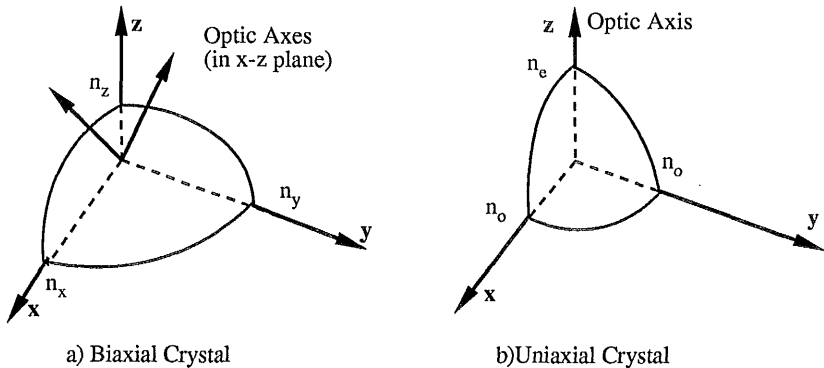


Figure 2.4 - Index Ellipsoids

For any arbitrary wave propagating through the crystal the polarisation can be split into two possible components- the extraordinary component, (e), and the ordinary, component, (o). In a uniaxial crystal where two of the axes have the same refractive index, (Fig 2.4b), the o-wave axis is defined as being in the plane defined by these axes, and the e wave is at right angles to the o wave and to the propagation direction. In a biaxial crystal the terms e and o do not really apply, but the terminology has been

transferred and redefined such that an o-wave is one which is polarised along a principal axis and an e-wave is one which is polarised in a principal plane (a plane defined by two of the principal axes). Figure 2.5 shows the polarisation of some arbitrary wave propagating through a biaxial crystal.

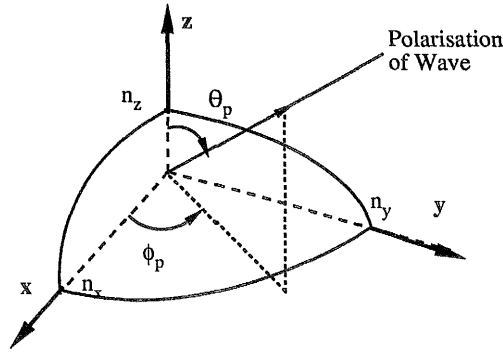


Figure 2.5 - Refractive Index Components of Wave

The surface of the ellipsoid is given by the standard equation:

$$\frac{x^2}{n_x^2} + \frac{y^2}{n_y^2} + \frac{z^2}{n_z^2} = 1 \quad \text{Eqn. (2.7)}$$

where x,y, and z are the three refractive index components along the three axes.

The overall refractive index of the wave, n, is $\sqrt{x^2+y^2+z^2}$, and the components along the three axes are: $x=nsin(\theta_p)cos(\phi_p)$, $y=nsin(\theta_p)sin(\phi_p)$, and $z=ncos(\theta_p)$. The refractive index of the wave, $n(\theta_p, \phi_p)$ is therefore given by the general expression:

$$\frac{1}{n^2(\theta_p, \phi_p)} = \frac{\sin^2(\theta_p)\cos^2(\phi_p)}{n_x^2} + \frac{\sin^2(\theta_p)\sin^2(\phi_p)}{n_y^2} + \frac{\cos^2(\theta_p)}{n_z^2} \quad \text{Eqn. (2.8)}$$

For a uniaxial crystal there is no ϕ dependence and so the general case shown in fig 2.5 can be represented by a two dimensional diagram showing just the θ refractive index dependence (fig 2.6). The figure shows the index surfaces for the extraordinary and ordinary polarisations of a wave propagating at an angle θ to the optic axis. (Note that this θ is at 90° to that of fig 2.5 as it is for the direction of propagation not the polarisation)

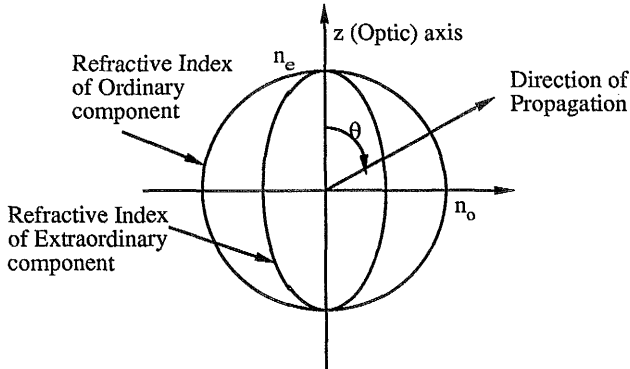


Figure 2.6 - Index Surfaces for a (negative) Uniaxial Crystal

In a positive uniaxial crystal $n_e > n_o$, and in a negative uniaxial crystal $n_e < n_o$. (In biaxial crystals the terms negative and positive refer to whether the angle between the optic axes is greater than or less than 90° .) It can be seen that the ordinary component is independent of θ whereas the extraordinary component is described by equation 2.8 (with ϕ set to 0 degrees and $\theta = \theta_p + 90^\circ$) to give the simpler expression:

$$\frac{1}{n^2(\theta)} = \frac{\cos^2(\theta)}{n_o^2} + \frac{\sin^2(\theta)}{n_e^2} \quad \text{Eqn. (2.9)}$$

With a biaxial crystal there is the additional ϕ dependence, but for each value of ϕ a similar diagram can be constructed where the o-wave has a constant value (being fixed to an axis) and the e-wave refractive index describes an ellipse which varies with θ .

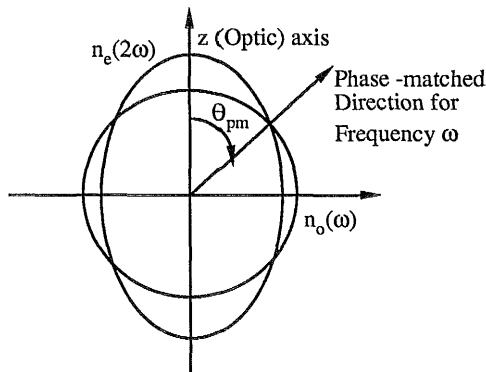


Figure 2.7 - Phase-Matched Angle

Figure 2.7 illustrates how the refractive indices for the fundamental and second harmonic can be equalised provided that they are not both ordinary or extraordinary (in which case the two index surfaces never cross). The case illustrated is for a negative uniaxial crystal. The angle at which $n_{2\omega} = n_{\omega}$ is called the phase match angle, θ_{pm} and can be calculated from eqn (2.9) by setting $n^{\omega}(\theta, \phi) = n_{\omega}^{2\omega}$ to give:

$$\sin^2(\theta_{pm}) = \left(\frac{n_e^{\omega}}{n_o^{2\omega}} \right)^2 \left(\frac{(n_o^{\omega})^2 - (n_o^{2\omega})^2}{(n_o^{\omega})^2 + (n_e^{\omega})^2} \right) \quad \text{Eqn. (2.10)}$$

The general variation of refractive index with the three axes can be represented as shown in figure 2.8.

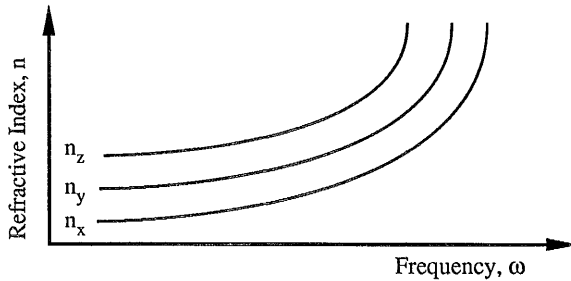


Figure 2.8 -Refractive Index Variation with Frequency
of Positive Biaxial crystal

In this case $n_z > n_y > n_x$ which corresponds to a positive biaxial crystal. (For a positive uniaxial crystal the indices n_x and n_y are equal).

As the fundamental is composed of two of the waves in the three wave interaction, these waves can either be two o-waves, two e-waves or both an o and an e wave together. This is set by the orientation of the fundamental polarisation to the crystal axes. If the two waves are the same then the interaction is said to be of type I, if they are different then they are of type II. It is obviously not possible (fig 2.9) for phase matching to occur if all three waves are of the same type ($e+e \rightarrow e$ or $o+o \rightarrow o$), as then the refractive indices are all on the same curve and so phase-matching does not occur. All three-wave interactions are one of four different types which are given in Table 2.1 for the general case, and also specifically for SHG.

All Three Wave Interactions		SHG	
Type I	Type II	Type I	Type II
o ₁ o ₂ e	e ₁ o ₂ e	o+o → e	e+o → e
e ₁ o ₂ o	o ₁ o ₂ o	e+e → o	o+e → o

Table 2.1 - Wave Configurations in Three Wave Mixing

Figure 2.9 shows the possible interactions for a positive uniaxial crystal. The symbol ● represents the refractive index of each of the three waves, with the value of the refractive index at the fundamental being a combination of two components.

It can be seen that there are only two phase matching options, which apply at the frequencies ω_1 and ω_2 . They are the type I interaction of $e+e \rightarrow o$ and the type II interaction $e+o \rightarrow o$. In a negative uniaxial crystal these two interactions are the unrealisable ones and the phase matching can either be $o+o \rightarrow e$ or $o+e \rightarrow e$. (Note that although the refractive index of the ordinary waves is always equal to n_o , that of the extraordinary waves varies with angle and has a value between n_e and n_o).

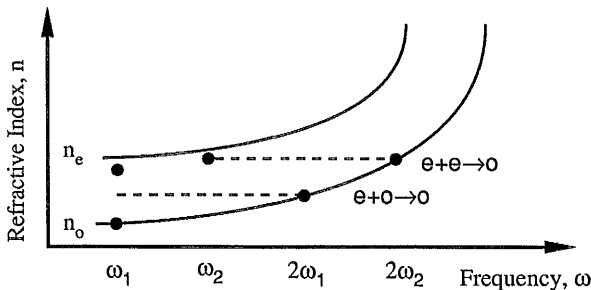


Figure 2.9 - Phase-Matching Options for a Positive Uniaxial Crystal

In a biaxial crystal the phase-matching configuration depends on the plane in which the crystal is being tuned⁸. Once more, of the four possible configurations only two are practically possible in any plane. The configurations are simpler to visualise if one keeps to the principal planes. Figure 2.10 shows these two possibilities for tuning in the z-y plane of a positive biaxial crystal (for a negative biaxial z and x are switched). When tuning in the z-y plane one of the waves must have a component polarised along the x-axis. As this has the smallest value of n it must be at the higher frequency, which sets the SH component as an o wave. The fundamental waves can then be either $e+e$ or $o+e$.

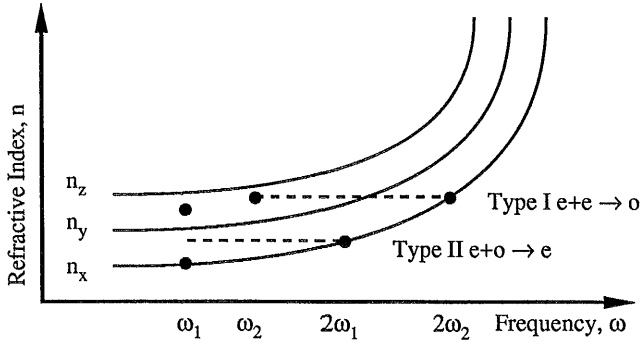


Figure 2.10 - Phase Matching Options for Tuning in z-y Plane of a Positive Biaxial Crystal

Although these are the phase matching options for this plane they will only be phase matched for a limited range of wavelengths, the values of which can be calculated using the Sellmeier equation and equation 2.8. The options for the other two principal planes can be deduced in a similar manner, as can those for a negative biaxial crystal, but off-axis tuning in a biaxial crystal is more complicated and is not used in this thesis. For a description of off-axis phase-matching in a biaxial crystal see reference 8 .

Length dependence

i) Effective length, ℓ_f

As the fundamental beam is focused within the medium, the tighter the focus the greater the effect of diffraction on the beam divergence. If the medium is long compared to the confocal parameter, b , then this leads to an effective length, (ℓ_f) , which is equivalent to the length in which the beam can be considered to be focused¹. This length is given in terms of the confocal parameter, where $\ell_f = \frac{1}{2} \pi b$. The confocal parameter is defined as the length over which the beam has expanded to $\sqrt{2}$ of its focused waist in each direction (fig2.11), and is given by $b = \frac{2\pi w_0^2 n}{\lambda}$, where n is the refractive index of the medium in the phase-matched direction, and λ is the fundamental wavelength.

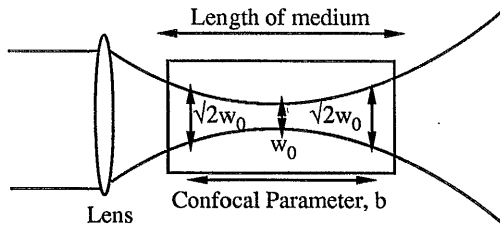


Figure 2.11- Confocal Parameter

Further study by Boyd and Kleinman² showed that the optimum length for a medium which is comparable in length to the confocal parameter is related to the crystal length and confocal parameter such that $l/b=2.8$. The relation l/b is commonly called the focusing parameter and is denoted as ξ . If the length of the medium is smaller than the optimum length then the value of l used in eqn 2.5 is the actual length of the medium, provided that this is longer than the aperture length.

ii) Aperture length

If phase matching ($\Delta k=0$) in the medium is achieved by use of a birefringent material, then the phenomenon of walkoff may occur. For any wave the direction of energy propagation - the Poynting vector - is in the direction normal to the index surface. In an ordinary wave the index surface is circular (fig 2.6) and so the Poynting vector and the direction of phase propagation are the same. For an extraordinary wave, which has an elliptical index surface, the tangent to this surface is not in the direction of phase propagation except when θ is 0° or 90° . This means that for beams phase matched at other angles there will be a gradual separation of the fundamental and second harmonic beams to the extent that they will eventually cease to overlap³. The angle between the Poynting vector and the direction of propagation is called the walkoff angle, ρ , fig(2.12).

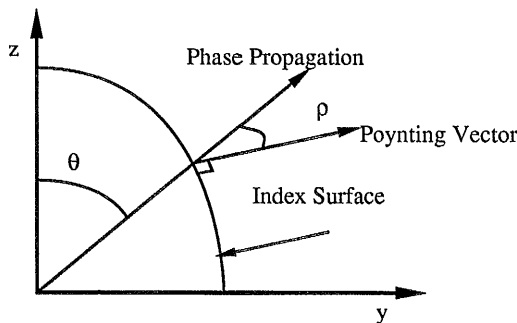


Figure 2.12 - Walkoff Angle

The walkoff angle, ρ , can be found from the expression:

$$\tan(\rho) = \frac{1}{n} \left(\frac{dn}{d\theta} \right) \quad \text{Eqn. (2.11)}$$

Differentiation of eqn. 2.9 and substitution into eqn. 2.11 leads to the following expression for a positive uniaxial crystal:

$$\tan(\rho) = \frac{1}{2} (n_o^\omega)^2 \left(\frac{1}{(n_e^{2\omega})^2} - \frac{1}{(n_o^{2\omega})^2} \right) \quad \text{Eqn. (2.12)}$$

Using the walkoff angle one can find the effective length over which the two beams are close enough to interact. This is also dependent on the waist size to which the beams are focused, as the wavefront curvature is greater the smaller the waist size. This aperture length, ℓ_a , is defined as the distance after which the second harmonic beam just separates from the fundamental beam and is given by the expression:

$$\ell_a = \frac{\omega_o \sqrt{\pi}}{\rho} \quad \text{Eqn. (2.13)}$$

Effective nonlinear coefficient, d_{eff}

The most significant factor to influence the conversion efficiency of the nonlinear interaction is the effective nonlinear coefficient, d_{eff} . This is directly proportional to the second order nonlinearity, $\chi^{(2)}$, such that $d = \frac{1}{2} \chi^{(2)}$. Even if a crystal is perfectly phase-matched there will be no frequency conversion unless d_{eff} has a finite (non-zero) value. Hence the choice of phase-matching geometry is influenced by the directions of propagation within the crystal which maximise the value of d_{eff} . The value of d_{eff} is derived from the \mathbf{d} tensor of that crystal. In general the tensor is represented using the contraction of indices due to Kleinman symmetry⁶. (This contraction holds true provided the frequencies involved are not near any resonances). Using this notation the coefficients are contracted to $d_{111}=d_{11}$, $d_{122}=d_{12}$, $d_{123}=d_{14}$, $d_{113}=d_{15}$, $d_{112}=d_{16}$ etc., such that the tensor can be represented by the matrix given below.

$$d_{\mu\nu} = \begin{pmatrix} d_{11} & \dots & d_{31} \\ \vdots & \ddots & \\ d_{16} & & d_{36} \end{pmatrix} \quad \text{Eqn. (2.14)}$$

For each crystal class there are a number of components of \mathbf{d} that are zero and some which are equivalent to each other. Tables of the \mathbf{d} tensors for each crystal class are readily available. The component symmetries (zero and non-zero components) are the same as in the electro-optic tensors for the crystals, but the components of the \mathbf{d} tensors are the nonlinear coefficients, instead of the electro-optic coefficients. The tensor given below is for the class $mm2$, which includes many of the crystals commonly used in nonlinear optics such as KTP, LiB_3O_5 and KNbO_3 .

$$\mathbf{d}_{\text{tm}} = \begin{pmatrix} 0 & 0 & d_{31} \\ 0 & 0 & d_{32} \\ 0 & 0 & d_{33} \\ 0 & d_{24} & 0 \\ d_{15} & 0 & 0 \\ 0 & 0 & 0 \end{pmatrix} \quad \text{Eqn. (2.15)}$$

By Kleinman symmetry the components d_{31} and d_{15} are equal, as are d_{32} and d_{24} . In terms of calculating d_{eff} , the interactions $o+o \rightarrow e$, $o+e \rightarrow o$, $o \rightarrow o+e$ and $e \rightarrow o+o$ are identical and are all ooe interactions. (The first two are SFM,DFM or SHG interactions and the last two are OPO interactions). There are four similar schemes for the ooe interactions. If the three interacting waves have wave normals \mathbf{k}_a , \mathbf{k}_b and \mathbf{k}_c then the unit vectors of the polarisation of each wave may be written as $\hat{\mathbf{e}}_a$, $\hat{\mathbf{e}}_b$ and $\hat{\mathbf{e}}_c$. Each of these unit vectors has three components along the three axes such that $\hat{\mathbf{e}}_a = (\hat{e}_{a1}, \hat{e}_{a2}, \hat{e}_{a3})$, where the three components are the projections of the unit vector onto the crystal axes 1,2,3 as shown in figure 2.13.

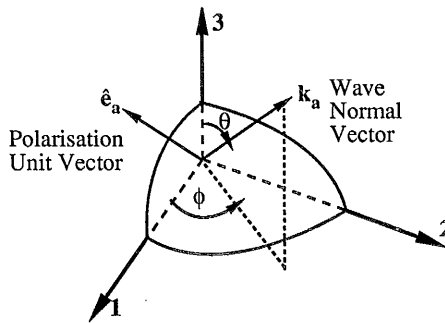


Figure 2.13 - Unit eigenvector projection

The effective nonlinear coefficient, d_{eff} , is given by: $d_{\text{eff}} = (\hat{\mathbf{e}}_a \cdot \mathbf{d}) : \hat{\mathbf{e}}_b \hat{\mathbf{e}}_c$. The values of the unit vector components can be calculated for any angle of propagation within a

biaxial crystal as described in Yao and Sheng⁸. If tuning in a principal plane the expressions once more simplify and the value of d_{eff} can be readily calculated for either ooe or eoo transitions. The effective nonlinear coefficient is given by the expression:

$$d_{eff} = d_{111}\hat{e}_a\hat{e}_b\hat{e}_c + d_{112}\hat{e}_a\hat{e}_b\hat{e}_c + \dots + d_{333}\hat{e}_a\hat{e}_b\hat{e}_c \quad \text{Eqn. (2.14)}$$

The ordering of the waves (abc or acb or cba etc.) does not matter as the value of $d_{113} = d_{131} = d_{311}$. Take, for example, an mm2 crystal in which the fundamental wave propagates in the 1,2 plane and is polarised along the 3 axis. This is an eoo transition. In this case $\hat{e}_b = \hat{e}_c = (0,0,1)$ and $\hat{e}_a = (\cos(\phi), \sin(\phi), 0)$. As several of the coefficients are zero, equation 2.14 reduces to $d_{eff} = d_{31}\hat{e}_a\hat{e}_b\hat{e}_c + d_{32}\hat{e}_a\hat{e}_b\hat{e}_c + d_{33}\hat{e}_a\hat{e}_b\hat{e}_c + d_{24}\hat{e}_a\hat{e}_b\hat{e}_c + d_{15}\hat{e}_a\hat{e}_b\hat{e}_c$. By substitution of the components of the unit vectors into this expression it can be calculated that $d_{eff}=0$ for an ooe transition in the 1,2 plane. For a similar ooe transition, but with tuning in the 1,3 plane, and the fundamental polarised along the 2 axis, we have $\hat{e}_b = \hat{e}_c = (0,1,0)$ and $\hat{e}_a = (\cos(\theta), -\sin(\theta), 0)$. Therefore $d_{eff} = d_{24}(-\sin(\theta)) = -d_{32}\sin(\theta)$. In this manner a complete table of the effective nonlinear coefficients for tuning in each of the three planes can be found for both ooe and eoo transitions⁷.

Tuning Plane \ Transition	ooe	eoo
1,2	0	$d_{32}\cos^2(\phi) + d_{31}\sin^2(\phi)$
2,3	$d_{31}\sin(\theta)$	0
3,1	$-d_{32}\sin(\theta)$	0

Table 2.2- Effective Nonlinear Coefficients for mm2 Crystals

Table 2.2 shows the values of the effective nonlinear coefficients for tuning in the principal planes of a mm2 crystal. In each of these planes there are two possible phase-match options, but in each plane there is one option which is ruled out as it has $d_{eff} = 0$. It is important that the value of d_{eff} be known for the particular configuration being used as although the nonlinear coefficients may look good in the data sheets the effective coefficient may be quite a lot lower in value. A good rule of thumb in looking for a non-zero d_{eff} is to make sure that the three waves have components along the axes specified by at least one of the nonlinear coefficients. For example, if the only non-zero coefficient is d_{12} then two of the waves must have components along the 2 axis and the third along the 1 axis. Similarly, if one looks at table 2.2 and fig 2.13 then it can be seen that when the wave is propagating along the 3 axis ($\theta=0$), the effective coefficient is zero, as none of the polarisation components can be along the 3 axis and the only nonlinear coefficients are d_{31} and d_{32} .

Like the linear susceptibility, from which one gets dispersion and absorption, the nonlinear susceptibility varies with frequency. The two are related by the driving force of the fundamental field, and provided the frequency is well away from any resonances the susceptibilities can be related by Millers Rule. This is given in Eqn. 2.15.

$$\chi_{ijk}^{(2)}(-\omega_{sh}; \omega_f \omega_f) = \chi_i(\omega_{sh}) \chi_j(\omega_f) \chi_k(\omega_f) \Delta_{ijk} \quad \text{Eqn. (2.15)}$$

where Δ_{ijk} is Millers coefficient and is constant for a given material. As the frequencies concerned are well away from resonance the absorption is low and the linear susceptibility can be directly related to the dispersion to give the relation $\chi_i(\omega_{sh}) \propto n_i^2(2\omega) - 1$. Provided the nonlinear coefficient is known at some given frequency the susceptibilities at any other frequency can then be calculated using the following expression:

$$d_{ijk}(\omega) = d_{ijk}(\omega_{known}) \left(\frac{(n_i^2(2\omega) - 1)(n_j^2(\omega) - 1)(n_k^2(\omega) - 1)}{(n_i^2(2\omega_{known}) - 1)(n_j^2(\omega_{known}) - 1)(n_k^2(\omega_{known}) - 1)} \right) \quad \text{Eqn. (2.16)}$$

Conclusions

All of the factors mentioned above must be taken into account when choosing the best crystal for second harmonic generation of a particular laser source, irrespective of the type of doubling scheme used. The simplest case of doubling is to pass the fundamental beam once through the crystal outside of the cavity. In this case the fundamental power is not affected by the frequency conversion and calculation of the expected power is straightforward. If either intracavity or external resonant doubling is used then the conversion itself depletes the fundamental power and for high conversion efficiencies there is an optimum crystal length at which the second harmonic power equals the power originally extracted at the fundamental^{4,5}. For the work done here the depletion of the fundamental is not significant and the crystal length was dictated by the more mundane factors of availability and cost. The practical aspects of SHG in a Ti:sapphire laser are described in Chapter 4.

Frequency Stabilisation

Lasers are increasingly being used both as absolute frequency standards and as spectroscopic sources. For both these applications the reduction of the laser linewidth to sub-MHz or Hz levels substantially increases their usefulness. In the former application the laser is usually locked onto an atomic transition and by a chain of frequency synthesis can be used as a reference for other frequencies. In spectroscopy both fixed frequency and tuneable lasers are used to look at atomic transitions not just in basic physics but also in commercial applications such as pollution monitoring. There is also a growing interest in the use of optical parametric oscillators for frequency conversion, in which the stability of the output is critically dependent on that of the input. For such reasons there has been a lot of research over the years to try to keep the output frequency of lasers as stable as possible.

Although the Ti:sapphire laser has a gain bandwidth of several hundred nanometers, the use of intracavity selection elements can narrow the output to a single cavity mode. In a free running Ti:sapphire laser such as the one used here the frequency of this mode is not fixed but varies by up to 40MHz over a period of a few minutes, due to changes in the optical length of the laser cavity. From an atomic viewpoint this frequency jitter is far above that caused by inalterable factors. There are three such fundamental noise sources⁹, the most pre-eminent of which is caused by the amplification of spontaneous emission. This creates phase fluctuations in the output which are random, unlike those of the amplified stimulated emission, and hence leaves a residual laser linewidth which is neither predictable nor correctable. The magnitude of this linewidth($\Delta\nu_{\text{osc}}$) is given by the Schawlow-Townes equation¹⁰:

$$\Delta\nu_{\text{osc}} = \frac{4\pi h\nu(\Delta\nu)^2}{P} \quad \text{Eqn. (2.16)}$$

where $\Delta\nu$ = half-width at half-maximum of cavity resonance,

ν = laser frequency, P = laser power

In general this limit is well below the milli-Hz level and although it is the theoretical limit of stability, it is well below that of most practical sources. Indeed the most important cause of frequency instability is fluctuations in the laser cavity length. The cavity mode spacing of the laser output for a ring laser is c/ℓ , where ℓ is the length of the laser. If the cavity length changes then the change in this mode spacing is such that $\frac{\Delta\nu}{\nu} = -\frac{\Delta\ell}{\ell}$. For a laser 1.2m long lasing at 800nm (such as the one considered here), a change of one wavelength in the cavity length causes the output to vary by a cavity mode (250MHz). To stabilise the output to less than 1 MHz therefore requires the cavity length to vary by less than 3.2nm.

The stability of lasers is generally improved through passive and active stabilisation techniques. These two methods are described in the rest of this chapter and are equally important in reducing the jitter. Firstly the passive stability is increased as much as possible using mechanical means. Secondly the length is actively stabilised using a servo loop. The two are related to each other such that ¹¹:

$$\text{overall stability} = \frac{\text{passive stability}}{1 + \text{servo gain}} \quad \text{Eqn. (2.17)}$$

Passive stabilisation

Among the factors which affect the laser cavity length are temperature changes of the air and laser components, vibrations of the mounts transmitted through the table, and pressure changes of the air. These can be roughly divided into low and high frequency components. Frequency fluctuations caused by thermal changes usually occur at sub-Hz rates but can cause GHz changes in the output frequency. Table 2.3 shows the frequency drift caused by temperature for the Schwartz laser used here¹².

Component	MHz/°C
Ti:sapphire crystal	47
Birefringent filter	47
Faraday glass in optical diode	69
Stainless steel base	3600

Table 2.3 - Frequency Drift caused by Temperature Changes of Laser Components

Added to those listed above should be the change caused by temperature to the refractive index of the air in the laser cavity. At 800nm a change of 1°C causes a change in refractive index¹³ of 2.746×10^{-4} , which for a 1.1m length of air in the cavity corresponds to a frequency change of 94GHz. This is a low frequency pressure change but there are also higher frequency pressure changes caused by acoustical noise in the environment. The higher frequency components of laser noise are usually those due to vibrations of the various components in their mounts. These can be caused by practically anything - passing traffic outside, people walking in the lab or even a dropped Allen key.

There are various techniques to reduce both the low and high frequency components of the jitter before resorting to active stabilisation. One of the most effective passive stabilisation techniques relies on making the laser components as immovable as possible. In lasers such as the CO₂ laser the mirror mounts can be made of heavy blocks of metal with very rigid tuning controls so that the mirrors themselves wobble as little as

possible. For Ti:sapphire lasers this has limited practicability as the laser is usually (and is in this case) a tabletop system which needs fine tuning to peak the power. Another alternative, although an expensive one, is to build mirror spacers made of a material with a very low thermal expansion coefficient, such as Invar. For the basic SEO Ti:sapphire laser the frequency drift due to expansion of the base can be reduced to -58MHz/C by changing from stainless steel to Invar.

In order to isolate the laser from vibrations transmitted through the table it is usual to either float the table on air supports or ensure that the table is heavy enough to be relatively unaffected by all but the most severe vibrations. To further decouple the laser from any high frequency vibrations of the table, the base board can be placed in a tray of sand or on a solid foam cushion.

After mechanical vibrations one of the greatest sources of instability is acoustical vibrations of the air. In the Ti:sapphire laser about 99% of the path length is air, making it particularly prone to this type of instability. This can be muted by covering the inside of the laser box with acoustical foam and by making the box itself of some solid and porous material such as wood to stop it from acting as a drum. A further option is to isolate the interior of the box from outside pressure changes by sealing all input and output windows and to regulate the internal air pressure.

Despite all such precautions there will always be some residual noise at both low and high frequencies. For example a change in temperature of 0.1°C alters the SEO laser output by 16MHz just through the expansion of the Ti:sapphire crystal, birefringent filter (BRF) and optical diode, all of which are indispensable. In order to stabilise sub MHz active stabilisation techniques must be used.

Active Stabilisation

Any system of active stabilisation has three main parts; a discriminator to detect the frequency deviations, electronics to determine the type of feedback, and the length control element(s) within the cavity.

Discriminators

In general there are two types of discriminator- those which detect changes from a fixed frequency which cannot be altered and those which detect changes from a frequency which can be changed to suit the user. In the former case the discriminator is usually an atomic absorption line. For example, it is now common practice to lock He-Ne lasers to one of the iodine absorption lines¹⁴ and visible wavelength dye lasers can also be locked to iodine lines, which cover the region from 500nm to 675nm ¹⁵. In these cases the laser light is passed through an iodine absorption cell placed either intra or extra cavity and the derivative of the absorption is used as the error signal. An alternative method, which can be used with discharge lasers, is to use the opto-galvanic effect¹⁶, in which the electrical

conductivity of the discharge varies when light of a frequency corresponding to one of its transitions is shone into the discharge. Unfortunately there are no readily accessible atomic resonances in the near infrared and although absolute frequency locking can be accomplished by means of frequency conversion of the output¹⁷, this is cumbersome and usually expensive.

The most commonly used type of discriminator is a confocal Fabry-Perot resonator. This can measure relative frequency changes in three ways, two of which monitor the transmission of the interferometer and the third of which monitors reflections from the interferometer. In the first scheme the laser frequency is tuned half way up a transmission fringe of the etalon, as shown in figure 2.14, and this is used as the 'lock point' of the discriminator. Any deviations from the lock point are measured as a positive or negative voltage change¹⁸, depending on whether the frequency change is up or down the transmission fringe. Alternatively, the lock point can be at the peak of the transmission fringe. In this case the laser frequency is dithered and the first derivative of the discriminator signal is used as the error signal. Although side of fringe locking has the greater Voltage per Hz change, it imposes a limitation on the feedback electronics, as the response time of the reference cavity causes an overshoot of the compensating signal which for large servo bandwidths could move the laser frequency away from the capture area. Despite this it is still one of the most widely used types of discriminator, as it allows laser sources to be stabilised well below the MHz level. Figure 2.14 shows the discriminator and error signals of a typical side of fringe experiment.

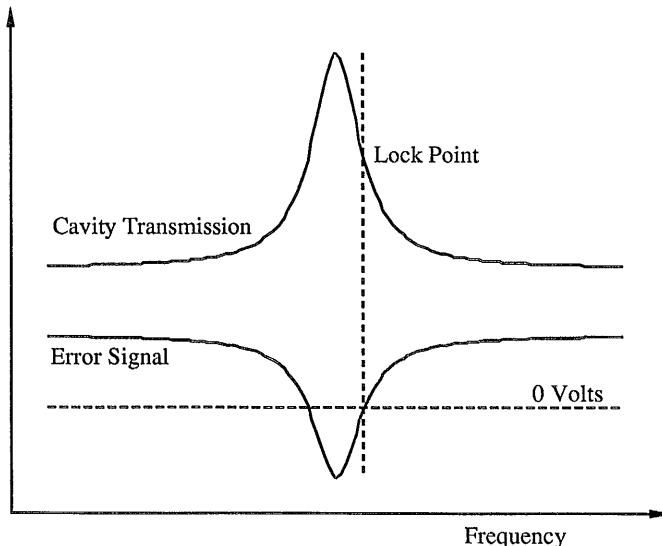


Figure 2.14 - Side of Fringe Discriminator and Error Signals

The upper curve is the transmission of the confocal Fabry-Perot resonator. The finesse(F) of the transmission is dependent on the reflectivity of the confocal mirrors (in this curve they are 90% reflective) and is given by the expression:

$$F = \frac{\pi\sqrt{R}}{1-R}$$

From this the width of the peak($\Delta\nu$) can be found, as it is related to the free spectral range of the resonator(FSR) by the relation $\Delta\nu = \text{FSR}/F$. The greater the reflectivity the larger is the error signal slope and so the better is the signal to noise ratio of the system. Unfortunately using high reflectivities has two major drawbacks. Firstly, the range over which the discriminator correctly interprets frequency changes is not symmetrically placed around the lock point. In figure 2.14 voltages above zero are seen as increases in frequency and those below as decreases. However if the frequency decreases by more than $\Delta\nu$ then the error signal incorrectly interprets this as an increase and the laser will be pushed to the next transmission fringe down. Secondly, the higher the finesse the smaller is the range over which the signal varies as the frequency changes. At a distance of about $2\Delta\nu$ from the peak the error signal is always the same and there is a far greater chance that the laser will overshoot the peak when correcting for frequency changes. Despite this, the technique allows stabilisation down to the kHz region^{19,20}.

The third scheme using F-P resonators was developed by R W Drever et al.²¹, based upon a scheme first suggested by R V Pound²². Unlike the previous scheme this one can respond to phase changes of the laser rather than frequency changes and is not limited by the reference cavity response time. The reference cavity effectively acts as an average phase storage unit. A small amount of the signal is reflected off the input mirror of this cavity and combines with leakage from the cavity to give a signal whose phase is proportional to the difference between that of the reflected signal and the "average" stored within the reference. This phase difference varies most as the laser is tuned over the resonance of the reference cavity. As part of this technique the laser output passes through a phase modulator which imposes sidebands at frequencies separated from the laser by the modulator frequency(ω_m). These sidebands are outside the resonator frequency passband and are totally reflected by the reference cavity when it is near the laser frequency. They are then heterodyned with the frequency dependent phase signal to produce a frequency dependent error signal. The sidebands act as a phase reference in much the same way as fringe locking techniques have an intensity reference. In other words, it is not so much the absolute phase (ϕ /transmitted intensity) that is important as the difference from that on resonance (ϕ /locking point).

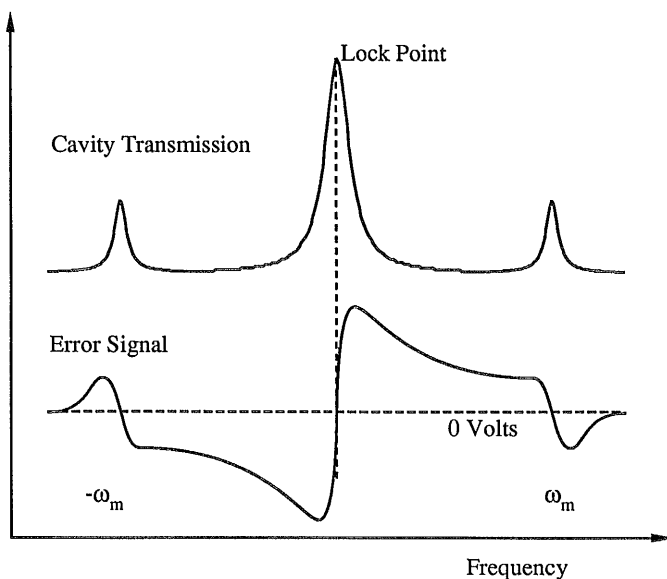


Figure 2.15 - Pound-Drever Discriminator and Error Signals

Figure 2.15 shows typical discriminator and error signals for a Pound-Drever locking scheme. As in figure 2.14 the upper curve is of the transmission signal as the reference cavity is tuned, and the mirrors have 90% reflectivity. The lower curve is the error signal which is now based on phase rather than intensity changes. At resonance of the three frequencies the signal passes from positive to negative or vice versa. Unlike side of fringe locking the 'correct error' range is symmetrical around the lock point, and extends to $\pm\omega_m$. The scheme therefore allows high finesse etalons to be used without the drawbacks mentioned for the side of fringe locking. This allows very high stabilisation levels to be reached. For low frequency changes the system behaves like that of fringe transmission. This stability obtainable with such a technique is potentially only limited by shot noise in the electronics²³.

In any scheme using a reference cavity the frequency stability of the laser is only as good as the reference cavity stability. Precautions can be taken to make the cavity as rugged as possible, with a high thermal capacity to reduce temperature drift and some form of temperature stabilisation, but the only absolute stabilisation techniques are those which lock to an atomic transition.

Cavity length control elements

There are three commonly used types of element to control the cavity length. In general the larger the deviation the element can compensate for, the lower is the

frequencies at which it can do so. The lowest frequency perturbations, such as those caused by thermal drift which occurs at sub-Hz levels, up to frequencies of a few hundred Hz, are usually compensated for by the use of either one or two tilting plates inside the cavity. The two arrangements which can be used for changing cavity length with tilting plates are shown in figure 2.16.

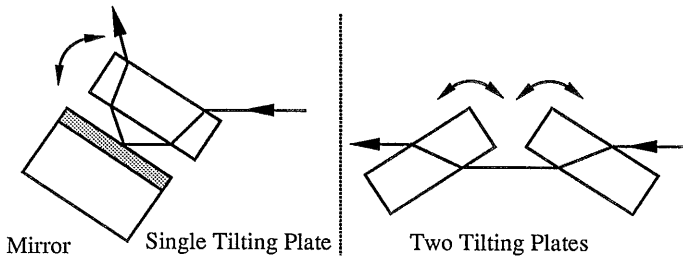


Figure 2.16 - Tilting Plate Arrangements for Cavity Length Tuning

One plate can be used if it is placed close to a mirror so that the intracavity beam passes through it twice causing no misalignment of the cavity as the plate tilts. Otherwise two counter-rotating plates are employed. The plates are usually placed at Brewster's angle within the cavity to cut down on insertion loss. The change of frequency is directly proportional to the angle through which the plates tilt and can cover tens of GHz for a 1 m ring cavity. Tilting plates are only necessary in longer cavities. In short cavities, such as in diode pumped Nd:YAG systems²⁴, the distance which needs to be moved to compensate for frequency shifts is proportionately shorter (n.b. $\frac{\Delta\nu}{\nu} = -\frac{\Delta l}{l}$) and so only the other two methods are used.

The second method is to mount a mirror on a piezo-ceramic controller.

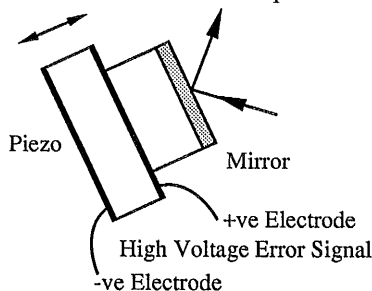


Figure 2.17 - Piezo Mounted Mirror

For a disc piezo the displacement is proportional to the applied voltage. A typical value is 0.4nm/V²⁵, so that a voltage swing of $\pm 20V$ will cover $\pm 2.5MHz$ in a 1.2m

long cavity and 22.5MHz in a 10cm long cavity. Piezos can respond at rates of tens of kHz depending on the type used and the limit imposed by resonance. The final control element is to use an electro-optic crystal, such as LiNbO_3 or KDP, within the cavity. When the error signal is applied to the crystal electrodes the refractive index of the crystal is changed, changing the optical length of the cavity. This length change is not large but the crystal can respond at frequencies up to the MHz level and so is used when stability down to Hz levels is required.

Control Electronics

The third component of any servo loop is the control electronics. These turn the error signals into the voltage signals which move the length control elements. In the experiment reported in Chapter 5 a side of fringe locking scheme is used and the control electronics for that are detailed then. Obviously the electronics for a Pound-Drever scheme are somewhat different to those for locking onto the side of a fringe, but all the methods have a few techniques in common. The error signal is first balanced to eliminate any intensity changes which might appear to be frequency changes. The resultant is then amplified and split into several parts for each of the length components. Each length component has a characteristic resonant frequency. For the tilt plates this is in the 100's of Hz region, for the piezo it is in the 10's of kHz region. The error signal must be rolled off well below these resonant frequencies or the component will begin to oscillate and will add noise to the system (a standard rule of thumb is to make the unity gain point a third of the resonance frequency). The tilt plates usually are controlled by the output of an integrator and the piezo signal rolled off using a low pass filter (or several). It is also important that the phase delay of the system be kept as low as possible so that the length is not being corrected in anti-phase to that needed. It is in making the signal to noise ratio as good as possible and in keeping the servo gain high while avoiding resonance that the electronics become critical.

The outline of stabilisation techniques given above is by no means complete but is meant more as a rough guide to the more common methods used. The exact scheme used is very dependent on the laser system and the application for which it is required. Some systems are naturally more stable than others and if the demands on them are not stringent they can be used with little modification. Other systems, such as those needed for gravity wave detectors, have far higher demands and it is worth spending a lot of effort and money in making them stable. For the Ti:sapphire laser the demands fall somewhere in-between and the experiment in Chapter 5 is aimed at making the laser a useful spectroscopic tool with sub-MHz resolution.

References

- 1 D A Kleinman, A Ashkin and G D Boyd - Second Harmonic Generation of Light by Focused Laser Beams - Phys Rev 145, 338, 1966
- 2 G D Boyd and D A Kleinman- Parametric Interaction of Focused Gaussian Light Beams- J.App.Phys, 39, 1968, p3597-3639
- 3 G A Boyd, A Ashkin, J M Dziedzic and D A Kleinman- Second Harmonic Generation of light with Double Refraction- Phys Rev, 137, 1965, p1305-1320
- 4 A Ashkin et al. - Resonant Optical Second Harmonic Generation - IEEE J-QE, vol. QE-2, No.6, pgs 109-124, 1966
- 5 R G Smith - Theory of Intracavity Optical Second-Harmonic Generation - IEEE J-QE, vol. QE-6, No.4, 1970
- 6 A Yariv - Optical Electronics - 3rd Ed., CBS College Publishing, 1985
- 7 FA Hopf and G I Stegeman -Applied Classical Electrodynamics- Vol.II:Nonlinear Optics- John Wiley and Sons- 1988
- 8 Jianquan Yao and Weidong Sheng- Accurate Calculation of the Optimum Phase Matching Parameters in Three Wave Interactions with Biaxial Non-linear optical Crystals- J. Opt. Soc. Am. B, vol.19, no.6, pgs 891-902, 1992
- 9 W Demtroder -Laser Spectroscopy - Springer Series in Chemical Physics, Springer-Verlag, Berlin, 1981
- 10 A L Schawlow and C H Townes - Infrared and Optical Masers - Phys. Rev., Vol. 112, No. 6, pgs 1940-1949, Dec 1958
- 11 A B Marchant - Optical Recording, A Technical Overview - Addison-Wesley Publishing Corp. Inc., 1990
- 12 P F Moulton - Tuning the CW Ti:Sapphire Laser - P F Moulton - Schwartz Electro-Optics, Inc., Research Div., 45 Winthrop St., Concord, MA 01742
- 13 Handbook of Chemistry and Physics - CRC Press - 53rd Edition, Chemical Rubber Publishing Company, USA, 1973
- 14 D A Jennings, J L Hall and H P Layer - Direct Frequency Measurement of the I₂ stabilised He-Ne 473-THz (633nm) Laser - Opt. Lett, vol. 8, no. 3, 136-138, Mar 1983
- 15 S Gerstenkorn and P Luc - Atlas du spectre d'absorption de la molécule d'iode - Centre National de la Recherche Scientifique, Paris, 1978
- 16 J-T Shy and T-C Yen - Optogalvanic Lamb-Dip Frequency stabilisation of a CO₂ Laser - Opt Comm, Vol. 60, no. 5, pgs 306-308, 1986
- 17 S V Kruzhlov, V A Pakhomov, et al. - Frequency Stabilisation of a Nd:YAG laser by means of ¹²⁷I₂ absorption lines - Sov. Tech Phys Lett 11(3), Mar 85 pgs 111-112

- 18 R L Barger, M S Sorem and J L Hall - Frequency Stabilisation of a cw dye laser -
App/ Phys Lett., Vol 22, no. 11, 1 June 73, pgs 573-575
- 19 J Helmcke, SA Lee -Dye Laser spectrometer for ultrahigh spectral resolution:
design and performance - Apl. Opt., vol 21, no. 9, 1 May 82, pgs 1686-1694
- 20 W Vassen, C Zimmermann et al. - A Frequency-Stabilized Titanium Sapphire Laser
For High-Resolution Spectroscopy - Opt. Comm., vol. 75, no. 5, 6, 15 Mar 90,
435-440
- 21 R W P Drever, J L Hall et al. -Laser Phase and Frequency Stabilisation using an
Optical Resonator - Appl. Phys. B., Vol 31, pgs 97-105, 1983
- 22 R V Pound - Electronic Frequency Stabilisation of Microwave Oscillators - Rev Sci
Instrum, 17, no. 11, pgs 490-505, Nov 1946
- 23 C Saloman, D Hils and J L Hall -Laser Stabilisation at the millihertz level - J. Opt
Soc Am. B, Vol. 5, No. 8, Aug 1988 pgs 1576-1587
- 24 Y L Sun and R L Byer -Submegahertz frequency-stabilised Nd:YAG oscillator -
Opt Lett, Vol. 7, No. 9, Sept 82, 408-410
- 25 Piezoelectric Ceramics -Morgan Matroc Ltd., Vemitron Division, Southampton,
Britain

Chapter 3

Equipment and Laser Development

In this chapter there is a description of the equipment used in the work on scanning, stabilisation and second harmonic generation with the Ti:sapphire laser. The system started as a basic unstabilised ring laser and was developed to adapt it for use in both intracavity frequency doubling and spectroscopy. The latter in particular requires a source tuneable over a few tens of GHz and stabilised to sub MHz levels.

Titanium Sapphire Laser

The titanium sapphire laser used in this development work was built around a Titan-CW model bought from Schwartz Electro Optics. This is a modular laser which is supplied mounted on its own breadboard base. A great advantage of this laser is that each component can be easily readjusted, and the whole laser can be removed and remounted on a standard optical table. This allows much freedom in the reconfiguration of the laser. A schematic diagram of the modified Ti :sapphire laser is given below.

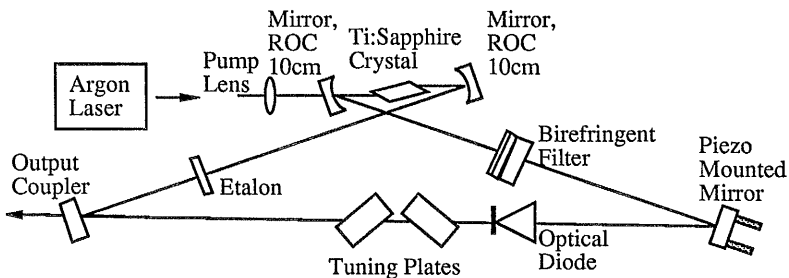


Figure 3.1 - Modified Ti:Sapphire Cavity

The pump laser used in these experiments was a commercial (model 2030-20) argon ion laser produced by Spectra-Physics. This laser can produce up to 20W of power when operating on all lines or 8.5W on single line operation at 514.5 nm¹. The laser was usually run on all lines, with up to 10W of TEM₀₀ light pumping the Ti:sapphire laser. It was found to be very important to ensure that the mode of the pump laser was as close to TEM₀₀ as possible, to allow optimum mode matching between the pump beam and the circulating infrared beam. (On one occasion when the argon ion plasma tube had degraded and the output was in the form of a doughnut shaped TEM₀₁* mode, the

replacement of the tube by one which allowed true TEM₀₀ operation was enough to cause a 50% increase in output power of the Ti:sapphire laser for the same input power.)

The argon ion laser produces vertically polarised light which is then rotated by a half wave plate to give the optimum horizontal polarisation required to pump the Ti:sapphire laser. The pump beam is focused to a spot of waist size 13μm within the crystal by a lens of focal length 8cm. The Ti:sapphire crystal absorbs 79% of the multiline power from the argon laser. The laser crystal itself is 7.45mm in length and is cut in the horizontal plane at Brewster's angle as shown in figure 3.2.

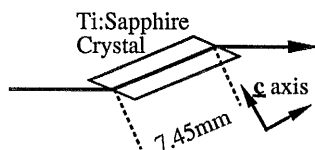


Figure 3.2 - Titanium Sapphire Crystal

As titanium doped sapphire is a birefringent material, the crystal is cut such that the polarisation of the light on passing through the crystal is parallel to the optic axis of the crystal². This stops the crystal from acting as a waveplate, which can cause oscillations in the output power as the wavelength is varied by the birefringent filter. The laser was operated in its ring configuration to eliminate spatial hole burning in the gain medium.

The full wavelength range of the laser is covered by three sets of mirrors, each individually covering the ranges 700nm-800nm, 800nm-900nm and 900nm-1000nm. Figure 3.3 shows the output power of the laser over the three mirror sets taken on one day with a pump power of 10W all lines. The peak of the output is at 810nm where there is approximately 12% conversion of power from the blue green to the infrared.

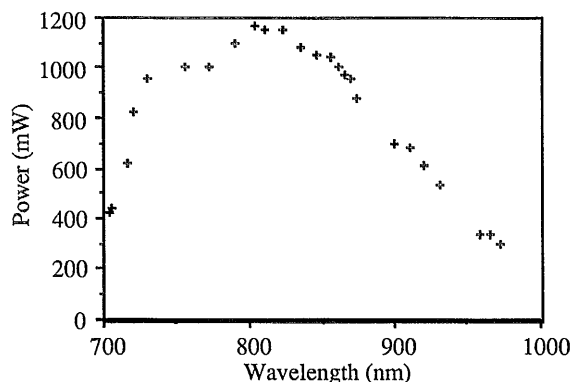


Figure 3.3 - Power vs. Wavelength

The mirrors work as the most coarse of the frequency selection elements in the laser by reducing the possible lasing bandwidth to 100nm. The two small curved mirrors around the laser crystal have radii of curvature of 10cm. They are separated by a distance of 10.76 cm and are tilted such that the radiation is incident at 9.75° . This arrangement results in an output beam whose diameter is roughly $470\mu\text{m}$ with an astigmatism of less than 3% between the horizontal and vertical waists. The mirror through which the pump beam travels is anti-reflection coated on the reverse side for the blue/green pump light. The two other mirrors are both flat - one is coated as a high reflector and the other is the output coupler, which has a transmission of 4% to 6% over its intended wavelength range and is anti-reflection coated on the reverse side to minimise loss of the transmitted light.

The main tuning element in the cavity is the birefringent filter. This narrows the spectral output of the laser to just a few cavity modes, with the selected frequencies dependent on the angle between the polarisation of the radiation and the crystal axes of the filter. As is usual, several plates are used in the filter (in this case three) to ensure both a large spacing of transmission frequency, and to ensure reasonable sharpness in the transmission peaks. In this case the lasing modes are limited to a region of less than 1GHz in which there are no more than three cavity modes going at any one time. Limiting the tuning range to 100nm by the mirror reflectivity assures that modes away from the main ones, which also have close to zero rotation introduced by the birefringent filter, are below oscillation threshold. In theory it is possible to have just one mirror set covering the whole range of the laser and tune to a few cavity modes solely by means of the birefringent filter. In practise this would mean that the thinnest plate of the filter would need to be microns thick. Plates that thin are difficult to manufacture and very delicate.

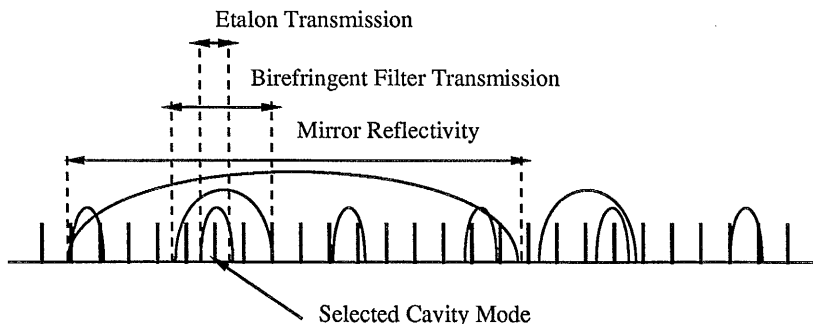


Figure 3.4 - Mode Selection by Elements within Laser Cavity

The linewidth is then further reduced by the insertion of a thin (1mm thick) etalon which has a finesse of 0.6 and a free spectral range of 100GHz. As the laser cavity modes are spaced by $\sim 250\text{MHz}$ and there are at most three modes oscillating, only one

etalon transmission peak coincides with the oscillating modes. Within this peak one of the modes is usually nearer the maximum than the others and hence has a larger gain/loss ratio, which is sufficient to reduce the output to a single longitudinal mode.

The direction of lasing within the cavity is set by the optical diode. This contains a waveplate and a Faraday rotator. The waveplate rotates the polarisation of the radiation by a small amount independent of its direction within the cavity. The Faraday rotator, however, is direction selective and rotates the polarisation either clockwise or anti-clockwise depending on the direction of lasing. For one direction of light travel the net polarisation rotation of the two components cancels and in the other they reinforce resulting in a much higher loss by Fresnel reflection as the radiation passes through the Brewster angled surfaces within the cavity, which are aligned to give minimum loss for horizontal polarisation of the radiation. As the two directions are in competition for the same population inversion, the decreased gain to loss ratio in one of the directions is enough to suppress lasing in that direction.

Tuning Equipment

In order to change the laser into a source suitable for spectroscopy it is necessary to be able to scan the laser frequency over a range of tens of GHz while still keeping the output as a single stabilised longitudinal mode. To do so the cavity length itself is continuously varied by rotating the two tuning plates within the cavity. These were 4mm thick and were constructed of BK7 glass, whose surfaces were parallel to 30 seconds of arc, and whose surface quality with regard to flatness was to better than $\lambda/10$. These were mounted on a pair of galvanometers (General Scanning G208) and were oriented at Brewster's angle (θ_B) to the cavity radiation and $180-2\theta_B$ to each other. The change of output frequency with cavity length (L), is given by the expression: $\Delta\nu = -v \frac{\Delta L}{L}$. As the two plates rotate within the cavity a portion of the cavity length has its refractive index changed from that of air to that of the BK7 glass ($n=1.51$), or vice versa and so effectively increases or decreases the optical path length of the cavity. Because there are two plates within the cavity which rotate in opposite directions, the overall position of the beam is not changed once the beam has passed through both plates. The change in refractive index of a small length of the cavity, (∂L), from 1 to n will result in a change of output frequency of $v(1-n)\partial L/L$. The rate at which the cavity length varies as the tuning plates are rotated through a small angle $d\theta$ away from the angle of incidence θ is given by the expression³:

$$\frac{\partial L}{\partial \theta} = \frac{n^2 d \sin(\theta) \cos(\theta)}{(n^2 - \sin^2(\theta))^{\frac{3}{2}}} + d \sin(\theta) - \frac{d \sin^3(\theta) \cos(\theta)}{(n^2 - \sin^2(\theta))^{\frac{3}{2}}} - \frac{2d \sin(\theta) \cos(\theta)}{(n^2 - \sin^2(\theta))^{\frac{1}{2}}}$$

Eqn. (3.1)

where θ is the angle of incidence and d is the plate thickness

This is a linear expression with regard to $d\theta$ and so a linear scan of frequency can be accomplished by applying a linearly varying voltage to the galvanometers. For the two 4mm thick tuning plates the overall change in frequency is 20.42 GHz per degree change from Brewster's angle (56.5°). The galvanometers can rotate over $\pm 4^\circ$ and so can scan over a maximum of ± 80 GHz. As the cavity modes are moving with the change in length, the etalon transmission must also move along with the mode it has selected or the laser will mode hop across the frequency scan as successive modes move under the etalon transmission peak. The condition for maximum transmission of a Fabry-Perot etalon is that $2nd \cos(\theta) = mL$, and from this the change in transmission of the etalon for small deviations (θ) from normal incidence can be found to be:

$$\Delta v = \frac{v\theta^2}{2n^2}$$

Eqn. (3.2)

The change in transmission frequency is therefore proportional to the square of the angle through which the etalon has rotated. If a linear ramp is applied to the tuning plates in order to scan the cavity, the ramp voltage must pass through a device which finds its square root before being applied to the galvanometer which drives the etalon so that the change in transmission frequency of the etalon also alters linearly in step with the tuning plates. Figure 3.5 shows the variation of frequency with angle for both the tuning plates and the etalon. For the etalon 0° is normal incidence, and for the scanning plates it corresponds to Brewster's angle.

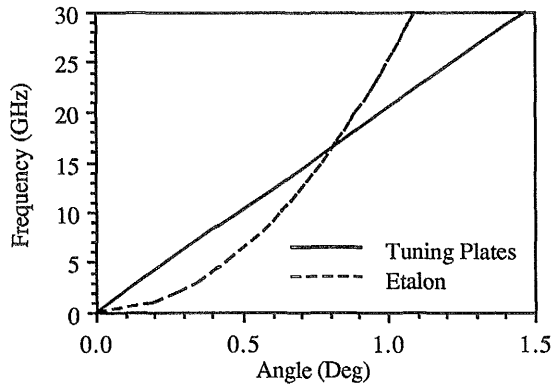


Figure 3.5 - Change in Frequency vs Angle

The galvanometers are driven by two units, one of which controls the two tuning plates and the other the etalon. Each driver has a maximum input of 10V. The inputs are from a triangular function generator (Feedback FG601) which gives scans of $\pm 5V$ over a frequency range from 0.001Hz - 1MHz. This is usually operated on the lower frequency settings to give scan lengths from sub-seconds to several minutes. The voltage scan is then passed through a unit which offsets the voltage by 5V and gives an output of 0-10V. For greater accuracy in the output frequency the laser is tuned while being actively stabilised.

Stabilisation Equipment

For the purposes of stabilisation a small portion of the output beam (about 4%) was split off to the monitoring equipment by an uncoated glass beamsplitter (Fig 3.6).

This beam was further split to both the scanning confocal interferometer and the stabilisation system. The scanning confocal interferometer was constructed with a finesse of 30 and a free spectral range of 1.5 GHz. This etalon both shows the longitudinal mode structure of the laser and provides a marker to show how far the laser had been scanned.

The remainder of the monitoring beam is used for the light balance circuit used in stabilising the laser. Before entering the static confocal interferometer, a portion of the remaining beam is split off onto a BPX65 photodiode. This beam monitors the intensity variations of the laser output. The magnitude of this beam can be altered using a neutral density wheel (Ealing Electro Optic).

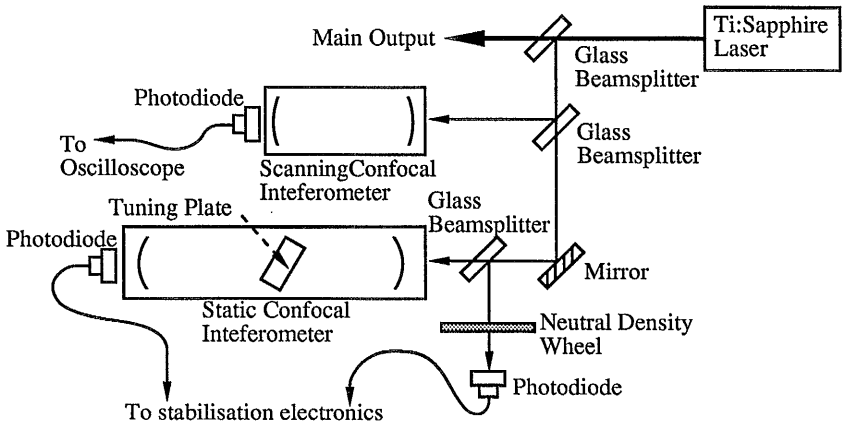
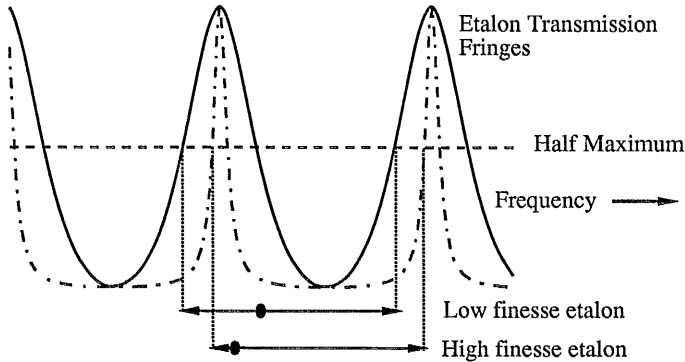


Figure 3.6 - Monitoring and Stabilisation equipment

By adjusting the average intensity incident on the photodiode to half that of the maximum transmission of the static confocal interferometer and subtracting it from the transmission of the etalon, one can ensure that intensity changes are not interpreted as frequency changes of the laser. The static confocal etalon itself was constructed with a low finesse of 2 and a free spectral range of 300MHz. The low finesse is necessary to ensure mode hop free scanning of the laser. This is illustrated in figure 3.7.



Frequency ranges over which stabilisation system will operate correctly. Lock point denoted by ●

Figure 3.7 - Lock Ranges of Low and High Finesse Etalons

The stabilisation system interprets any frequency change to a position above that of the lock point on the etalon transmission curve as a decrease in the laser frequency and corrects accordingly. Similarly a change to a position below that of the lock point is

interpreted as an increase in frequency. An etalon with a finesse of 10 and a free spectral range of 300MHz would have a full width half maximum (FWHM) value of 30MHz while that with a finesse of 3 has a FWHM value of 100 MHz. For the low finesse etalon the transmission changes are correctly interpreted over a range from -100MHz to +200MHz about the lock point, while the high finesse etalon interprets correctly from -30MHz to 270MHz. If the laser frequency hops down in value by more than 30MHz the high finesse etalon will incorrectly interpret this as an increase in frequency and will push the output frequency even further from the original lock point. The 'correction' will continue until the frequency is re-locked at a frequency 300MHz below that of the original.

Variations in the transmission of the static confocal etalon due to variations in the laser frequency are fed back via the light balance circuit to the laser cavity as changes in the cavity length. Slow fluctuations in the laser frequency are corrected by rotating the pair of glass plates within the laser cavity. Fast fluctuations in the laser frequency were corrected by applying a high voltage to the piezo ceramic on which the flat high reflector was mounted. The cavity length is 1.2m and so to achieve a stability of less than 100kHz it is necessary to control the cavity length to within 0.3nm.

The piezo ceramic on which the flat high reflector is mounted is a disc of thickness 2mm (thk), made of PZT5A material which has a d_{33} coefficient of $\sim -374 \times 10^{-12}$ m/V. The change in thickness for a voltage of V applied between the ends is given by $\Delta thk = d_{33} V$. The change of length per volt for this disc is therefore 0.37nm/V. The output of the stabilisation box varies by ± 75 V around a positive offset of 75 V for which the corresponding change in frequency is ± 8.25 MHz. The free running stability of the laser is less than 40MHz, which is outside the range covered by the piezo ceramic and so larger variations over longer periods are controlled by the Brewster plates. Fig 3.8 is a schematic of the operation of the stabilisation system. It illustrates how the light balance circuit works to eliminate changes in the laser intensity from the static confocal etalon signal, which is then split into high and low frequency components which are fed back to the piezo mounted mirror and the Brewster plates respectively.

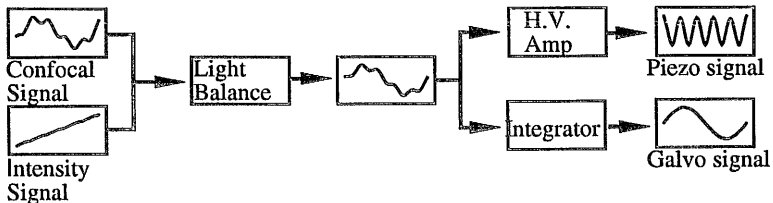


Figure 3.8 - Operation of Light Balance

When the laser is stabilised, the cavity cannot be scanned as simply as described previously, as the stabilisation system will act to compensate for the frequency changes with scanning and bring the output back to the lock point. It is therefore necessary to move the lock point along with the scan. The optical length of the reference etalon is controlled by a block of BK7 glass of length 4mm placed within the etalon cavity. The plate is mounted on a galvanometer, model no MG325D from General Scanning, which controls its angular position and is placed at roughly Brewster's angle to reduce unwanted etaloning effects, and to minimise reflectance losses. The input signal for the galvanometer comes from the Feedback FG601 Frequency Generator. The change in optical length of this etalon per degree of rotation of the internal plate can be calculated in the same way as for the tuning plates of the cavity (Eqn.3.1), and results in a change in output frequency of 24.5GHz per degree change from Brewster's angle. The frequency lock point of the laser is therefore also moved, and the tuning plates and the piezo mounted mirror act to keep the laser locked to the side of the etalon transmission. When scanning over a large frequency range, the error signal from the light balance circuit which is used to control the stabilisation elements is also large and the light balance has to be operated on a low gain setting to stop the output from saturation by the tuning signal. As better stabilisation is achieved with a higher gain setting, a voltage follow through from the frequency generator is added to the stabilisation signal before it is applied to the tuning plates. The laser is therefore coarsely tuned by the frequency generator while the stabilisation circuit compensates for any frequency deviations from the scan of the lock point. This arrangement is shown schematically in figure 3.9.

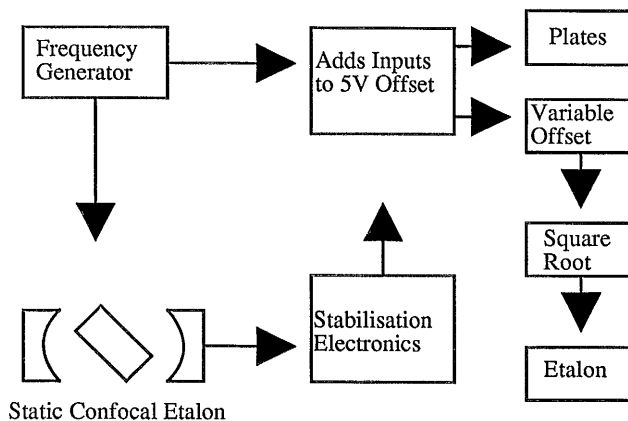


Figure 3.9 - Scanning Control

The experimental results of the stabilisation and scanning schemes are shown in Chapter 5.

Second Harmonic Equipment

To adapt the Ti:sapphire cavity for intracavity doubling, the circulating field has to be focused down into the doubling crystal, without significantly disturbing the waist within the Ti:sapphire crystal itself. Changing the waist size within the crystal would degrade the mode matching with the pump beam and result in lower output powers. In order to look at various schemes for intracavity doubling, the cavity was modelled on a computer to find the waist sizes in the vertical and horizontal planes inside both the Ti:sapphire and the doubling crystals. For the experiments in second harmonic generation it was necessary to produce a waist of no less than $250\mu\text{m}$. There were several ways in which this could be done, including the use of intracavity lenses or additional curved mirrors, but the least complicated method which involved no extra components in the cavity and so minimised the additional loss was found to be an alteration in the spacing of the two curved mirrors around the laser crystal. In the model of the laser cavity it is apparent that there is a secondary larger waist mid-way between the flat high reflector and the output coupler.

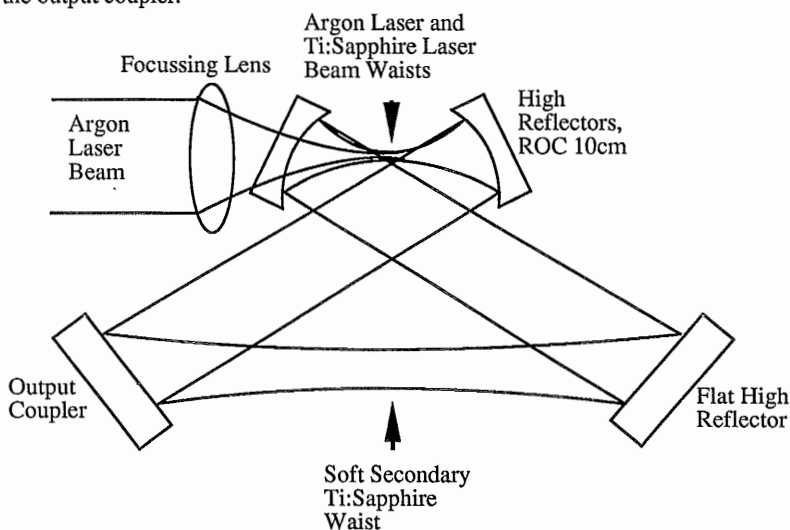


Figure 3.10 -Mode Sizes within Cavity

The waist sizes within the Ti:sapphire crystal as a function of mirror spacing are shown in figure 3.11. This stability curve shows the spacings for which the cavity can successively refocus itself to the same real waists as the radiation circulates within the cavity. For the best collimated output beam the laser operates on the edge of the stability curve which has the smaller mirror spacing, but by increasing the mirror spacing the

secondary waist is decreased, while the waist within the Ti:sapphire crystal goes through a maximum and then decreases again.

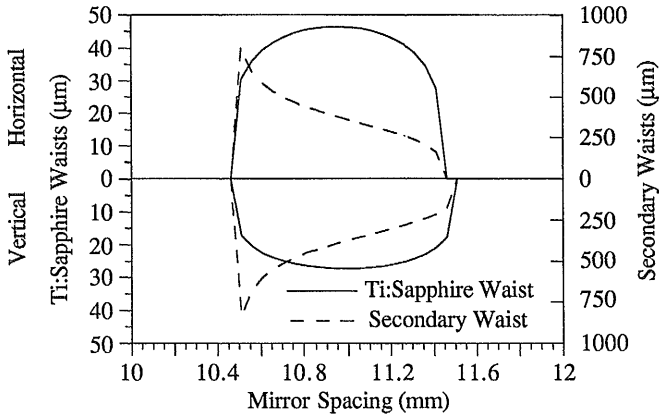


Figure 3.11 - Waist sizes in Horizontal and Vertical Planes

Initially the waists within the laser crystal were $44\mu\text{m}$ and $26\mu\text{m}$ in the horizontal and vertical planes respectively while the secondary waists were $464\mu\text{m}$ and $476\mu\text{m}$. This arrangement produces an output beam whose astigmatism is less than 3% with a beam radius of 493mm and a divergence of 1mrad in the far field. If the mirror spacing is increased by 4mm from 10.76cm to 11.16cm , the Ti:sapphire waists remain constant, while the secondary waists are reduced to 300mm and 316mm in the horizontal and vertical planes. The beam waists transmitted 23cm beyond the flat high reflector are necessarily the same as those at the secondary waist. They could therefore be measured using a scanning apertured photodiode mounted on two translation stages which moved the pinhole and photodiode in the horizontal and vertical planes.

The values given above are only valid if the angle between the incident and reflected beams on the small curved mirrors is 19.5° , which in the unaltered configuration produces a collimated beam in which the astigmatism generated by the rod is cancelled by reflection off the curved mirrors. However astigmatism in the secondary waists and output beam can be produced by variations in the position of the beam on the output coupler and flat reflector. These mirrors are 2.5cm in diameter and therefore variations in the beam position across the mirrors can cause a change of $\pm 2.3^\circ$ in the angle between the incident and reflected beams on the curved mirrors. Changes in this angle result in a divergence in the horizontal and vertical waist sizes about a central value, while the average of the two waists remains constant. This is shown in figure 3.12 as a function both of the spacing of the curved mirrors and of the angle between beams about the central value of 19.5° .

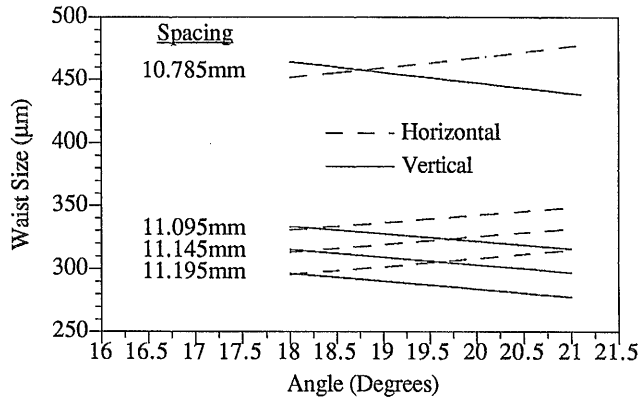


Figure 3.12 - Waist Size Variations

The doubling crystal was enclosed in a cylindrical copper oven of diameter 25mm with a circular aperture of 3mm. The crystal is pressure sensitive and was held in place by a lightly sprung plate, with both upper and lower contact areas highly polished to give good thermal contact between the crystal and the oven. The copper cylinder was placed in a second hollow cylinder constructed of aluminium on which were wound the coils of heating wire. This cylinder had two holes drilled in it - one for a thermistor and another for a thermocouple. Both temperature sensors were coated in a heat sink compound for good conduction between them and the oven.

The temperature controller used to heat the oven was a RFL model 7a controller supplied by Virgo Optics. This unit is capable of controlling temperature to an accuracy of $0.05^{\circ}\text{C}^{\circ}$. The heating wire used was from the London Electric Wire Company and was 0.193mm in diameter (36 SWG), silk coated, and wound to give an overall resistance of 300ohms. The thermistor was a glass bead type thermistor with a negative temperature coefficient, and a resistance value of 11 k Ω at 20 $^{\circ}\text{C}$. This was the feedback element to the temperature controller. The actual temperature was read directly from a Digitron type K Thermocouple. The oven was then enclosed in a block of Teflon to provide insulation against heat loss at high temperatures. The overall oven unit was mounted on a Micro Control prism table and placed in the cavity midway between the two flat reflectors, one of which replaces the output coupler in the doubling configuration. The prism table was capable of 2.5 $^{\circ}$ rotation about the x, y and z axes for optimisation of the phase matching angle.

Ancillary Equipment

Two different power meters were used in the experiments - a Coherent 210 for measuring powers of up to 10W with an accuracy of 10mW on the lowest scale, and a Newport 835 capable of measuring power levels from nano Watts up to 200mW. The blue generated as second harmonic radiation was separated from the residual infrared by a BG38 filter which passes less than 10^{-4} of infrared between 830nm and $1\mu\text{m}$ but 88% of power between 430nm and 450nm, taking into account both transmission and reflection losses. The high reflector of the cavity also has a transmittance of 91% over this wavelength range, so that the total power measured was 80% of that generated. In the experiments on stabilisation the noise levels of the laser were monitored using a Type 2033 Signal Analyser from Bruer and Kjaer capable of measuring frequencies from DC to 20kHz. The input for this was from the error signal of the stabilisation circuit. The wavelength was measured by a quarter metre focal length monochromator from Applied Photophysics Ltd., model no. F 3.4.

References

- 1 Spectra Model 2030 and 2035 High Power Ion Laser Instruction Manual - Laser Products Division, Spectra Physics Ltd.
- 2 P.F. Moulton - CW Ti:Sapphire Laser Tuning: A Straightforward Task - Photonics Spectra, pp 119- 122, March 91
- 3 C.E.Dunn - The Development of a Single Frequency, Frequency-Doubled, Ring Dye Laser and its Application to High Resolution Spectroscopy in the Ultraviolet - Ph.D Thesis, St. Andrews 1982
- 4 Piezoelectric Ceramics - Vernitron Division, Morgan Matroc Ltd.
- 5 Instruction data - RFL Industries

Chapter 4

Intracavity Second Harmonic Generation of a Ti:Sapphire Laser using Potassium Niobate

In the review of the theory of second harmonic generation given in chapter 2, the factors which affect the conversion efficiency from fundamental to second harmonic were discussed. In this chapter are presented results on the experimental intracavity doubling of the Ti:sapphire laser using a crystal of potassium niobate (KNbO_3). These experiments covered the wavelength range between 860nm to 905nm with the production of powers of up to 50mW in the doubled range from 430nm to 452nm. The characteristics of the system were examined and the practicability of this method of doubling the Ti:sapphire laser is discussed.

The two initial choices which have to be made in frequency doubling are the type of doubling scheme and the nonlinear medium. The three ways of doubling are single pass extra-cavity, intracavity, and external resonant doubling. In order to achieve the best harmonic power either intracavity or external resonant doubling are used to increase the available fundamental power. In these schemes it is theoretically possible to extract as much power in the second harmonic as the laser source usually provides at the fundamental¹. Intracavity doubling is always an attractive choice, as it involves no extra cavity and so is a compact source of doubled radiation. Alternatively, resonant doubling has the advantage that the SHG is decoupled from the laser and so any adverse effects such as thermal lensing do not disrupt the laser cavity. The disadvantage of this method is that the resonant cavity must be servo controlled to keep its length resonant with the fundamental wavelength. In the work described here we chose intracavity doubling for its relative simplicity and robustness. Experimental results of the alternative method of external resonant doubling, also using KNbO_3 , are found in a paper by Polzik and Kimble².

Frequency doubling is usually most efficiently achieved using a birefringent crystal, as described in chapter 2, and that was what was used in this work. Later in this thesis there is a description of work on sum frequency generation using an alternative medium, namely an atomic vapour. Although the discrete levels associated with vapours allow the basic physics of frequency conversion to be better understood, and vapours have the advantage that they are transparent deep into the ultraviolet, the conversion efficiencies of nonlinear crystals are usually several orders of magnitude higher than those of vapours. Crystals are also not restricted to the relatively narrow

frequency regions in which vapours are resonantly enhanced by their proximity to an atomic transition. The choice of crystal is largely governed by its phase matching range and nonlinear coefficients, although the obvious choice on these grounds is not always the best as a practical source. The optical damage limit of the crystal, its thermal properties, whether it is hygroscopic or soluble in cleansing solvents such as methanol, its physical hardness which might limit the working of the crystal and its ability to be anti-reflection coated all contribute to both the cost of the material and its long term reliability. The properties of some crystals which could be used in the doubling of the Ti:sapphire laser and comments on their overall suitability are presented in Table 4.1. The nonlinear coefficients and damage limits are for the Nd:YAG wavelength of 1064nm as this is the most widely used source and are slightly lower over the 700nm to 1000nm range.

Material	Nonlinear Coefficient, d_{eff} (pm/V)	Damage limit (W/cm ²)	Comments
BBO	$d_{22} = 1.7$ $d_{31} = 0.12$	23×10^9 ($\tau = 14\text{ns}$) 4×10^6 CW	High damage threshold, but angle tuned so efficiency low at 900nm
BANAN	$d_{31} = 13$	3×10^6 ($\tau = 10\text{ns}$)	very low damage threshold
LiIO ₃	$d_{31} = -7$	6×10^7 ($\tau = 20\text{ns}$)	good properties but angle tuned so low efficiency at 900nm
LiNbO ₃		6×10^7 ($\tau = 10\text{ns}$)	Good but has to be cooled well sub zero at 900nm
ADP	$d_{36} = 0.5$	6×10^9 ($t = 15\text{ns}$)	Low coefficient
KNbO ₃	$d_{31} = -15.8$ $d_{32} = -18.3$	12×10^6 ($t = 10\text{ns}$) 1×10^4 CW	Good coefficient, but low damage threshold. Temperature tunable

Table 4.1- Comparison of Different Nonlinear Materials
Suitable for Phase-Matched SHG at 900nm

Of the materials shown above the two most suitable for the Ti:sapphire laser are lithium iodate and potassium niobate. The tuning curves and nonlinear coefficients over the wavelengths for which the materials are phase-matched are shown in figures 4.1 to 4.4.

Lithium iodate is a negative uniaxial crystal and SHG is achieved via a Type I ooe interaction. However, although the tuning range covers all the Ti:sapphire laser wavelengths, the effective nonlinear coefficient drops off at the higher wavelengths to 4pm/V, almost half its original value. For the higher wavelengths, over 857nm, potassium niobate has higher effective nonlinear coefficients and so looks the better material .

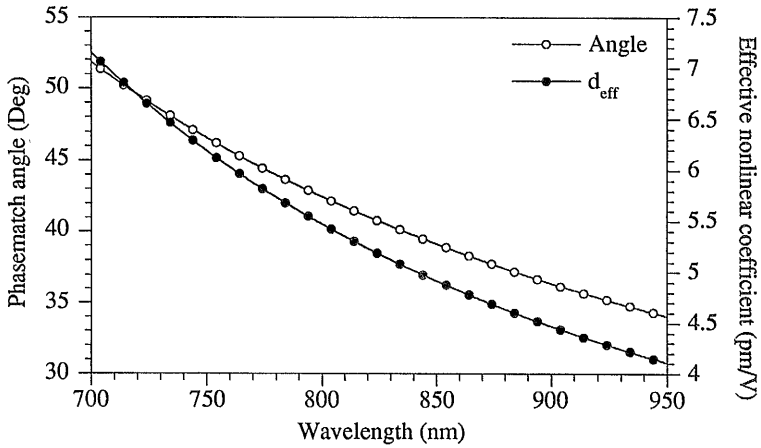


Figure 4.1 - Phase-match angle and effective nonlinear coefficient vs wavelength for lithium iodate

Phase-Matching in Potassium Niobate

Potassium niobate is a negative biaxial crystal, type mm2, with $n_x > n_y > n_z$ and the angle between the optic axes, ($2V_z$), is 65.40° . As potassium niobate is a biaxial crystal there is more than one phase-matching possibility. Figure 4.2 shows the range of wavelengths over which phase-matching is possible for tuning in the a-b plane.

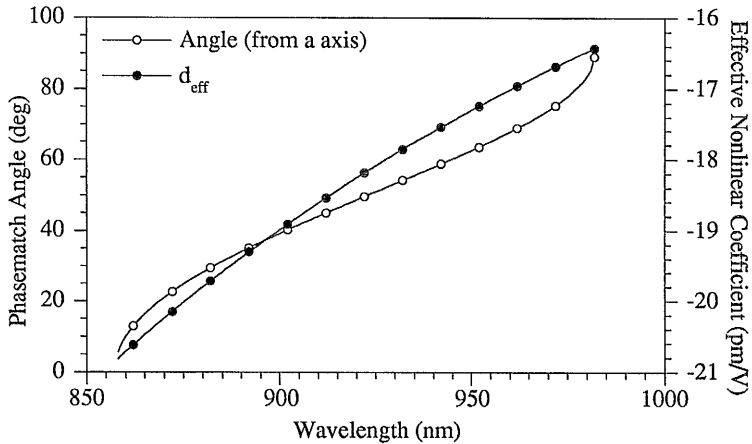


Figure 4.2- Phase match angles and effective nonlinear coefficients vs wavelength for tuning in the a-b plane of potassium niobate

This is a Type I *eeo* transition in which the second harmonic is polarised along the *c* axis. The minimum phase match wavelength is 857nm, which has an effective nonlinear coefficient of 20.8 pm/V. As in the case for lithium iodate, the effective nonlinear coefficient increases with wavelength.

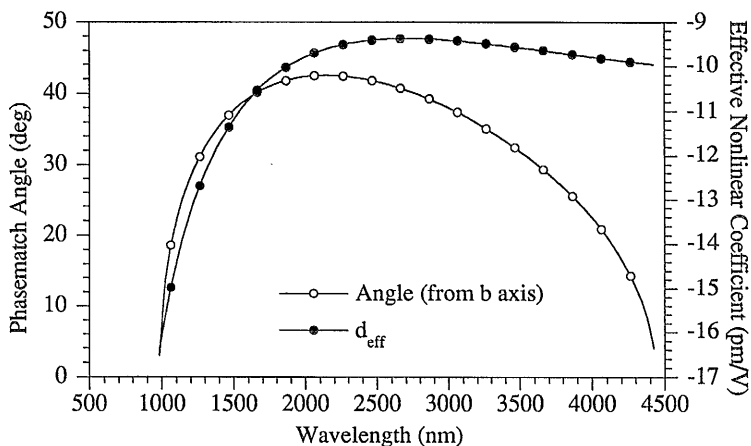


Figure 4.3 - Phase match angles and effective nonlinear coefficients vs wavelength for tuning in the b-c plane of potassium niobate

Figure 4.3 shows the phase matching range possible for tuning in the b-c plane. This takes over where the a-b plane stops, with the lowest phase matched wavelength in this plane being the highest in that plane (982nm). This is also for Type I phase matching, this time *ooo* with the fundamental being polarised along the *a* axis. However the best characteristics of all the tuning curves are for tuning in the a-c plane, a Type I *ooo* transition, with the fundamental polarised along the *b* axis.

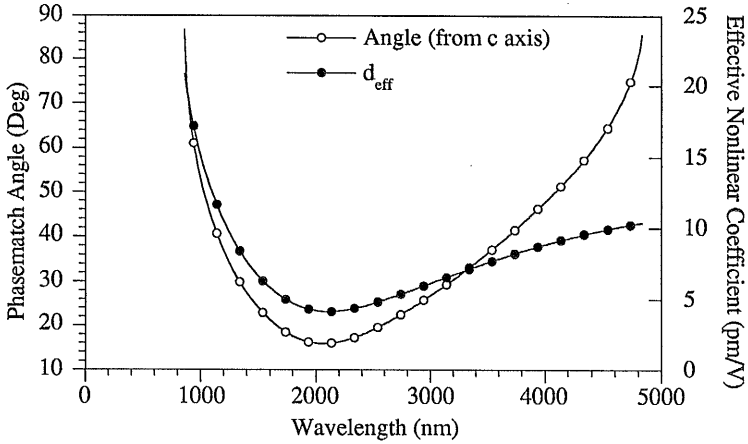


Figure 4.4- Phase match angles and effective nonlinear coefficients vs wavelength for tuning in the c-a plane of potassium niobate

Tuning in this plane allows the whole tuning range from 857nm to 4800nm to be covered. At the lowest phase-matched wavelength (857nm), the effective nonlinear coefficient is 20.8pm/V, considerably higher than that for lithium iodate. Added to this is the most attractive feature of potassium niobate, the fact that it can also be temperature tuned. If an angle tuning crystal is used for SHG, then to cover a range of wavelengths a range of crystals are needed, all cut at different angles for different wavelengths and if possible also cut at Brewster's angle for the laser polarisation. If the fundamental polarisation is in the tuning plane, then tuning away from the wavelength for which it is cut will cause an increase in cavity loss. If instead the crystal is temperature tuned then one crystal can cover a range of wavelengths and be either anti-reflection coated over the fundamental range or cut at Brewster's angle for the mid wavelength.

Refractive Indices and Temperature Tuning

For the following experiments a 4mm x 4mm x 1cm crystal of potassium niobate was used. It was cut for propagation along the a axis and was anti-reflection coated to give < 0.25% reflection from 860nm to 940nm. Figure 4.5 is a schematic of the crystal showing the polarisations of the fundamental and second harmonic with relation to the crystal axes.

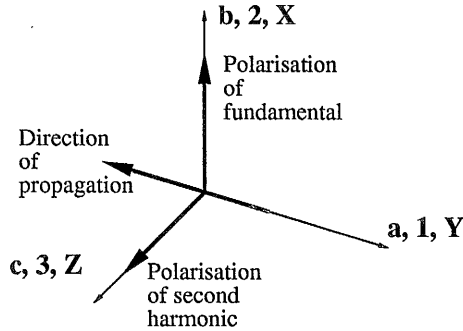


Figure 4.5 - Crystal axes in potassium niobate with polarisations of fundamental and second harmonic, for propagation along the a axis, temperature tuning up from 857nm.

The refractive indices for the three axes for a long time were thought to be well described by a Sellmeier equation with two oscillator terms, but more recent work by Zysset et al³ has added an additional infrared correction term to give a better fit to the available experimental data. At room temperature this Sellmeier equation is:

$$n^2 - 1 = S_1 \frac{\lambda^2 \lambda_1^2}{\lambda^2 - \lambda_1^2} + S_2 \frac{\lambda^2 \lambda_2^2}{\lambda^2 - \lambda_2^2} - D\lambda^2 \quad \text{Eqn. 4.1}$$

The coefficients for each of the three axes, n_a , n_b and n_c are given in table 4.2 for a temperature of 22 °C.

	S_1	S_2	λ_1	λ_2	D
n_a	2.005519×10^{13}	1.498408×10^{14}	2.581594×10^{-7}	1.290932×10^{-7}	2.517432×10^{10}
n_b	1.937347×10^{13}	1.354992×10^{14}	2.727478×10^{-7}	1.370050×10^{-7}	2.845017×10^{10}
n_c	1.60917×10^{13}	1.654431×10^{14}	2.552298×10^{-7}	1.197152×10^{-7}	1.943289×10^{10}

Table 4.2 - Sellmeier Coefficients at 22 deg C

This variation of refractive index with wavelength/frequency is shown in figure 4.6. For the configuration used in these experiments the refractive index for the fundamental, which is polarised along the b axis, must be made equal to that for the second harmonic, which is polarised along the c axis. This corresponds to a fundamental wavelength of 857nm at 22 °C, as marked in figure 4.6.

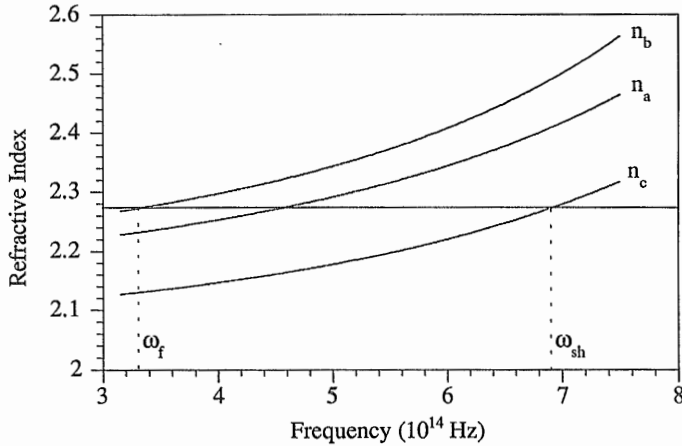


Figure 4.6 - Variation of Refractive index with Frequency at 22 degrees Celsius for polarisation along each of the crystal axes.

The two useful cases of propagation along the principal axes are a) propagation along the a axis with fundamental polarised along b axis as shown in fig 4.5, with the room temperature phase matched wavelength at 857nm and b) propagation along the b axis with fundamental polarised along the a axis, with the phase matched wavelength initially at 982nm. There is a zero effective nonlinear coefficient for propagation along the c axis so that even if phase matching were possible (which it is not) there would be no second harmonic generated.

The change of refractive index with temperature for each axis is also frequency dependent and cannot be given with just one equation. This is discussed in more detail later in the chapter when considering thermal effects. The more important variation is that of phase matching wavelength, which is dependent on the difference between the variation for the fundamental and the second harmonic. The change in refractive index for light polarised along the c axis is greater than that for the b axis by an order of magnitude, although the c axis variation is positive and the b axis variation is negative⁴. As the refractive index increases more quickly for the second harmonic the phase matching wavelength shifts upwards as the temperature increases. (For propagation along the b axis the temperature tuning is also positive as the a axis index variation is also less than that of the c axis. In this case the a axis variation is positive not negative and so the tuning is less.). Potassium niobate undergoes a phase- change at about 225°C from an orthorhombic to a tetragonal crystal structure⁵ so temperature tuned phase matching is only used at temperatures of up to 200° C. Additionally, at temperatures above about 190°C potassium niobate crystals tend to suffer from de-poling of the

ferroelectric domains⁶. This also occurs at lower temperatures if the crystals are heated or cooled too quickly, but can be avoided if a voltage of (typically) 100V is applied along the c axis.

Although the phase matching calculations are difficult to predict for temperature tuning, the change in phase matched wavelength has been found to be about 0.4nm per °C for the configuration studied here⁷. During the course of the experiment the wavelength and phase matching temperature were measured on a number of different occasions and the accumulated results are plotted in figure 4.7.

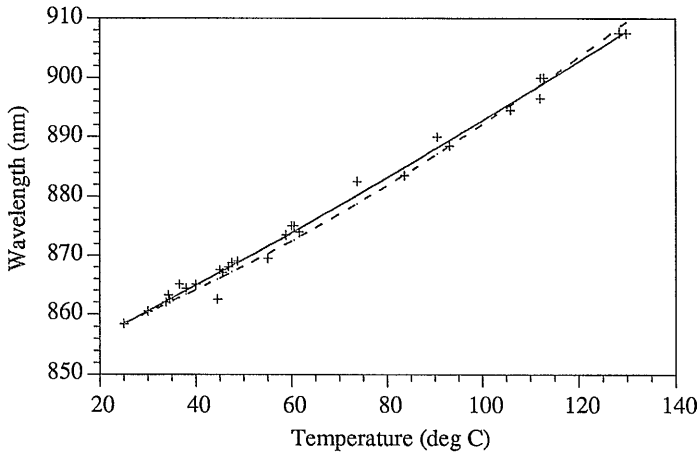


Figure 4.7 - Experimental results of phase matched Wavelength vs Temperature
(Solid line is best fit to Eqn 4.2, dotted line is theoretical curve)

In a review paper by Biaggio et al.⁴, they propose a temperature dependence for the phase matched wavelength which is a second degree polynomial, and have fitted results from seven sources to give the expression:

$$\lambda_{pm} \text{ (nm)} = 850.4 + 0.294(T) + 1.234 \times 10^{-3}(T^2) \quad \text{Eqn. (4.2)}$$

where T is the temperature in °C

This is marked as a dashed line in Figure 4.7. The solid line is a best fit polynomial to the present experimental results giving corresponding coefficients of 848, 0.404 and 4.2×10^{-4} .

The damage coefficient for CW powers in potassium niobate was quoted⁸ as 10 kW/cm². If the laser has a circulating power of 20W then the waist size is restricted to 250µm or greater. The secondary waists were set to an average value of 320µm as

explained in Chapter 3. These were measured in the horizontal and vertical planes by looking at the propagation of the beam through one of the high reflectors and were found to be 300 μm and 350 μm respectively . The intensity profiles are shown in figure 4.8.

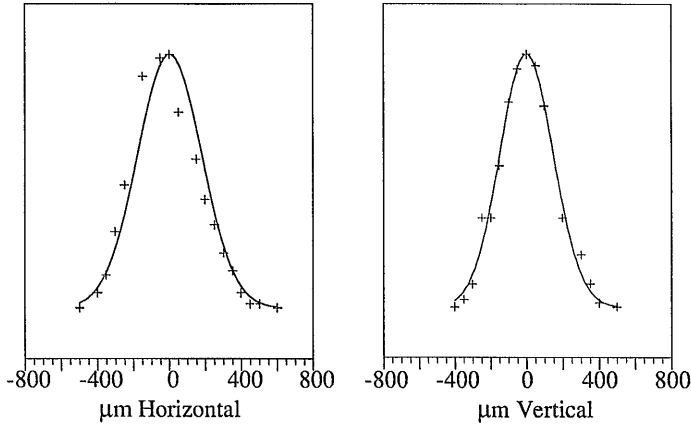


Figure 4.8 - Intensity profiles of the beam as it passes through Secondary focus
(Solid lines are best Gaussian fit to data)

The crystal itself was mounted in an oven which was placed on a prism table within the cavity. The crystal had to be mounted slightly off normal incidence or the power reflected back into the cavity caused the laser to operate bi-directionally.

Acceptance Bandwidths

As explained in Chapter 2 the second harmonic power is given by the expression:

$$P_{2\omega} = \frac{2\omega^2 d_{\text{eff}}^2 \ell^2 P_{\omega}^2 \text{Sinc}^2(\Delta k \ell / 2)}{\pi \omega_0^2 \epsilon_0 n_{\omega}^2 n_{2\omega} c^3} \quad \text{Eqn. (2.5)}$$

If all other factors are constant then the power is directly proportional to the Sinc^2 phase matching term. This can be expressed as :

$$P_{2\omega} \propto \text{Sinc}^2\left(\frac{2\pi}{\lambda_{\omega}} \Delta n \ell\right) \quad \text{Eqn. (4.3)}$$

where Δn is the refractive index mismatch, $n_{2\omega} - n_{\omega}$

Changes in the term Δn , which is zero for perfect phase matching, are mainly caused either by a change in the temperature of the crystal or a change in the orientation of the crystal axes to the fundamental beam. A good indication of the scale of these effects is given by the bandwidth (half width at half maximum) of the Sinc^2 curve describing the variation in second harmonic power as the factor is altered. If the Sinc^2 term $\rightarrow \frac{1}{2}$ full value, then:

$$\frac{2\pi\ell}{\lambda} \Delta n = \pm 1.39, \text{ so } \Delta n = \pm \frac{1.39\lambda}{2\pi\ell}$$

Changes in Power with Angle

For deviations of the direction of propagation away from the a axis in the a-b plane, the refractive index of the second harmonic remains constant at n_c . The refractive index of the fundamental on the other hand is given by:

$$\frac{1}{n_\omega^2} = \frac{\cos^2(\phi)}{n_b^2} + \frac{\sin^2(\phi)}{n_a^2} \quad \text{Eqn. (4.4)}$$

(where ϕ is the angle to the a axis)

Using a Taylor expansion⁹ on this expression for n gives:

$$n(\phi + \delta\phi) = n(\phi) + \delta\phi \frac{\partial n}{\partial \phi} + \frac{(\delta\phi)^2}{2!} \frac{\partial^2 n}{\partial \phi^2} + \dots$$

$$\therefore \Delta n = n(\phi + \delta\phi) - n(\phi) = -n(\phi)^3 \delta\phi^2 \frac{\cos(2\phi)}{2} \left[\frac{1}{n_a^2} - \frac{1}{n_b^2} \right]$$

(The first derivative is zero at $\phi = 0$, so the second derivative is used instead)

Assuming that $n_a \approx n_b \approx n_c$, the HWHM value is given by:

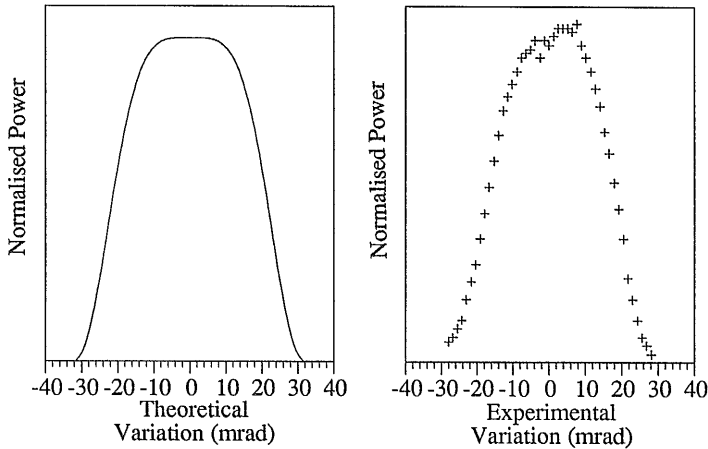
$$\delta\phi = \sqrt{\frac{1.39\lambda_\omega}{2\pi l (n_b - n_a)}} \quad \text{Eqn (4.5)}$$

The refractive indices at 860nm and 430nm are given in Table 4.3. These are the phase matched wavelengths at 30 °C. In general the oven was kept at this temperature to avoid fluctuations caused by room temperature changes.

Wavelength (nm)	n_a	n_b	n_c
430.00	2.4145	2.4974	2.2771
860.00	2.2372	2.2784	2.1338

Table 4.3 - Refractive Indices at 30 °C for the three axes, a, b and c

Using eqn. 4.4 and the refractive indices given above results in a HWHM value of 21.5mrad. The variation of second harmonic power vs angular tuning in the a-b plane is shown in figs. 4.9a and b. The first figure is the theoretical variation and the second is the variation measured experimentally. The experimental HWHM is slightly less than predicted at 18mrad, but as the error in measurement was ± 1.5 mrad this is a reasonably good fit.



Figures 4.9a and 4.9b - Theoretical and experimental variation of second harmonic power with angular variation in the a-b plane

For deviations in the a-c plane the refractive index of the fundamental is constant but that of the second harmonic varies. The HWHM value is dependant on $|(n_c - n_a)|$ rather than $|(n_b - n_a)|$ and the values of the refractive indices are taken at 430nm, not 860nm. The predicted value is 12mrad but was not experimentally measured, as the crystal was only easily rotatable in the a-b plane.

Changes of Power with Frequency/Wavelength

The dependence of the second harmonic on changes in the laser frequency can be found in a similar manner to that given above for angular deviations.

$$\begin{aligned}\Delta n &= n_{2\omega}(\lambda_{sh} + \delta\lambda_{sh}) - n_{\omega}(\lambda_f + \delta\lambda_f) \\ &= n_{2\omega}(\lambda_{sh}) - n_{\omega}(\lambda_f) + \delta\lambda_{2\omega} \frac{\partial n_{2\omega}}{\partial \lambda_{2\omega}} - \delta\lambda_{\omega} \frac{\partial n_{\omega}}{\partial \lambda_{\omega}} \\ &= \delta\lambda_{\omega} \left[\left(\frac{\partial n_c}{2\partial \lambda} \right)_{2\omega} - \left(\frac{\partial n_b}{\partial \lambda} \right)_{\omega} \right]\end{aligned}$$

From this the angular acceptance bandwidth can be calculated as:

$$\delta\lambda = \frac{1.39\lambda_{\omega}}{2\pi l} \left[\left| \left(\frac{\partial n_c}{2\partial \lambda_{2\omega}} - \frac{\partial n_b}{\partial \lambda_{\omega}} \right) \right| \right]^{-1} \quad \text{Eqn.(4.6)}$$

By differentiation of the Sellmeier equation (Eqn. 4.1) the values of $\frac{\partial n_b}{\partial \lambda_{\omega}}$ and $\frac{\partial n_c}{\partial \lambda_{2\omega}}$ were found to be 117414m^{-1} and 999594m^{-1} respectively. From this the wavelength acceptance bandwidth is calculated to be 0.05nm (20GHz). The laser has a free running jitter of less than 40MHz and a cavity mode spacing of 250MHz . Therefore, even mode hops of the cavity should have no effect on the second harmonic output, and indeed observations using a 1.5GHz interferometer showed no detectable correlation between the frequency changes observed and the second harmonic output power.

Changes of Power with Temperature

There are two main effects caused by temperature variations of the nonlinear crystal. The first is the change in phase-matched temperature as the crystal temperature is increased, as shown earlier. Related to this is the temperature bandwidth of the crystal. In this case the term Δn is $\frac{\partial(n_c - n_b)}{\partial T}$. This varies with the overall temperature of the crystal from about $1.25 \times 10^{-4}/\text{C}$ at 30°C to $1.7 \times 10^{-4}/\text{C}$ at 180°C , and is mainly due to the changes in refractive index of the c axis. Figure 4.10a shows the theoretical variation of normalised second harmonic power with temperature. The temperature bandwidth is about 0.15°C at room temperature. Attempts to get a good fit of experiment to theory were not successful, as temperature changes of the crystal had a dramatic effect on the intracavity field, to the extent that the direction of lasing within the ring laser would change direction as the temperature was varied. This effect is shown and discussed later.

Apart from the change in phase matched wavelength, there is another important effect associated with thermally induced refractive index changes in the nonlinear crystal. This is self-induced thermal phase mismatching and is caused by the beam itself. A good explanation of this effect can be found in the work of Okada et al¹⁰. The fundamental beam is partially absorbed by the crystal resulting in a change in the

crystal temperature (and hence refractive index) across the beam profile. To find the total SH power generated the sum of the powers generated at each point across the profile must be calculated. As the intensity of the SH is proportional to the square of the fundamental, the SH is proportional to the Gaussian amplitude raised to the fourth power. This is then integrated across the beam profile(r) while taking into account the change in phase-matching(Δk) caused by the temperature change. This is expressed mathematically as:

$$P_{2\omega} = \text{Const.} \int_0^{\infty} r \exp\left(\frac{-4r^2}{w_0^2}\right) \text{Sinc}^2\left(\frac{2\pi l}{\lambda_{\omega}} \Delta n\right) dr \quad \text{Eqn.(4.7)}$$

The expansion of Δn with regard to temperature is once more a Taylor expansion:

$$\begin{aligned} \Delta n &= \underbrace{(n_{2\omega} - n_{\omega})}_{\Delta n} \Big|_{T_{pm}} + \left(\frac{\partial n_{2\omega}}{\partial T} - \frac{\partial n_{\omega}}{\partial T} \right) \Big|_{T_{pm}} \delta T \\ &= \left(\frac{\partial n_c}{\partial T} - \frac{\partial n_b}{\partial T} \right) \Big|_{T_{pm}} \delta T \end{aligned}$$

where the term δT is the difference between the temperature for which the fundamental wavelength is correctly phase-matched and that of the crystal well away from the centre of the beam. For a large waist or a good thermal conductor this term is always zero, but in general it varies across the beam. Okada assumed a cylindrical temperature distribution and derived an expression for the dependence of SH power on two parameters, a and t , by substitution of this distribution into equation 4.7. The two parameters are:

$$a = \frac{2P_{\omega} \eta \beta}{\lambda_{\omega} K_T} \quad t = \frac{4\pi \beta l \delta T}{\lambda_{\omega}}$$

where η = crystal absorption, K_T = thermal conductivity and $\beta = \frac{\partial(n_{2\omega} - n_{\omega})}{\partial T}$

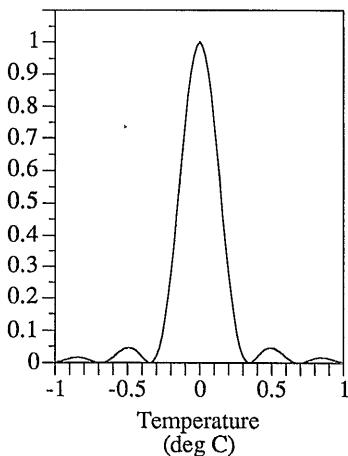


Figure 4.10a

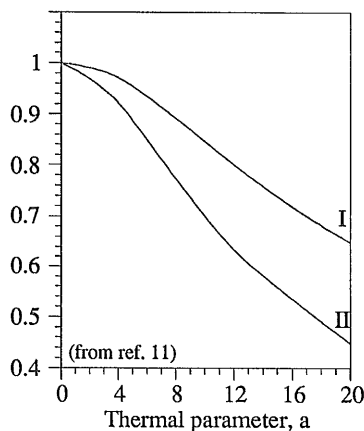


Figure 4.10b

Figure 4.10 - Variation of normalised second Harmonic Power with
a) temperature changes and b) thermal parameter

From this the effect on the SH power can be found for any nonlinear crystal. It is important to note that the best SH is achieved when the wavelength corresponds to perfect phase-matching not at the centre of the crystal, but near the sides of the beam where the induced temperature rise is at an intermediate value, so as to minimise the total phase-mismatching effect. The effect on the normalised SH power is shown in figure 4.10b as a function of the parameter a . The upper curve (I) shows the case of phase matching to the sides of the beam whereas the lower curve (II) shows that of phase matching to the centre of the beam. In general curve I is valid as the wavelength is adjusted for maximum power. For potassium niobate the thermal conductivity is relatively small, $K_T = 0.05 \text{ W/cmK}$ and the absorption, $\eta = 0.01/\text{cm}$. As β is 1.25×10^{-4} at room temperature, this gives a value for a of 11.6, which means that the SH power is roughly 80% of what it would be if the crystal was a perfect conductor.

Another temperature effect was that of the potassium niobate acting as a temperature dependent waveplate due to its birefringence. The effect of both bulk and local temperature changes are illustrated in figures 4.11, 4.12 and 4.13. Figure 4.11 shows the fundamental power circulating in the cavity as measured by the transmission through one of the high reflectors and also the reflection of this power off one of the Brewster cut faces of the Ti:sapphire crystal. The latter trace is a measure of the polarisation of the light circulating in the cavity. The frequency was well away from phase matching so that effects due to frequency conversion are not significant. The

figure is a scan of a chart recording, with the abrupt power changes darkened so that they are distinguishable.

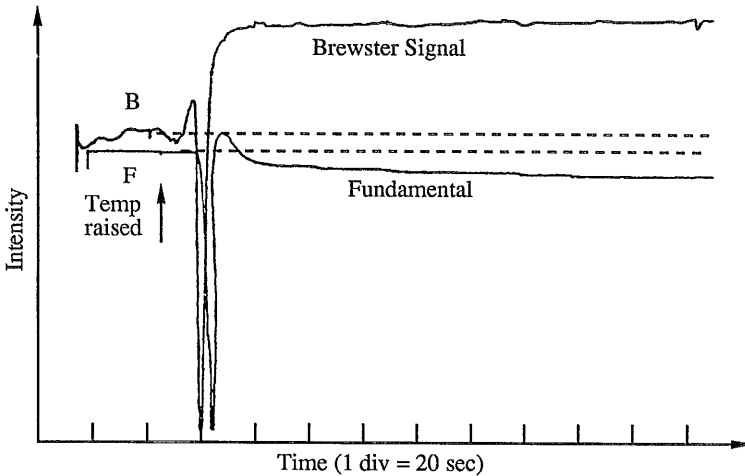


Figure 4.11 - Effect of crystal temperature on cavity polarisation

Initially the two power levels are at an equilibrium set by the doubling crystal and the Ti:sapphire laser components. After a short time the crystal temperature is raised a few degrees, and the polarisation oscillates then kills the lasing completely for a brief period. By observation it could be seen that at this point the lasing had actually changed direction within the ring. The laser then switched direction again and finally settled at a new equilibrium as the temperature stabilised. The final values clearly show the anti-phase relationship between the circulating power and the loss at the Brewster angled face. The loss is now much greater, indicating that the polarisation has rotated further away from the horizontal, while the intracavity power has decreased. This behaviour was seen consistently as the crystal was temperature tuned. Because of this waveplate behaviour, the crystal orientation has to be optimised whenever the temperature is changed. The effect the temperature has on the direction of lasing is seen even more clearly in figure 4.12. The three traces are the second harmonic power, the fundamental power and the reflection of the fundamental off a Brewster angled face (as in fig 4.11).

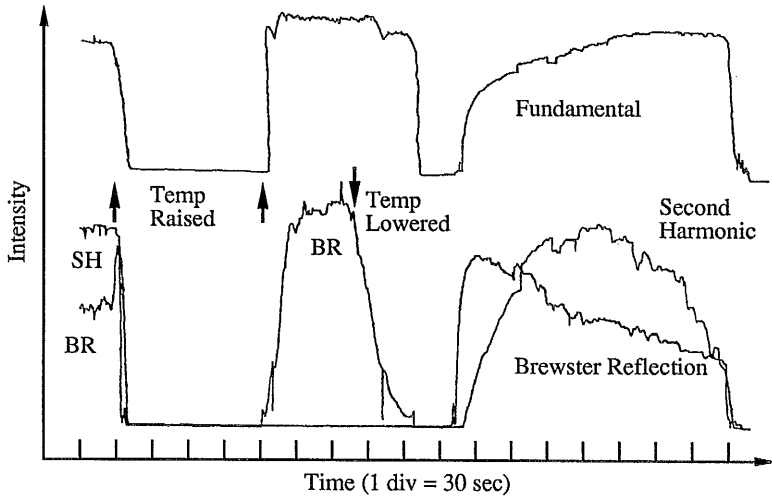


Figure 4.12 - Effect of crystal temperature on lasing direction
(SH = Second Harmonic power, BR = Reflection of fundamental off Brewster face)

The experiment was first set such that the second harmonic was at a maximum. The temperature was then raised a few degrees above phase matching and the laser settled into a state in which the direction of lasing was reversed. A further increase in the temperature changed the direction once more. (At this point the fundamental power was higher than its original value, as was the Brewster reflection. This at first seems like a contradiction of the anti-phase relation between the two, but in fact the proportional change in the reflection is far larger than for the fundamental power. This implies that there are two factors involved - an increase of the power as a whole, which would increase both signals by the same percentage, and a rotation of the polarisation. The reason for the first mechanism is not known but it is possible that reflections of the SH around the cavity can disrupt the laser and lower the fundamental power at phase matching.) The temperature was then decreased to a value lower than its starting point and the laser again changes direction at the same temperature, changes back to sweep through phase matching and then reverses once more.

The effect of self induced temperature changes in the crystal can be seen in figure 4.13. Initially the wavelength was set to give maximum SH conversion, and then the cavity was blocked for about a minute to allow the crystal to cool. The traces show the recovery of the three variables after the cavity is unblocked.

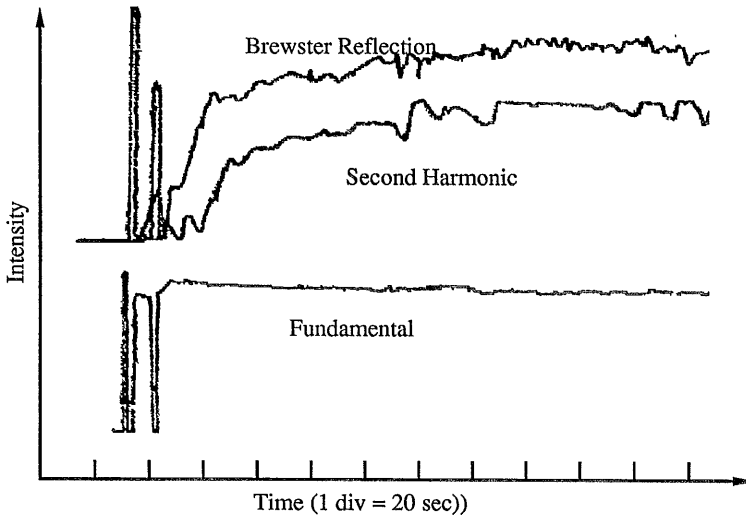


Figure 4.13 - Self induced phase-mismatching effects

As soon as the laser is unblocked there is a brief transition period before the fundamental power reaches a stable power level. At the same time the polarisation starts to vary, causing the laser to briefly switch directions and then settle once more to a stable level. At this point the second harmonic power starts to rise and after a period of about two minutes has once more reached a steady state. It can be seen that there is a close correlation between the Brewster reflection and the SH power. This is more likely to be due to the fact that they are both affected by the heating of the crystal than that the polarisation change is itself affecting the SH power to this extent. The polarisation of the fundamental would have to rotate over several degrees before the component along the b axis decreased enough to affect the SH power to the extent seen. The relation between the polarisation and the SH power is discussed later and the size of the effect is calculated.

According to the calculations done earlier the thermal effect the fundamental has on the phase-matching should lower the power by 12% at a fundamental power of 15W. Although it is clear from figure 4.13 that the fundamental is heating the crystal, the effect of mismatching across the beam was not obvious. Figure 4.14 shows the power generated at 430nm vs the fundamental power. The line shown is a best quadratic fit to the data.

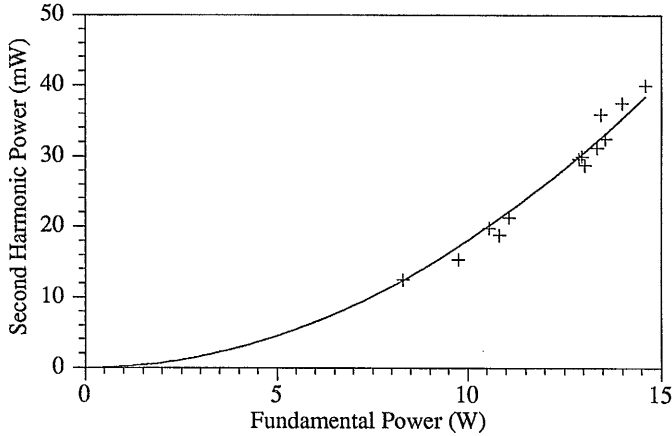


Figure 4.14 - Power at 430nm vs Power at 860nm

It can be seen that the data are a close fit to the quadratic curve, and that the characteristic tail-off of power due to phase mismatching across the beam is not obvious. There are two possible explanations for this. The first is that the effect is lost in the variations of the output power. (The reasons for the variations are discussed later). This is typically about $\pm 10\%$ and so a drop of 12% could be lost in experimental error. However the results were taken of the average power value and although the power out vs circulating power was measured on several occasions the effect was never detectable. The second reason is that the thermal conductivity is better than the value of 0.05W/cmK used in the calculations. The thermal conductivity was hard to find as it was unknown by the manufacturers and that used here is from a paper published in 1979⁵. It is possible that the growth techniques have improved the conductivity since then. If one uses a cylindrical temperature distribution for the temperature changes produced by the absorbed power in the crystal^{10, 11}, then a reasonable approximation to the radial(r) temperature change is:

$$T(r) = \frac{-\eta P_{\omega}}{2\pi K_T} \exp\left(-\frac{r^2}{w_0^2}\right) \quad \text{Eqn (4.8)}$$

The temperature change expected given a circulating power of 15W is shown for several values of the thermal conductivity parameter, K_T , in figure 4.15.

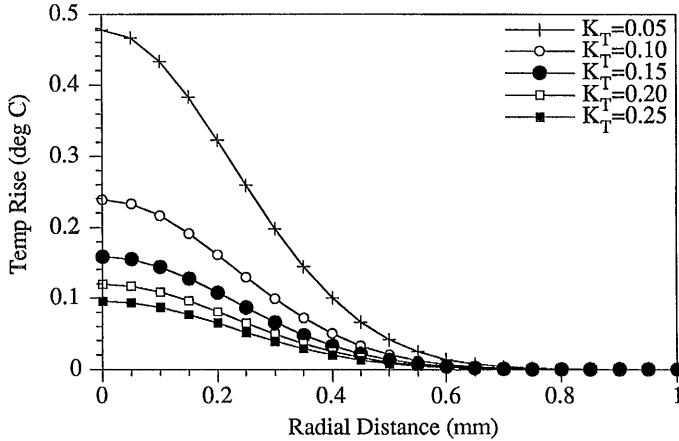


Figure 4.15 - Radial temperature variation produced by absorption

It can be seen that although a change in the thermal conductivity from 0.05/cmK to 0.1/cmK will change the thermal parameter, a , from 11.6 to 5.8 (which would reduce the power to only 97% of maximum as opposed to 88% at 15W) the temperature of the crystal where the beam passes through it is between 0.1 and 0.24° above the background. As the power is reduced to half its maximum for a temperature change of 0.15°, this change in the temperature above the background would reduce the power by between 20 and 90% when the crystal is cool. As the two effects (overall temperature change and change across the beam) are related they must both be present. It seems most likely that the value for the conductivity is somewhere between 0.05 and 0.1W/cmK, so that although the tail-off is not obvious, the change in background temperature is enough to affect the phase-matching wavelength.

Efficiency and Power

The potassium niobate crystal was usually set at an angle of about 2-5° to the normal. This was necessary to prevent back reflections but has a slight effect on both walkoff and the nonlinear coefficient. At 5° the walkoff angle (ρ) is no longer zero but instead is given by eqn 2.12 such that :

$$\rho = \tan^{-1} \left(\frac{1}{2} (n_b(\omega))^2 \left(\frac{1}{(n_c(2\omega))^2} - \frac{1}{(n_a(2\omega))^2} \right) \sin(10^\circ) \right) = 0.55^\circ$$

From this the walkoff(aperture) length can be calculated from eqn 2.13. For a waist size of 320 mm this length is 59mm, which is far longer than the crystal length of 10mm. The walkoff is therefore insignificant.

The nonlinear coefficient for potassium niobate using the d_{32} coefficient is quoted by the manufacturers as 18.3pm/V at 1064nm. Using Millers rule (eqn 2.16) this allows the value at any other frequency to be calculated by:

$$d_{32}(\omega) = \frac{18.3(n^2(2\omega) - 1)(n^2(\omega) - 1)(n^2(\omega) - 1)}{(n^2(532\text{nm}) - 1)(n^2(1064\text{nm}) - 1)(n^2(1064\text{nm}) - 1)}$$

For tuning in the a-c plane the effective nonlinear coefficient is $d_{32} \sin(\theta)$ and so the coefficient is decreased by less than 0.38%. Taking these two factors into account gives a value for the nonlinear coefficient at 860nm of about 21pm/V.

The laser was usually run with circulating fundamental powers of 20W. The peak power measured in the blue was 50 mW at a fundamental power level of 21.3W. A more usual day to day value was 30mW. It was found to be quite tricky to get the best alignment of the crystal within the cavity. Changes in alignment of the crystal affected the circulating power and consequently the self induced thermal effects and phase matching wavelength. The values of SH power vs wavelength typically available using this method are shown in figure 4.16.

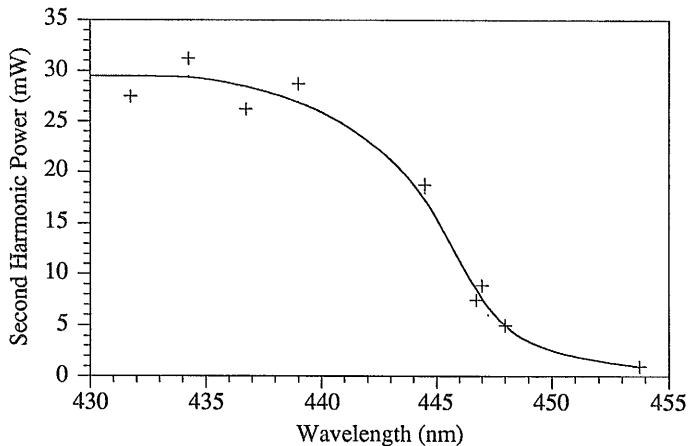


Figure 4.16 - Second Harmonic Power vs Wavelength

The decrease in the power with wavelength is due to the fundamental laser powers rather than the efficiency of the SH generation. The reflectivity of the coatings

drops off over this region and so a better idea of the conversion efficiency can be found by measuring $P_{2\omega} / P_{\omega}^2$, which should be constant provided (as in this case) the fundamental depletion is low. The values of $P_{2\omega} / P_{\omega}^2$ over this wavelength range are shown in figure 4.17.

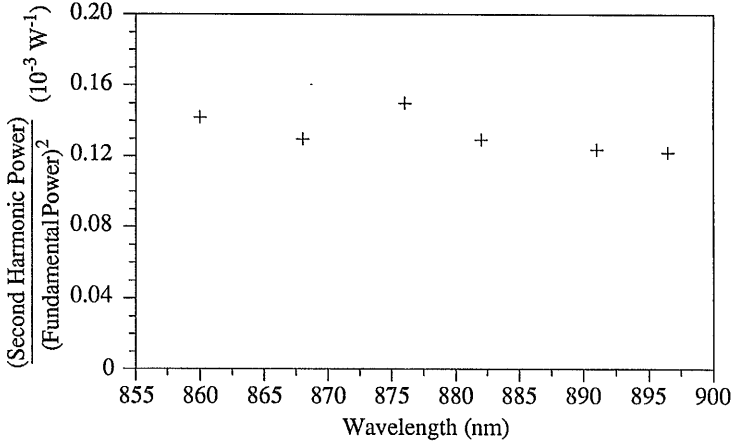


Figure 4.17 - Relative conversion efficiency vs Wavelength

This graph shows that the relative conversion efficiency remains at the same value, $\pm 10\%$, over the whole tuning range so that with the appropriate mirrors the powers should remain roughly constant. In fact a slight reduction can be expected due to the decrease in the nonlinear coefficient at higher wavelengths, but this would only be of the order of 5%.

The theoretical second harmonic power is given by eqn 2.5. This is also modified by the self induced phase mismatching term which is dependent on the fundamental power. Using the values for the refractive indices, waist size, crystal length and nonlinear coefficient given previously gives the expected out power as:

$$P_{2\omega} = 4.45 \times 10^{-4} \times P_{\omega}^2 \times T_a$$

(where T_a is the thermal reduction term dependent on a)

For the maximum SH output of 50mW the fundamental power was 21.3 W and the term T_a was 0.8 (using $K_T = 0.05 \text{ W/cmK}$). This gives an expected power of 161mW and so the SH was only 31% of that expected. The best conversion efficiency was for a circulating power of 11.76W ($T_a=0.9$), for which the output was 22.5 mW as opposed to a calculated value of 55mW. This gave a conversion efficiency with respect to theory of 41%. These results were disappointing given the high conversion efficiencies that

should be expected from potassium niobate by its nonlinear coefficient, but are comparable to those of Baumert et al (using cw dye lasers), who also found that the conversion was roughly 40% of that expected. The results of Polzik and Kimble are for a shorter crystal(6mm) and a smaller waist size(20 μ m) but give a value for $P_{2\omega} / P_{\omega}^2$ of 0.005W⁻¹. When converted to the waist and crystal length used here this gives a value of 5 x 10⁻⁵W⁻¹, a third of the one seen in this experiment.

Power Variations

Figure 4.18 is similar to figure 4.13, but the intensity changes are monitored over a longer time period as the system is running. This plot was used to look at the typical variations in the second harmonic and to see what effect the polarisation and fundamental power changes had on the SH. By measurement these variations are:

$$\frac{\Delta P_{\omega}}{P_{\omega}} = \pm 1.7\%, \quad \frac{\Delta P_{BR}}{P_{BR}} = \pm 6.1\%, \quad \frac{\Delta P_{2\omega}}{P_{2\omega}} = \pm 13.4\%$$

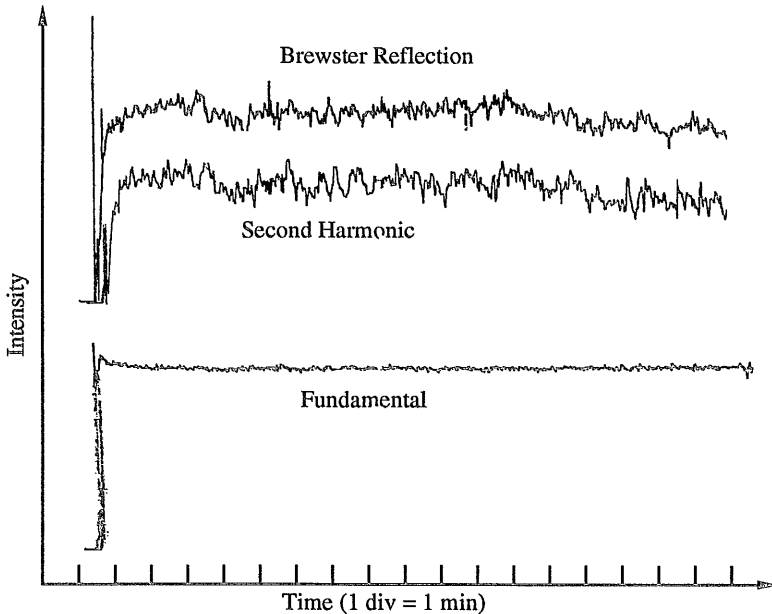


Figure 4.18 - Free running intensity variations of second harmonic, fundamental and Brewster reflection

i) Effect of ΔP_{ω} on $\Delta P_{2\omega}$

As the SH is proportional to the square of the fundamental, a $\pm 1.7\%$ change in the latter will produce a $\pm 3.4\%$ change in the former. This still leaves $\pm 10\%$ unaccounted.

ii) Effect of polarisation changes on $\Delta P_{2\omega}$

By measuring the amount of light reflected off the Brewster angled face in the cavity one can find what percentage of the fundamental beam is polarised vertically within the cavity. For a total circulating power of 19.72W (as measured through a high reflector) the intensity of the vertical component (P_{\perp}) is 28mW. The circulating field is therefore polarised at an angle of 2.2° to the horizontal. A change in the reflected power of $\pm 6\%$ means that this angle is changing by $\pm 0.15^{\circ}$. Assuming that the crystal is initially well phase-matched, this change only leads to a variation of 0.0007% in the second harmonic power.

iii) Effect of ΔP_{ω} on temperature of crystal and hence on $\Delta P_{2\omega}$

Using eqn 4.8 one can find the variation of the temperature change produced by absorption of the fundamental. For a 1.7% variation in the fundamental power of 19.7W, the temperature change is $\pm 0.01^{\circ}$. From graph 4.10a this should make little difference provided the beam is well phase matched to begin with. However the temperature controller itself is only rated to $\pm 0.05^{\circ}\text{C}$, and a variation of this size will produce a change of $\pm 8\%$. If instead of being perfectly phase matched the temperature is set to slightly off optimum, as it will be to counteract the effects of self phase mismatching, then the scale of temperature variations is greatly increased. Figure 4.19 is a magnification of figure 4.10a, showing the changes in SH power as the crystal temperature changes.

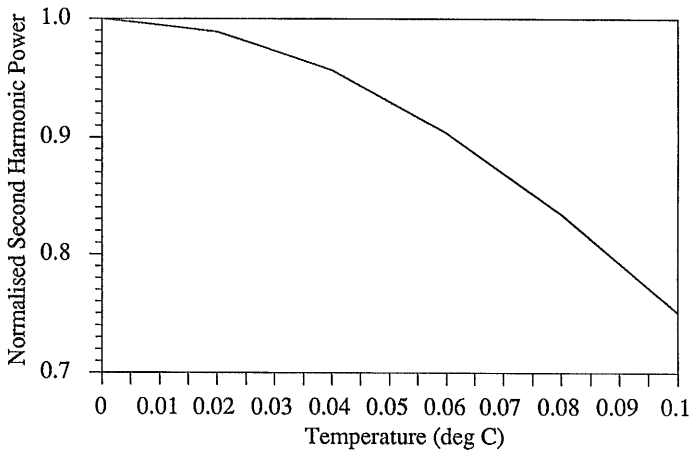


Figure 4.19 - Second Harmonic Power Variations with Temperature

From this one can see that if the temperature is offset by 0.05° to begin with, then variations of the same magnitude will be of the order of $\pm 12\%$.

Conclusion

The scheme described above demonstrates a straightforward method of obtaining cw blue powers of up to 50mW from a Schwartz Ti:sapphire laser. Although potassium niobate is still the only material with which one can get any powers above mW levels by doubling the Ti:sapphire laser in the region around 900nm, it is far from an ideal material. The relatively low damage threshold limits the extent to which the radiation can be focused into the crystal, (for similar damage reasons the use of lithium iodate in the lower wavelength range has now been superseded by lithium triborate^{12,13}) and the poor thermal qualities both limit the conversion efficiency through thermal phase-mismatching and pose a stringent accuracy limit on the temperature controller used. However, if one does not need large power levels and are prepared to tolerate power fluctuations or use a high accuracy temperature controller then a Ti:sapphire laser and potassium niobate are still the best way to get tunable blue radiation from 430nm to 470nm.

References

- 1 R G Smith - Theory of Intracavity Optical Second-Harmonic Generation - IEEE J.QE, vol QE-6, No. 4, 1970, pgs215-223
- 2 E S Polzik and H J Kimble - Frequency doubling with KNbO_3 in an external cavity - Optics Lett., Vol. 16, No. 18, Sept 1991, pgs 1400-1402
- 3 B Zysset, et al. - Refractive indices of orthorhombic KNbO_3 . I. Dispersion and temperature dependence - J. Opt. Soc Am. B, vol. 9, no. 3, March 93, pgs 380-386
- 4 Biaggio et al. - Refractive indices of orthorhombic KNbO_3 . II. Phase-matching configurations for nonlinear-optical interactions - Opt. Soc. Am. B., Vol. 9, no. 4, April 1992, pgs 507-517
- 5 M M Mebed et al. - Thermal properties of KNbO_3 crystals in the temperature range 350-700K - Rev. int. hautes Tempér. Refract. Fr., 1979, vol. 16, pgs 340 - 345
- 6 G Mizell and W Kay - Ferroelectric Domains and Optical Absorption in potassium niobate crystals - Communication from Virgo Optics, Division of Sandoz Chemicals Corporation, 1990
- 7 J.-C. Baumert et al.- Nonlinear Optical effects in KNbO_3 crystals at $\text{Al}_x\text{Ga}_{1-x}\text{As}$, dye, ruby and Nd:YAG laser wavelengths - SPIE vol. 492, ECOOSA 84, pgs 374-385
- 8 Rene Baar, Private communication from Sandoz optoelectronics, 1990
- 9 A Yariv - Optical Electronics - 3rd Ed., CBS College Publishing, 1985
- 10 M Okadu and S Ieiri -Influences of self-induced thermal effects on phase matching in nonlinear optical Crystals - IEEE J.QE, vol. QE-7, No. 12, pgs 560-563
- 11 A I Ferguson - Frequency Doubled Continuous Wave Dye Lasers - Ph. D Thesis, St. Andrews University, 1977
- 12 C S Adams and A I Ferguson - Tunable narrow linewidth ultra-violet light generation by frequency doubling of a ring Ti:Sapphire laser using lithium tri-borate in an external enhancement cavity - Opt. Comm., Vol. 90, No. 1,2,3, pgs 89-94, 1992
- 13 S Bourzeix et al - Efficient frequency doubling of a continuous wave titanium:sapphire laser in an external enhancement cavity - Opt. Comm., Vol. 99, No. 1, 2, pgs 89-94, 1993

Chapter 5

Frequency Stabilisation and Scanning of Laser

In Chapter 2 there is an outline of the most commonly used methods of frequency stabilising laser sources. This chapter will deal with the methods used to turn the basic Ti:sapphire laser into a spectroscopic source capable of sub-MHz resolution. In addition there is a section on the conversion of the laser to a scannable source. This work was successful in producing a single longitudinal mode which could be scanned over 10GHz. Techniques suitable for producing a longer, more reliable scan are also described.

Stabilisation

Passive Stabilisation

As always, the first step in laser stabilisation is to improve the passive stability of the laser. The laser used here is a breadboard system with modular components. This makes the laser very easy to adapt and it has in fact been altered both for intracavity doubling, in which the soft secondary waist was tightened as described in Chapters 3 and 4, and also for tighter focussing work in which an extra folding section was inserted between the two flat reflectors. The disadvantage of the modular system is that each component is capable of independent movement and the level of stability gained by making the laser of one unalterable piece is lost. As the laser has formed part of several different projects so far there are only three passive techniques which do not compromise the experiments for which the laser was and is used. The first technique is to decouple the breadboard from the optical table by a solid foam cushion. The table itself was incapable of floating on its pressurised legs due to the weight of the argon ion pump laser and so was not isolated from vibrations through the floor. The cushion instead has something of the same effect. The second somewhat prosaic but useful method was to replace the two independent mirror mounts with more solid (but less adjustable) models. The third and most useful measure was to build a customised box to fit over the laser itself, in order to reduce the acoustic pick-up of the laser from the surrounding environment. The box was made of wood with an inner lining of anechoic foam to cut down on acoustic resonances and transmission of environmental noise. The input and output beams were guided through short tubes to cut down on draughts and provision was made for the whole enclosure to be kept at an over pressure of nitrogen. The three passive stabilisation techniques used are shown in figure 5.1.

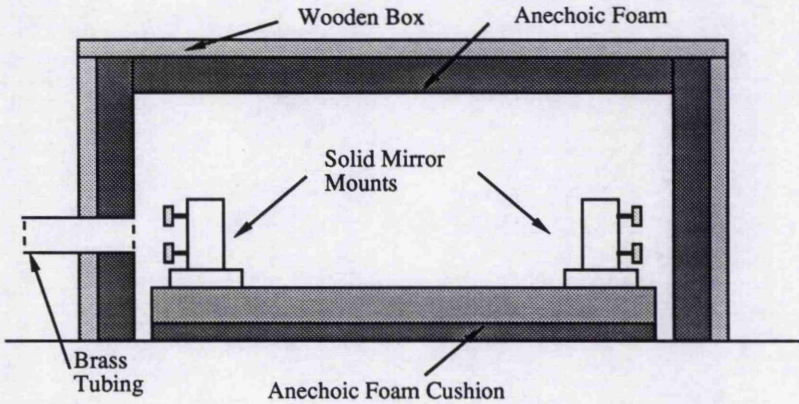


Figure 5.1 - Passive Stabilisation Measures

These provisions kept the short term (<1 second) frequency perturbations down to 5MHz, but the temperature variations still caused the output frequency to drift by 10 to 30 MHz over a few minutes. The spectral power density of the frequency perturbations was measured using a spectrum analyser and is shown in Figure 5.2.

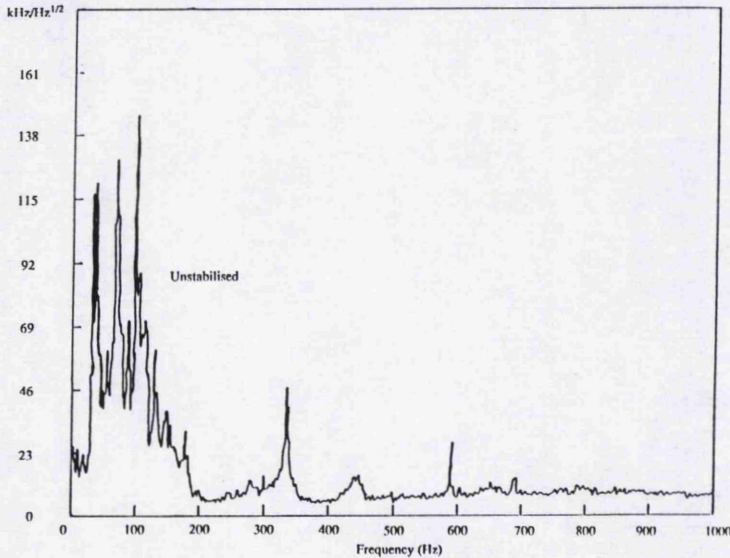


Figure 5.2 - Spectral Analysis of Noise Components of Passively Stabilised Laser

The spectrum is taken by analysing the deviations from the side of fringe transmission of a confocal interferometer over a period of about a minute. The response is measured linearly and the resolution is to 2.5Hz. It can be seen that the majority of

the noise is well below 1kHz and in fact apart from two components at 330Hz and 590Hz the noise is mostly below 200Hz. The magnitude of the noise components below about 50Hz is quite variable as will become obvious in later spectra. These components depend greatly on doors closing, people walking and talking and other such variable background noise.

Active Stabilisation

Once all reasonable measures were taken to reduce the passive noise the laser was adapted for active stabilisation. The two components added to the cavity to compensate for changes in cavity length were a pair of rotating galvanometer mounted Brewster angled plates and a piezo mounted mirror. As explained in Chapter 2, the plates can correct for large changes in laser frequency but only at low perturbation frequencies, while the piezo mirror responds rapidly to correct smaller laser frequency deviations. The method used for stabilisation is to lock the laser output to the side of a transmission fringe of a confocal etalon. The interferometer arrangement for both stabilisation and scanning has been shown previously in figure 3.6. The static confocal interferometer to which the laser is locked has a free spectral range of 300MHz and a finesse of 2.1. The relatively low finesse ensures that an appropriate error signal is generated for frequency deviations of at least 70MHz and so reduces mode hops due to overshooting of the plates or large frequency deviations but also reduces the size of the signal to noise ratio for a given frequency change.

The third component of the servo loop is the electronic control of the length correction elements. The scheme used was relatively simple and the circuit diagrams for the electronics are shown at the end of the chapter as figures 5.a-5.d. The first stage is the light balance and the amplifier of the error signal. Two photodiodes, placed back to back, are used as the input to the control box. If only the power transmitted through the etalon was monitored, then any intensity noise in the laser would be interpreted as a frequency change. However, if the intensity of the laser itself is also monitored, then by adjusting the light incident on the compensating photodiode such that the error signal is zero when the frequency is locked to the side of the transmission fringe, the variations in laser intensity give equal and opposite contributions from the two photodiodes and so cancel. The resulting error signal is then split in two and processed to drive the galvanometers and the piezo separately. In both cases there are two factors which must be taken into account - the resonant frequency of the component and the phase of the correction voltage. The galvanometers have their resonance frequency at 260Hz and are used to compensate for the low frequency perturbations, in particular the large but sub-Hz thermal drifts. The plates could, if needed, correct for GHz perturbations, but this is well above the passive stability of the laser. In order to best correct for these slow changes in laser frequency the error signal was integrated, and to avoid the galvo

resonance the time constant was set to 100Hz. The output was then sent through a variable gain amplifier and input to the galvo drivers. The contribution of the tilting plates to noise suppression is seen clearly in figure 5.3. This shows the error signal when the laser is unstabilised, when it is stabilised just on the tilting plates, and when the plates and the piezo are both used. The servo mechanism using the tilting plates works best at frequencies from dc to 50Hz and rolls off to provide virtually no compensation at 100Hz. The trace is plotted for noise in frequency bands from 0 to 200Hz on a logarithmic scale relative to an internal voltage source of the spectrum analyser.

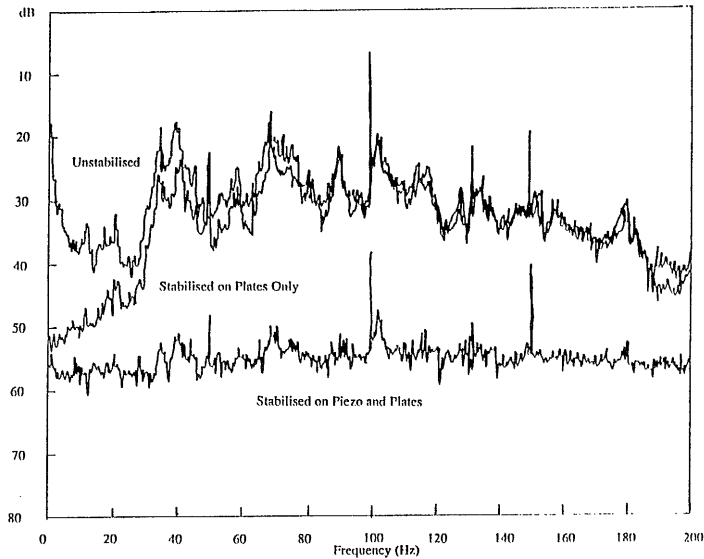


Figure 5.3 - Spectral analysis of tilting plate contribution to noise suppression

The resonance frequency of the piezo ceramic mounted mirror is much higher and is usually somewhere between 20kHz and 30kHz. The actual value is dependent on the current source used to drive the piezo itself. With the current output from a function generator the resonance was measured as 18kHz but when controlled by the high voltage amplifier it was about 50% higher. This fits well with the theoretical calculation, given that the unloaded resonance frequency of the disc piezo is 1000kHz and the mirror's weight was roughly twice that of the piezo. Two approaches were tried to control the output of the voltage signal to the signal. The first used a 6 pole low pass Bessel filter with a cut off (-3dB point) of about 4kHz. Using several filters increased the sharpness of the cut-off, but unfortunately also increased the phase delay of the

feedback signal, and sent the piezo into oscillation at a lower frequency than its resonance. The second approach was to use a single 2 pole Bessel filter. As most of the laser noise is below 1kHz anyway, the suppression of higher noise components is only necessary for very accurate stabilisation. Instead the -3dB point was set at 1kHz so that most of the laser noise had a good response from the servo system but without the phase delay caused by cascaded filters, and the response was negligible at the piezo resonance. The resulting signal was then sent through a high voltage amplifier where the response could swing through $\pm 75V$, large enough to correct for deviations of $\pm 13MHz$.

When the laser was stabilised using both the tilting plates and the piezo mounted mirror the laser frequency jitter dropped from tens of MHz to a level of 0.50-0.75MHz. This was measured using the variation in transmission of the reference etalon.

Residual Noise Levels

Figure 5.4 shows the transmission of the reference etalon as the laser is scanned over several free spectral ranges.

Scope Levels:
 V: 200mV/div
 H: 20ms/div

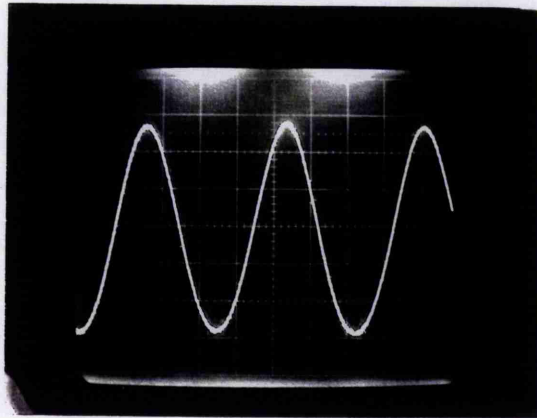


Figure 5.4 - Transmission of Reference Etalon

The laser is light balanced to give an error output of 0V half way up the transmission fringe and at this point the slope gives an error of 92.5kHz/mV. The finesse of the etalon is 2.1. Figure 5.5 is the error signal when the laser is stabilised. The vertical scale is now 100 times larger than in the previous figure.

Scope Levels:
 V: 2mV/div
 H: 20ms/div

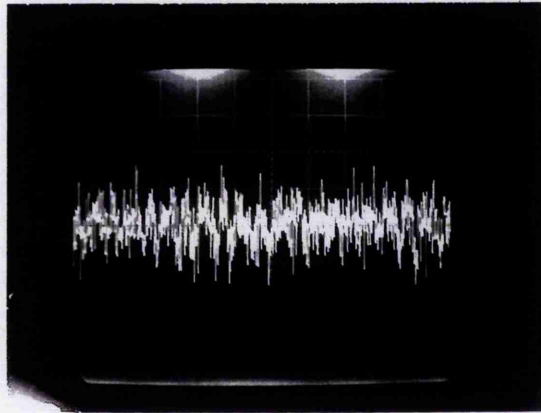


Figure 5.5 - Error Signal when Stabilised

Most of the noise is now contained within 4mV (corresponding to frequency fluctuations of 370kHz) with spikes out to 6mV (frequency fluctuations of 550kHz). This is close to the value at which the system is limited by electronic background noise within the system. This noise is shown in figure 5.6 which has the same scales as the previous figure. The background noise would correspond to frequency fluctuations of 140kHz.

Scope Levels:
 V: 2mV/div
 H: 20mS/div

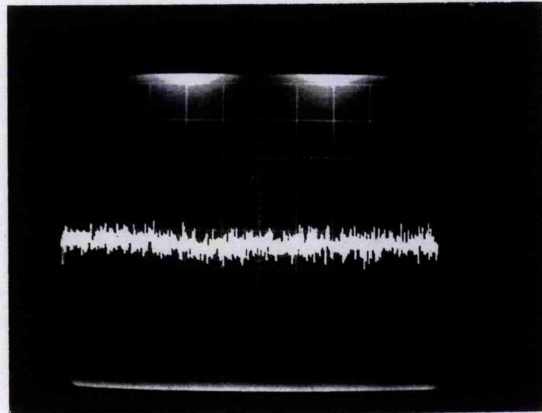


Figure 5.6 - Background Noise

Achieving the sub-MHz stability levels seen above is due to the corrections by the piezo driven mirror. Without the piezo the laser only stabilises to about 4MHz. The error signal when the piezo is switched off is shown in figure 5.7. (The vertical scale is

5 times larger than in the last two figures). The noise component at 100Hz, where the plates do not compensate, is now particularly evident.

Scope Levels:

V: 10mV/div

H: 20mS/div

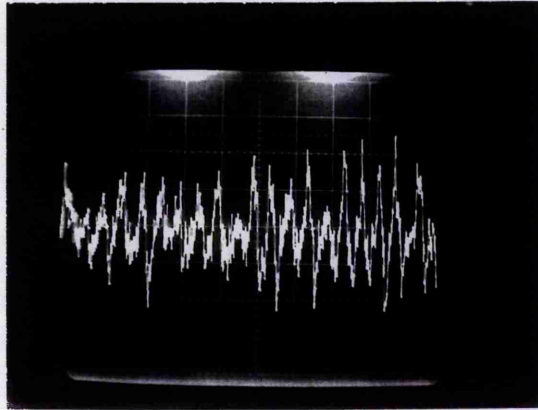


Figure 5.7 - Error Signal when stabilised only by tilting plates

This does not make the plates redundant because without them the piezo can only hold the stability for a short period of time before saturating to the upper or lower rail as the laser drifts by more than 13MHz. Both components are necessary to achieve a high level of long term stability. The gain of the servo system acting through the piezo ceramic mirror was measured at 20 Hz and found to be 16. At the -3dB point this would drop to 8. As the noise is roughly 4MHz when not stabilised on the piezo, one could expect from eqn 2.17 that the stabilised noise level would be somewhere between 235kHz and 445kHz, which ties in well with the measured stability of 370kHz - 550kHz.

The response of the stabilisation system to the frequencies of the noise components is seen in the following spectrum analyses. The first, figure 5.8, like 5.2 is a linear response to the noise and shows the unstabilised signal, the stabilised signal and the background noise of the analysis system over a 1kHz range. For a 1kHz range the sample size is 2.5Hz.

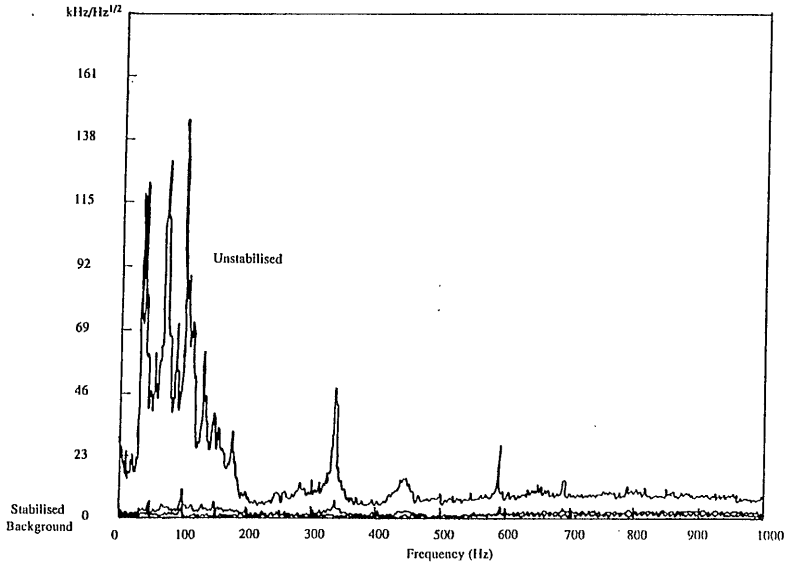


Figure 5.8 - Spectral power Density of Unstabilised, Stabilised and Background Noise

In a linear trace such as this the stabilised signal is very close to the background level and it is more useful to look at the noise components on a logarithmic plot. Figures 5.9 - 5.11 are log plots of the same stabilisation signals also over three ranges, 500Hz, 1kHz and 10kHz. The sample sizes over these three ranges are 1.25Hz, 12.5Hz and 25Hz. The full scale level is 80dB in each case.

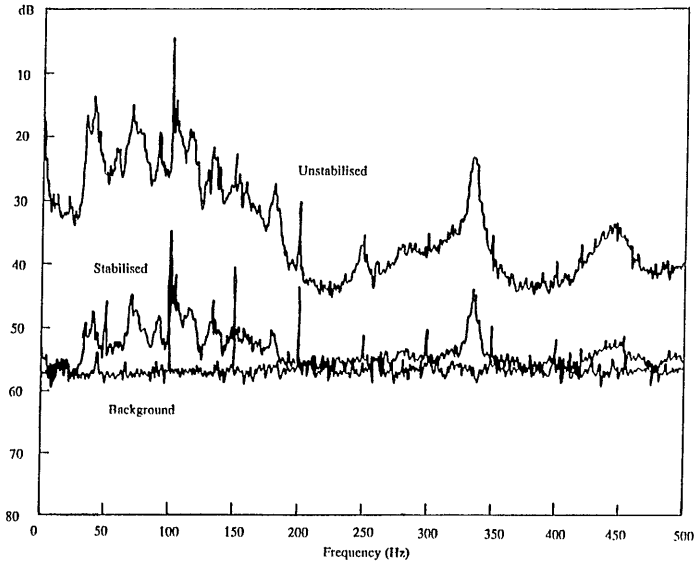


Figure 5.9 - Log Plot of Unstabilised, Stabilised and Background Noise over 500 Hz

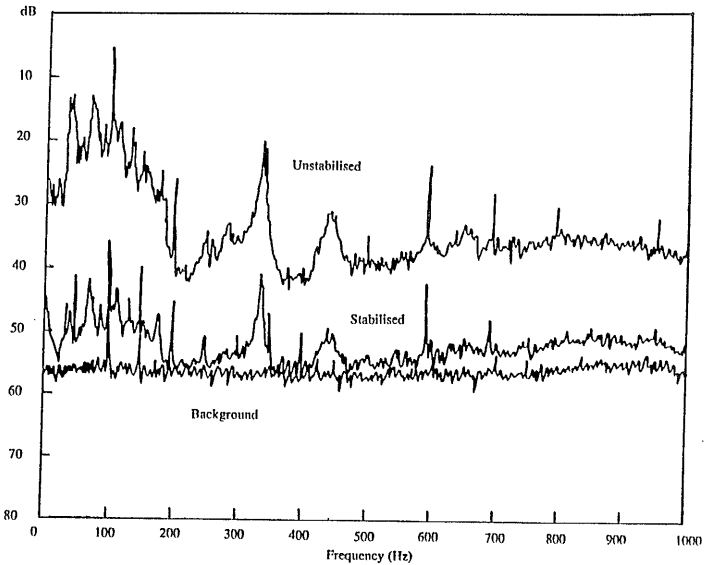


Figure 5.10 - Log Plot of Unstabilised, Stabilised and Background Noise over 1 kHz

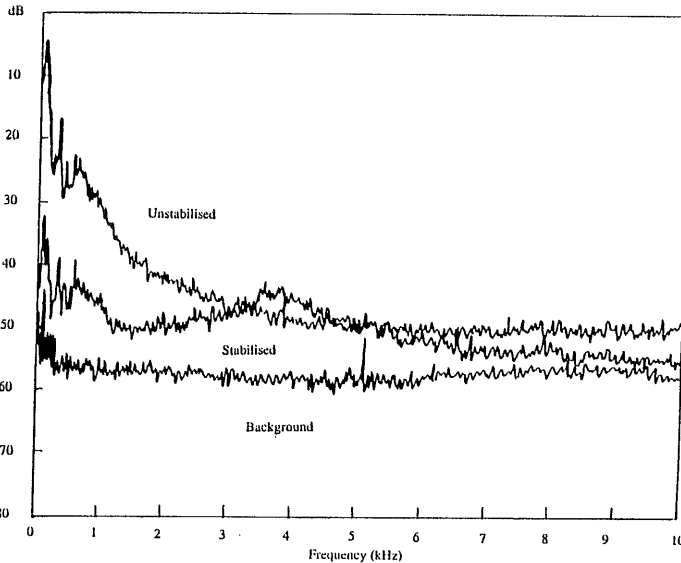


Figure 5.11 - Log Plot of Unstabilised, Stabilised and Background Noise over 10 kHz

It can be seen that below 200Hz (fig 5.9) the noise levels are 20-30dB down on the unstabilised noise, and that the stabilised noise is only 0-15dB above the background. The most consistent noise elements are the mains hum at multiples of 50Hz. In figure 5.11 the resolution of the traces are lost as the sample size is 25Hz, but the figure shows the suppression of the noise up to 3kHz. The stabilisation electronics themselves add a noise component at about 3.6kHz which is 5dB above the unstabilised signal. It is usual that stabilisation circuits add some noise and this contribution is not too large.

Conclusion

The system described above reduces the noise of the laser to sub-MHz levels without compromising the versatility of the laser. This level of stability is comparable to that of most commercial dye lasers and is suitable for most spectroscopic applications. Further improvements could be made if required by increasing the response and bandwidth of the servo loop, but stability down to Hz levels would require both a better passively-stabilised laser and a Pound-Drever stabilisation scheme¹.

Laser Scanning

At the beginning of this chapter it was mentioned that the conversion of the laser to a fully scanable source was partially successful. The laser was capable of scanning up to 10GHz, but only with a degree of care and attention in setting the appropriate voltage levels for the tracking etalon. This section will outline the method used (dead reckoning) and its limitations, and will describe a more recent approach which it is hoped will be more reliable. It is in reliability that the dead reckoning method falls down. A fully scanable laser should be capable of starting from any given point in its tuning range and scan, without mode hops, over a range of at least 20GHz. In this way a series of overlapping scans can cover the entire tuning range of the laser. If the scanning system must be reset each time the tuning range is changed, or from day to day, then considerable time is lost which is better spent on the actual experiments. The dead reckoning system was still of considerable use, as can be seen in figure 5.4 where the finesse of the etalon was measured by scanning the laser, and more particularly will be seen in Chapter 7 where phase matching in vapours is studied. In this second application the frequency of the dye laser was kept fixed and the frequency of the Ti:sapphire laser was repeatedly scanned rapidly up and down across the Doppler width of the generated ultraviolet as the temperature of the vapour was changed. Any mode hops in the scan are insignificant compared to the Doppler width and so the laser will always find the maximum of the transition. An example is shown in figure 5.12.

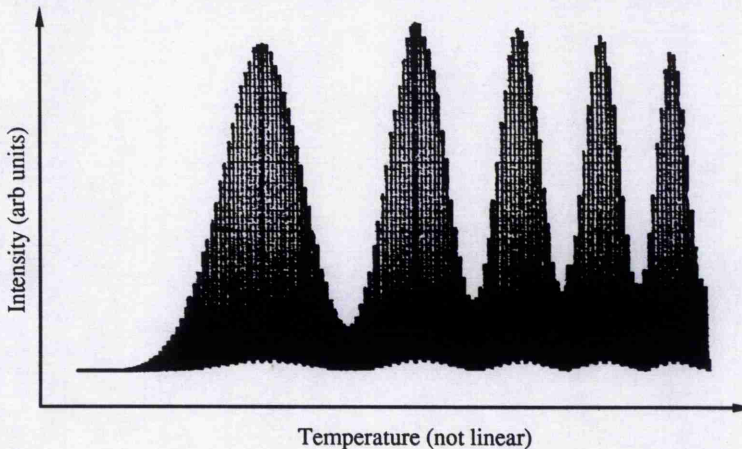


Figure 5.12 - Scanning Ti:sapphire Laser used to look at Phase Matching Behaviour

In the figure above are five of the phase matching peaks found by altering the vapour temperature. Each peak is composed of dozens of Ti:sapphire laser scans over

about 10GHz. This technique was used often to look at bulk phase-matching effects under different conditions.

'Dead Reckoning' Method of Scanning

In Chapter 3 is a description of the equipment used to scan the cavity. This consists of the two rotating plates also used in stabilisation and the etalon necessary to keep the cavity on a single longitudinal mode. All three are mounted on galvanometers controlled by drivers constructed at the university. The plates are 4mm thick and scan the cavity linearly at a rate of 20.42GHz/degree (eqn. 3.1). For small changes from normal incidence, the change in etalon transmission is given by eqn. 3.2:

$$\Delta v = \frac{v\theta^2}{2n^2} \quad \text{Eqn. (3.2)}$$

The idea behind a dead reckoning circuit is that provided the etalon is initially set at normal incidence and the voltage controlling it is the square root of that controlling the plates then with the appropriate gain on one or the other the two should always track each other. This is true whether the controlling signal originates from a signal generator or when the cavity is locked to the error signal of the reference etalon as it itself is scanned. As the laser hops from one thin etalon mode to another as the birefringent filter is turned, the laser has to be able to cover the whole of the interval in-between. This is 150GHz for the 1mm thin etalon used. By adding an offset to the signal controlling the etalon before it is square rooted the laser can be set to scan over any part of this 150GHz range. The scanning/stabilisation loop is shown in figure 3.9. (For scanning without stabilisation the confocal etalon and stabilisation control are removed). The problems arise in keeping the maximum transmission of the etalon exactly on the scanning frequency. The most common error was that during the scan the laser would hop up or down a cavity mode, or more frustratingly be unable to decide between two adjacent modes and hop back and forward repeatedly during the scan. Two other uncoated etalons (2mm and 3mm) were tried to provide better discrimination between the modes but with no more success. The discrimination did not seem to be the problem, as the laser happily kept to a single mode throughout, but the tracking of the plates and the etalon was not consistent. As the cavity modes of the laser are spaced by 250MHz, a change of 125MHz (or less if the mode is not originally at the transmission maximum) will cause the laser to switch modes. Any error in the response of any of the three galvanometers will cause the pre-set tracking to be spoilt. (A piece of grit need only cause a 0.4% deviation in a 30GHz scan for the laser to hop). The etalon also had to be set accurately to normal incidence before the tracking voltage was applied or the square root relation does not hold. If the etalon itself was at all dirty then as it scanned

the tracking mode need not necessarily have the most gain, and the laser would also try to hop. All of the above variables meant that effort was required daily to get the laser to scan without hopping. So far there has been no reported case of a dead reckoning scheme working particularly well with a Ti:sapphire laser.

Alternative Schemes

The alternative to a dead reckoning scheme is that of dither and lock. A standard dither and lock scheme uses an air spaced etalon with a piezo spacer. The piezo is dithered at a frequency of a few kHz over a few nm. This in turn dithers the transmission frequency of the etalon by several MHz and therefore slightly alters the intensity of the laser output. Using phase sensitive detection the output is heterodyned with the dither signal. The result is shown in figure 5.13.

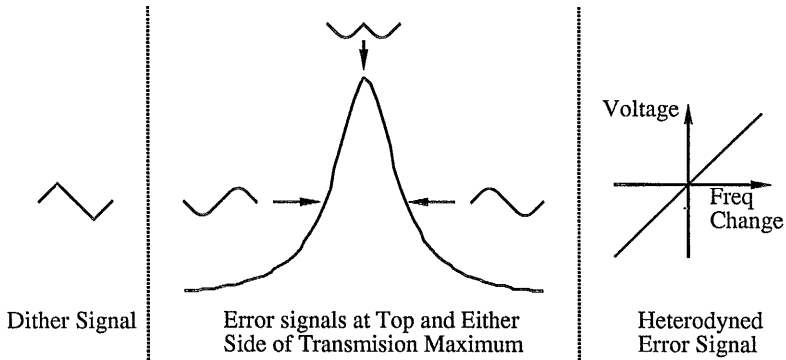


Figure 5.13 - Dither and lock to maximum of etalon transmission

If the etalon is at the transmission maximum the intensity change in the two half cycles is the same and the heterodyned signal is zero. If the transmission is off the maximum the output will be positive or negative depending on which way the signal has moved. In this way the feedback signal always keeps the etalon locked onto maximum transmission. This method has been used several times with Ti:sapphire lasers^{2,3} and until recently was the only reliable method of scanning the laser. Unfortunately air spaced etalons are very expensive.

We also investigated using a dither and lock method using the galvo mounted solid etalon. In theory this should work as well as dithering at higher frequencies using a piezo, but the galvo can only respond to frequencies of up to a few hundred Hz and unfortunately there is a lot of intensity noise in the Ti:sapphire laser at low frequencies due to the argon ion pump laser power fluctuations so that although these intensity perturbations are not large, they are large enough that the dithered signal is lost in the

background noise. Recently a new technique has been developed by Charles Adams et al⁴ which now forms an alternative to an air spaced etalon. Their method also uses a solid etalon but is one in which the dither of angle is controlled by a piezo. This is done by mounting the solid etalon directly onto a tube piezo which has been split in two lengthways. The voltage to each half is dithered in anti-phase to the other so that while one expands the other contracts. The etalon is firmly attached to both halves of the piezo which is itself rigidly mounted to an armature mounted on a galvo. The experimental arrangement tried is shown in figure 5.14.

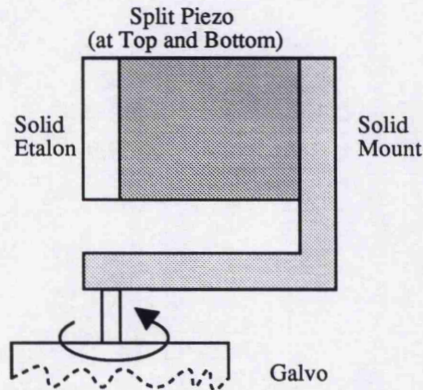


Figure 5.14 - Adams' method of Etalon Dithering

This method has the advantage that the etalon can be dithered at kHz levels while keeping the large tunability for the solid etalon of mounting the whole on a galvanometer. The error signal in this case is the small reflection of the intracavity power off the etalon surface. At maximum transmission this goes through a minimum and the error signal is similar to that shown in figure 5.13. Preliminary experiments⁵ using this method have already produced results better than those for the dead reckoning method but the system needs further development.

Conclusion

It seems clear that using a dead reckoning method of keeping the etalon transmission maximum following the laser mode will never be a reliable way of ensuring a scan without mode hops. Although this method has allowed 10GHz scans to be carried out, the time needed to adjust the laser for use justifies exploration into more reliable methods, in particular dither and lock schemes. These can either be in conjunction with an air-spaced etalon or using Adams' method as described above. At

present the latter seems a promising technique for scanning a laser without the power loss or expense of using an air-spaced etalon and is the basis for current work.

References

- 1 T L Boyd and H J Kimble - Frequency Stabilisation of a continuous-wave Ti:sapphire laser - Opt. Lett., Vol. 16, No. 11, pgs 808-810, 1991
- 2 X Zhan et al. - High-Resolution Photoacoustic Ti:Sapphire/Dye Ring Laser Spectrometer - Rev. Sci. Instrum, Vol.63, No.12, Dec 92
- 3 S Bourzeix et al. - Efficient Frequency Doubling of a Continuous Wave Ti:Sapphire Laser in an External Enhancement Cavity - Opt. Comm., Vol. 99, No. 1-2, pgs 89-94, 1993
- 4 C Adams - Ph.D Thesis, Strathclyde University, 1992
- 5 Conducted with Mr. R R Moseley (Ph. D Research Student)

Circuit Diagrams For Control Electronics

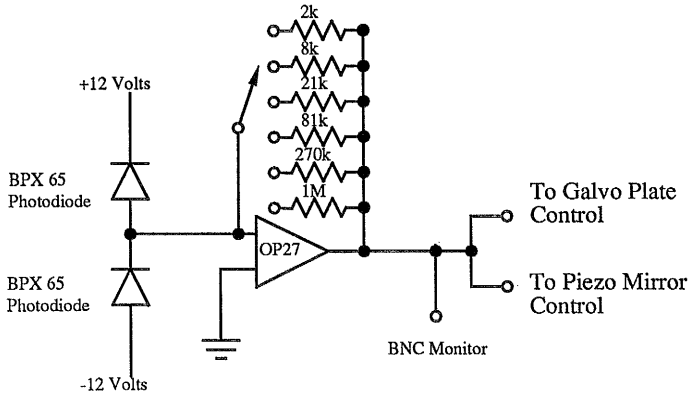


Figure 5.a - Photodiode Pre-Amp

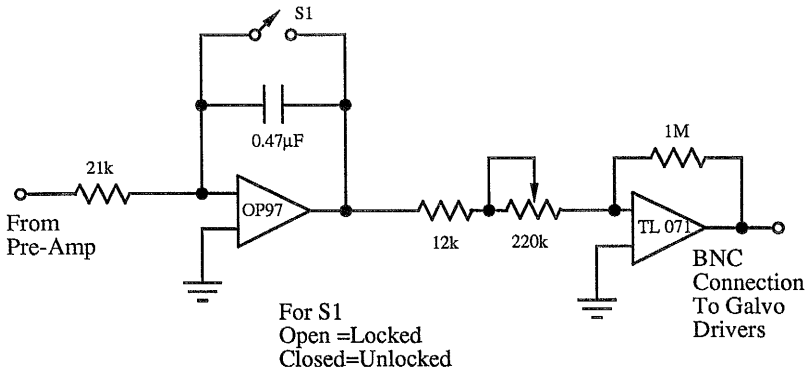


Figure 5.b - Galvo Plate Control

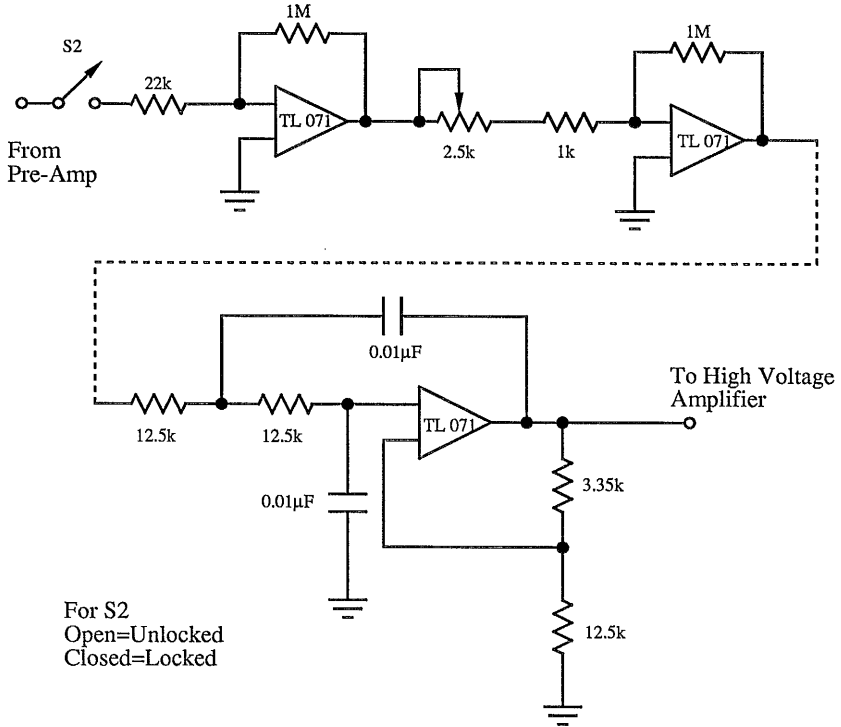


Figure 5.c - Piezo Mirror Control

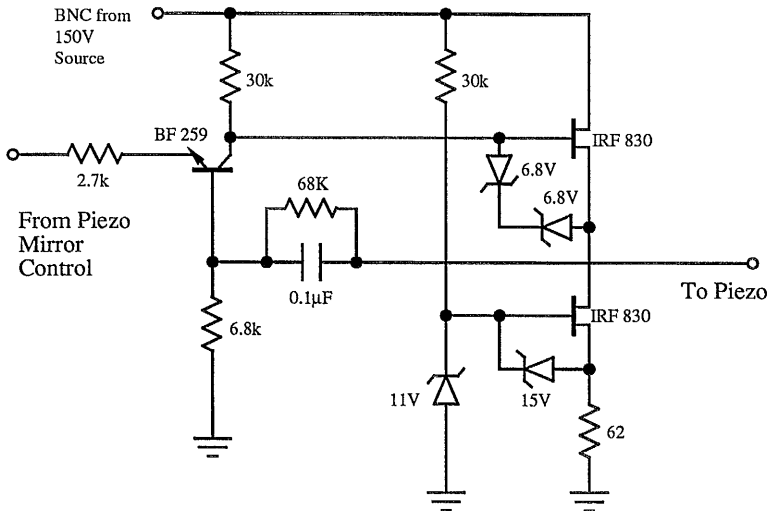


Figure 5.d - High Voltage Amplifier

Theory of Sum Frequency Generation in Vapours

The use of vapours in second harmonic generation (SHG), sum frequency generation (SFG) and difference frequency generation (DFG) has been studied by a number of researchers over the years¹⁻³. The main interest of such studies is often the generation of light in the ultraviolet part of the spectrum where the traditional use of nonlinear crystals for frequency conversion is hampered by the decreasing transparency of such crystals at low wavelengths. These experiments take advantage of the resonantly enhanced absorption of an atomic transition as the frequency of a laser source is tuned near the transition frequency. This can be explained with the aid of a three level energy diagram as shown in figure 6.1.

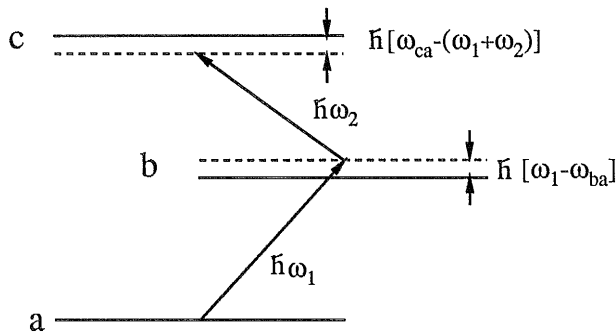


Figure 6.1-Three Level Atom showing Single and Two Photon Detuning from Resonance for a Three Wave Interaction

In the figure shown above the three energy levels, a, b and c, are separated by the energies $\hbar\omega_{ba}$, $\hbar\omega_{cb}$ and $\hbar(\omega_{ba} + \omega_{cb})$. For the experiments described here two different laser sources were used to provide coherent excitation between the atomic levels - a dye laser in the visible at frequency ω_1 and a Ti:sapphire laser in the infrared at frequency ω_2 . The two laser sources provide photons of energy $\hbar\omega_1$ and $\hbar\omega_2$ respectively. The strength of the induced transition from level c to a depends on how close the two lasers are tuned to both single photon, $\hbar(\omega_{ba} - \omega_1)$, and two photon resonance, $\hbar[\omega_{ac} - (\omega_1 + \omega_2)]$, as well as, for the scheme used here, to the strength of the magnetic field used to break the symmetry of the vapour. As the atomic system consists not just of one atom but an ensemble of atoms, the behaviour of the system as a whole can be explained as an

average. This average behaviour is expressed in terms of a density matrix, in which the components of the matrix represent the populations of the atomic levels, the transitions between the levels and the phase coherence between levels established by the coherent laser fields but lost through collisions within the vapour. This chapter looks in detail at the density matrices associated with the two sum-frequency transitions in order to predict the expected output. As a necessary prelude to the examination of the Density Matrices the energy levels a, b, and c must themselves be understood. The two sum frequency routes were 3S-3P-3D-3S and 3S-3P-4P-3S. Apart from the 3S level, each of the other levels actually consists of two sublevels split by spin orbit coupling. In addition, all of the levels are degenerate in the absence of a magnetic field, but as the sum-frequency interaction takes place with a magnetic field present, these levels are split by the Zeeman effect into a number of sub-levels. The behaviour of each of these levels in a magnetic field and the quantum numbers associated with each level are discussed later in the chapter. To conclude the chapter the bulk effects of phase matching in an atomic vapour are discussed in terms of vapour density, atomic resonances and the effect of focusing the Gaussian laser beams.

Three Wave Mixing in Vapours

To start with, how can one get a second order nonlinear interaction in a medium as homogeneous as an atomic vapour? This can be understood by referring back to figure 6.1. The transition from level a to b is characterised by the tensor matrix element $\langle b|M^{(x)}|a\rangle$, where $M^{(x)}$ is an operator which describes the type of transition from level a to level b. For example a dipole transition would be described as $D^{(1)}$, which indicates that the irreducible tensor associated with the transition is of order 1, and that there are three pseudo-vector components of this irreducible tensor. In physical terms the three components of the dipole tensor represent the three changes of orbital angular momentum which can occur during a dipole transition. (In the commonly used terminology for a dipole transition, $-e\langle b|D^{(1)}|a\rangle = -e\langle b|\hat{r}|a\rangle$, the term $D^{(1)}$ is used here to emphasise that dipole and quadrupole transitions are similar in nature but differ in selection rules). A quadrupole transition is described by $Q^{(2)}$, indicating that the irreducible tensor is of the second order⁴. There are five possible changes of orbital angular momentum in a quadrupole transition and so the tensor has five components. A full description of the transition would include which one of the tensor elements was being used, for example $Q_0^{(2)}$, $Q_{\pm 1}^{(2)}$ or $Q_{\pm 2}^{(2)}$. (The dipole tensor elements are $D_0^{(1)}$ and $D_{\pm 1}^{(1)}$.)

If the two photons of frequency ω_1 and ω_2 are absorbed by the atom such that an electron is shifted from level a to level c then the strength of the $\chi^{(2)}$ nonlinearity for the return transition from c to a is given by the expression⁵:

$$\chi^{(2)} \propto \frac{N}{2\hbar^2} \frac{\langle a|M^{(z)}|c\rangle\langle b|M^{(x)}|a\rangle\langle c|M^{(y)}|b\rangle}{(\omega_{ab} - \omega_1)(\omega_{ca} - (\omega_1 + \omega_2))} \quad \text{Eqn (6.1)}$$

Obviously the nonlinearity becomes stronger the larger are the matrix elements for the three transitions and the closer the lasers are tuned to both single and two photon resonance. The most common type of transition is a dipole transition but these transitions can only take place between states of opposite parity. For a closed cycle ($a \rightarrow b \rightarrow c \rightarrow a$) the three transitions cannot all be between states opposite in parity and so the $\chi^{(2)}$ nonlinearity will be zero. However if one of the transitions is of a higher order, such as a quadrupole, which is not parity forbidden, or alternatively some means is employed to mix states of opposite parity so that all the dipole elements are non-zero, then the nonlinearity can have a non-zero value. This means that the tensor matrix element of at least one of the transitions will be dependent on some external factor. (To cheat slightly by skipping ahead in this explanation, we have used a magnetic field to induce a quadrupole transition so for our transitions the $\chi^{(2)}$ nonlinearity is also magnetic field dependent)

Although these means might result in a non-zero $\chi^{(2)}$, collinear three wave mixing will still be forbidden by symmetry considerations of the momentum conservation law for the wavevectors of the three waves in the sum frequency interaction, $k_3=k_1+k_2$. As the medium is centrosymmetric there is no preferred direction in which momentum must be summed but instead a direction can be chosen arbitrarily. If one looks at the z component of the angular momentum of the three photons then they can each have a value of ± 1 . However, $\pm 1 \neq \pm 1 \pm 1$ in any combination and so a collinear three-wave interaction is not allowed. If the symmetry of the vapour is broken then a preferred direction is imposed on the vapour and the momentum conservation law can also be satisfied. These two factors, namely a symmetry breaking scheme and a multipole interaction or a parity mixing scheme are the basis on which three wave mixing in vapours is achieved.

There are four ways in which both conditions can be satisfied. These are all reviewed at length in references 1 and 2 and will only be summarised here.

1) Non-Collinear Beams⁶

If the beams are not collinear then the momentum laws can be satisfied without other means (fig 6.2), but the condition for $\chi^{(2)}$ must still be met.

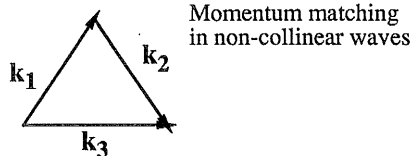


Figure 6.2 - Non-Collinear Phase-Matching

A non-collinear two dipole one quadrupole transition satisfies both conditions but is not ideal as the conversion efficiency will be weak on at least two counts. Firstly, quadrupole transitions in general have lower transition strengths than do dipole interactions. The ratio of electric dipole to electric quadrupole strengths is^{4,7} $1:Z^2\alpha^2$ where Z = atomic number and $\alpha \approx 1/137$. For sodium this means that the quadrupole transitions strengths are about 3% of that of dipoles. A second factor is that because the beams are not collinear the interaction length is severely limited. As the power generated is proportional to the square of the length this greatly reduces the efficiency.

2) Transverse Electric Field⁸

If a transverse electric field is imposed upon the vapour then the eigenfunction of the atom becomes perturbed and states of opposite parity become mixed. This allows a non-zero value for the $\chi^{(2)}$ nonlinearity. It also imposes a preferred quantisation direction on the vapour in which the conservation of momentum can be satisfied.

3) Use of High Energy Pulses⁹

The mechanism for frequency mixing using high energy pulses is not known, but it is possible that it is similar to that when an external electric field is applied in that the pulses create a local electric field which mixes states of opposite parity.

4) Magnetic Field Scheme³

The application of an external magnetic field does not mix states of opposite parity, so that a quadrupole transition must be used in a three wave interaction. In the absence of a magnetic field the quadrupole does not radiate in the forward direction, but the magnetic field mixes Zeeman sublevels of the atom causing the quadrupole moments previously radiating transversely to the beam to rotate, allowing a component to exist in the forward direction so that a coherent sum-frequency interaction can take place along the length of the oven.

All of these schemes have been described in detail previously and only the one used in this work, that of magnetic field induced SFM will be treated here.

The Energy levels of Sodium and Their Behaviour in a Magnetic Field

The atomic vapour used in this work consists of sodium atoms in which there are two closed shells containing 10 electrons, and a single optically active valence electron in the outermost ($n=3$) shell. In its ground state the electron occupies the 3S shell. The SFG we have looked at utilises two routes between energy levels, one of which is $3S \rightarrow 3P \rightarrow 3D \rightarrow 3S$ and the other $3S \rightarrow 3P \rightarrow 4P \rightarrow 3S$. The first route employs two dipoles on the upward transition, with a quadrupole emission, and the second has both a dipole

and a quadrupole on the upward route with a dipole emission. These will be called the DDQ and the DQD routes respectively. The four energy levels in zero magnetic field and the wavelengths corresponding to transitions between the upper three and the ground state are shown in figure 6.3. This figure includes the splitting due to spin-orbit (fine) coupling but not the far smaller hyperfine splitting.

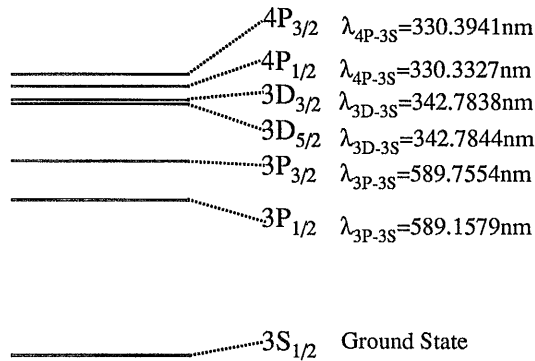
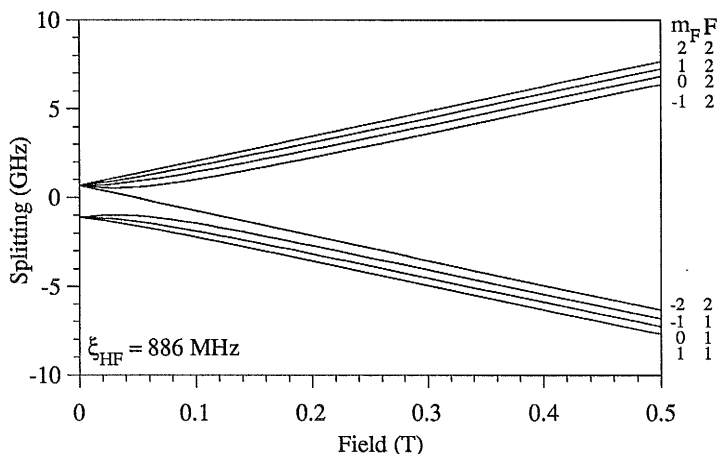
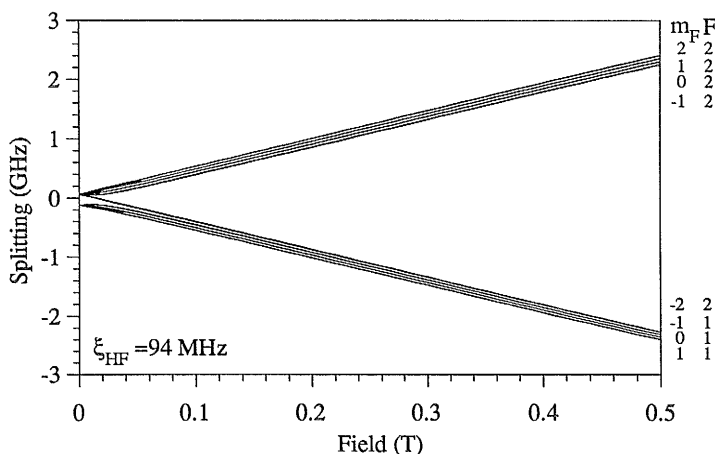


Figure 6.3 - Relevant Energy Levels in Sodium

The terms S, P, and D represent the orbital angular momentum value (L) of each state, and are 0, 1 and 2 respectively. The spin-orbit coupling splits each level into two angular momentum components, $L-S$ and $L+S$, where S is the spin angular momentum. The exception is the S level in which there is no spin-orbit coupling as $L=0$. The total angular momentum value is called J , and as sodium has only one valence electron the calculation of S , L , and J is straightforward. ($S = \Sigma s = 1/2$ or $-1/2$, $L = \Sigma \ell = 0, 1, \text{ or } 2$, $J = L \pm S$). Each of the J levels are further split into hyperfine components by the interaction of the nuclear magnetic moment with the magnetic field produced at the nucleus by the orbiting electrons. These hyperfine components are characterised by the quantum number F , where F can have the values $I+J, I+J-1, \dots, |J - I|$, where I is the nuclear angular momentum quantum number. For sodium, $I=3/2$. The hyperfine splitting is greatest in the 3S levels as their wavefunctions overlap those of the nucleus to a greater extent than do those of the other levels. All of the energy splittings, from the energy differences between levels to the fine and hyperfine splittings decrease the further they are from the influence of the nucleus.

With the application of a magnetic field (B) the states are split into each of their previously degenerate components by the Zeeman effect. The J states each have $(2J+1)$ levels from $m_J = J$ to $m_J = -J$ and similarly the hyperfine levels are labelled by $m_F = F$ to $m_F = -F$. The effect of the field can be characterised into three regions- a weak field region, an intermediate field region and a strong field (or Paschen Back) region. For the

$3S_{1/2}$ level the weak field region is the one in which the splitting of the hyperfine components ($\propto \mu_B B$) is much less than the zero field splitting of the F components (twice ξ_{HF} , the hyperfine constant). The Paschen-Back region is where the opposite is true. In the first case the Zeeman effect is perceived as a small perturbation on the hyperfine interaction and in the strong field the hyperfine is a small perturbation on the Zeeman effect. If one looks at the Zeeman splitting of the $3S_{1/2}$ level (fig 6.4) and compares it to the $3P_{1/2}$ level (fig6.5) then it is obvious how much more important the hyperfine interaction is in the former case, as the Paschen-Back region is not reached until $\sim 0.2T$ as opposed to $\sim 0.05T$ in the $3P_{1/2}$ state. (The formulae with which the splittings are calculated are shown later in this chapter).


 Figure 6.4 - Zeeman Splitting of $3S_{1/2}$ Hyperfine Levels

 Figure 6.5 - Zeeman Splitting of $3P_{1/2}$ Hyperfine Levels

For the higher energy states the hyperfine interaction has become small enough¹⁰ to be ignored for the purposes here and the Zeeman splitting of the hyperfine states is in the Paschen-Back (P-B) region for all fields above 0.05T, but at the same time the magnitude of the spin-orbit coupling has also decreased. For the 3P states the spin-orbit coupling (this is $(\ell+1/2)$ times the fine constant, ξ_F) is very large as compared to the field splittings and so they are always in the weak field region for the Zeeman splitting of the fine components. Although the coupling is a factor of 3 less in the 4P states they are also always in the weak field region (fig 6.6). The 3D states however have a value of ξ_F that is less than one hundredth that of the 4P levels and so the Zeeman splitting of the fine states takes them beyond the weak field region to the intermediate/strong field region as the field is increased to 0.5T (fig 6.7). The behaviour of the fine and hyperfine components of the sodium atom were calculated using a mathematical solution to the perturbation of the atom's Hamiltonian by a magnetic field. The relations used are shown later in this section, but the importance of calculating the behaviour of each level is that each is composed of a mixture of eigenstates and that this mixture varies depending on whether the atom is in a strong, intermediate or weak field region with regard to both the fine and hyperfine splitting. Once the eigenstate composition of each level is known in a particular magnetic field then the selection rules governing both dipole and quadrupole transitions can be applied. This allows one to know exactly which transitions between levels are allowed for that field strength. The selection rules for dipole and quadrupole transitions are tabulated in the section following this one on eigenstate variation in magnetic fields.

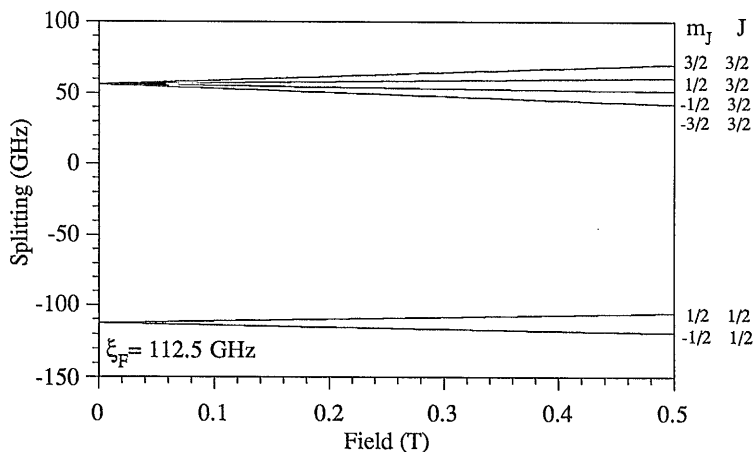


Figure 6.6 - Zeeman splitting of 4P fine levels

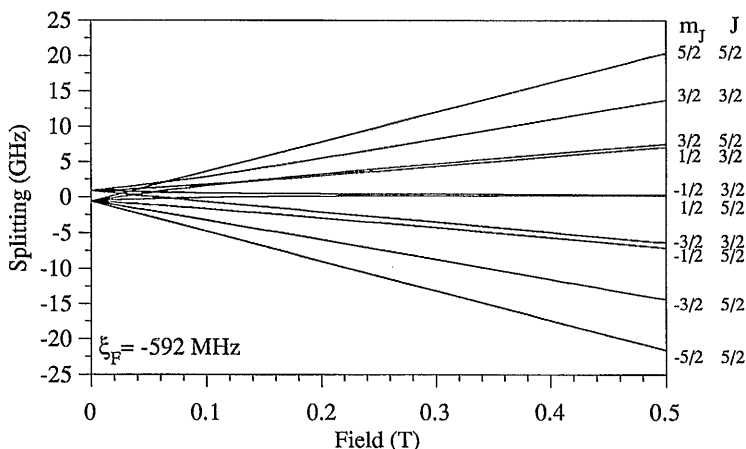


Figure 6.7 - Zeeman Splitting of 3D fine levels

As the magnetic field strength is increased and the levels pass through weak, intermediate or strong field regions field region, it is not appropriate to use either m_F or m_J as the basis on which transitions between levels are traced, as the eigenstate mixture within these levels is not constant. Instead the more fundamental quantum numbers m_ℓ and m_s are used. The quantum number m_ℓ can have values from ℓ (orbital angular momentum) to $-\ell$. The value of m_s can be either $1/2$ (spin up) or $-1/2$ (spin down). During a transition from one level to another the electron cannot change its spin value⁴ and so only transitions to levels with the same spin value are allowed. This gives the selection rule $\Delta m_s = 0$. The change in the value of m_ℓ is linked to the type of transition (a list of selection rules is given in table 6.1). Each of the fine and hyperfine levels are a mixture of spin $1/2$ and spin $-1/2$ eigenstates. The m_J and m_F numbers are composed as follows:

$$m_J = m_\ell + m_s$$

$$m_F = m_I + m_J$$

(In comparing the behaviour of fine and hyperfine levels the numbers F and J are analogous, and in the same way I behaves like ℓ and J behaves like s).

For the $3S_{1/2}$ state there is no spin-orbit coupling but the hyperfine interaction is strong and so the behaviour of the hyperfine levels in a magnetic field is of importance. As $m_\ell = 0$, so $m_J = m_s = \pm 1/2$. Any m_F (hyperfine) state is therefore composed of the two spin eigenstates such that :

$$\begin{aligned}\Psi(n, \ell, m_F) &= C_1 \phi |m_I, m_s\rangle + C_2 \phi |m_I', m_s'\rangle \\ &= C_1 \phi |m_F - \frac{1}{2}, \frac{1}{2}\rangle + C_2 \phi |m_F + \frac{1}{2}, -\frac{1}{2}\rangle\end{aligned}\quad \text{Eqn. (6.2)}$$

The two coefficients C_1 and C_2 are the Clebsch-Gordon coefficients of the eigenstates. In order to normalise the wave function one sets $\Psi\Psi^* = 1$, which results in the relation $(C_1)^2 + (C_2)^2 = 1$. $(C_1)^2$ and $(C_2)^2$ are the probabilities of the electron being in each of the spin states, $m_s = 1/2$ or $m_s = -1/2$, respectively. These coefficients vary with a magnetic field, one increasing while the other decreases, and in the Paschen-Back region each m_F level is composed either of the spin $1/2$ eigenstate or the spin $-1/2$ eigenstate.

For the states with spin-orbit coupling each m_J (fine) level is also composed of spin $1/2$ and spin $-1/2$ eigenstates. The comparable equation to that given for the hyperfine states, but this time looking at the m_J levels instead of the m_F levels is:

$$\begin{aligned}\Psi(n, \ell, m_J) &= C_1 \phi |m_\ell, m_s\rangle + C_2 \phi |m_\ell', m_s'\rangle \\ &= C_1 \phi |m_J - \frac{1}{2}, \frac{1}{2}\rangle + C_2 \phi |m_J + \frac{1}{2}, -\frac{1}{2}\rangle\end{aligned}\quad \text{Eqn. (6.3)}$$

The intensity of a transition between one state and another is proportional to the square of both the upper and lower state Clebsch-Gordon coefficients so that in an emission spectrum some lines will grow in intensity while others disappear as the magnetic field increases and the eigenstate mixture varies.

The splitting of the states by the Zeeman effect is given by the solution of the two time-invariant equations^{4,7,11}:

$$\begin{aligned}C_1 \Delta E &= C_1 \mathcal{H}'_{11} + C_2 \mathcal{H}'_{12} \\ C_2 \Delta E &= C_1 \mathcal{H}'_{21} + C_2 \mathcal{H}'_{22}\end{aligned}\quad \text{Eqn. (6.4)}$$

where \mathcal{H}' is the perturbation of the Hamiltonian caused by the magnetic field. This leads to a secular equation of the form:

$$\begin{vmatrix} \mathcal{H}'_{11} - \Delta E & \mathcal{H}'_{12} \\ \mathcal{H}'_{21} & \mathcal{H}'_{22} - \Delta E \end{vmatrix} = 0\quad \text{Eqn. (6.5)}$$

The solution of this equation leads to a general equation for the Zeeman splitting of the fine states¹²:

$$\Delta E = m_J \mu_B B - \frac{\xi_F}{4} \pm \frac{\xi_F}{4} \sqrt{X}\quad \text{Eqn. (6.6)}$$

where ξ_F is the fine structure constant (spin perturbation), B is the field strength in Tesla and μ_B is the Bohr magneton. The upper term is for the $J=L+S$ state and the lower term for $J=L-S$. The value under the square root is given by:

$$x = 1 + 8m_J \left(\frac{\mu_B B}{\xi_F} \right) + 4 \left(\frac{\mu_B B}{\xi_F} \right)^2 + 4\ell(\ell + 1)$$

where ℓ = the orbital angular momentum of the state. The total zero field splitting between the L+S and the L-S states is:

$$\Delta E = \frac{\xi_F}{2} (2\ell + 1) \quad \text{Eqn. (6.7)}$$

The solution of the secular equation combined with eqn. 6.4 and the normalisation of the wave function allows the variation of the Clebsch-Gordon coefficients with magnetic field to be found:

$$(C_1)^2 = \frac{Y^2}{Y^2 + Z^2} \quad (C_2)^2 = \frac{Z^2}{Y^2 + Z^2} \quad \text{Eqn. (6.8)}$$

where:

$$Z = \frac{\xi_F}{2} \sqrt{(1 + m_J + \frac{1}{2})(1 - m_J + \frac{1}{2})}$$

and

$$Y = \frac{\xi_F}{2} \left[m_J + \left(\frac{\mu_B B}{\xi_F} \right) \pm \frac{1}{2} \sqrt{x} \right] \quad \begin{array}{l} + \text{ for } J = L + S \\ - \text{ for } J = L - S \end{array}$$

The Breit Rabi formula for the splitting of the $J=1/2$ hyperfine states¹³ is of a similar form and can be shown to be the same when calculating C_1 , C_2 , and x , given the following substitutions :

$$\begin{aligned} m_J &\rightarrow m_F, \ell \rightarrow I, \mu_B \rightarrow (g_J - g_I) \mu_B, \xi_F \rightarrow \xi_{HF} \\ g_J &= \text{Lande } g \text{ factor, } g_I = \text{nuclear } g \text{ factor} \end{aligned}$$

With these substitutions the behaviour of the hyperfine eigenstates can be found using Eqn. 6.8 given that:

$$\begin{aligned} Z_{\text{Breit Rabi}} &= \frac{\xi_{HF}}{2} \sqrt{(1 + m_F + \frac{1}{2})(1 - m_F + \frac{1}{2})} \\ Y_{\text{Breit Rabi}} &= \frac{\xi_{HF}}{2} \left[m_F + \left(\frac{(g_J - g_I) \mu_B B}{\xi_F} \right) \pm \frac{1}{2} \sqrt{x_{HF}} \right] \quad \begin{array}{l} + \text{ for } F = I + S \\ - \text{ for } F = I - S \end{array} \end{aligned}$$

$$x_{\text{BreitRabi}} = 1 + 8m_F \left(\frac{(g_J - g_I)\mu_B B}{\xi_{\text{HF}}} \right) + 4 \left(\frac{(g_J - g_I)\mu_B B}{\xi_{\text{HF}}} \right)^2 + 4I(I+1)$$

The energy splitting term in the hyperfine states is slightly different to that for the fine states and is given by :

$$\Delta E_{\text{BreitRabi}} = -g_I m_F \mu_B B - \frac{\xi_{\text{HF}}}{4} \pm \frac{\xi_{\text{HF}}}{4} \sqrt{x_{\text{BreitRabi}}}$$

(for sodium $g_I = -0.0008$, for the $3S_{1/2}$ state $g_J = 2.002$)

The equations for the splitting of the energy levels and the variation of their eigenstate coefficients for the fine and hyperfine interactions have been written in the forms given above to emphasise the similarity between the behaviour of the fine and hyperfine interactions in a magnetic field.

The variation of the eigenstates of the levels $3S(F, m_F)$, $3D(J, m_J)$, and $4P(J, m_J)$ are given in figures 6.8-6.10. (The coefficients C_1 and C_2 are called S_a and S_b for the S levels, P_a and P_b for the P levels, etc.). Although the eigenstate coefficients vary considerably for the S and D states, the 4P state coefficients are virtually invariant for these field values. The 3P values change even less than the 4P values and can be read from the same graph.

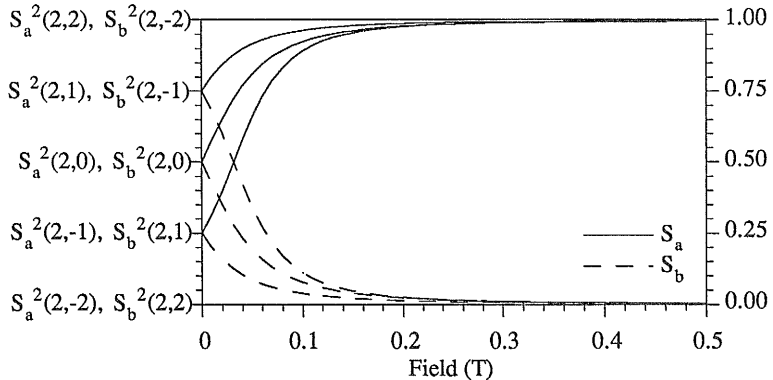


Figure 6.8a - Variation of Eigenstate Components of $3S(F, m_F)$ levels with magnetic field, for the $F=2$ levels

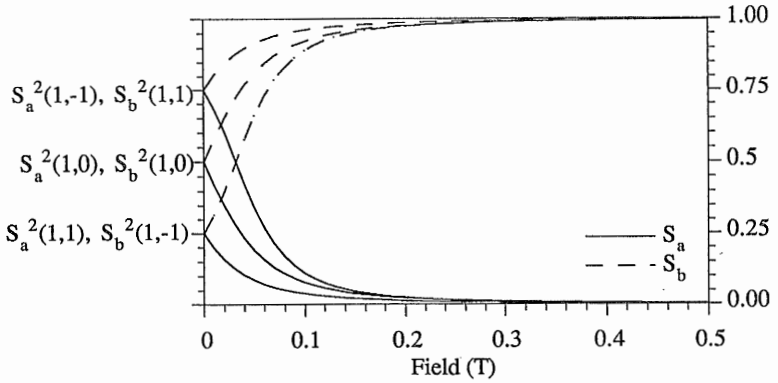


Figure 6.8b - Variation of Eigenstate Components of 3S (F, m_f) levels with magnetic field, for the F=1 levels

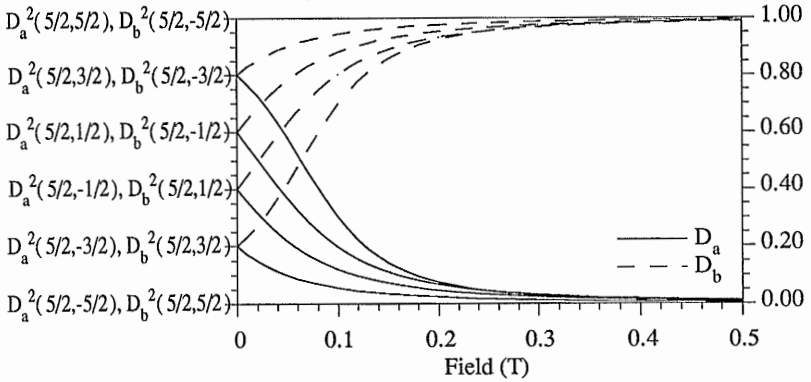


Figure 6.9a - Variation of Eigenstate Components of the 3D (J, m_j) levels with magnetic field, for the J=5/2 levels

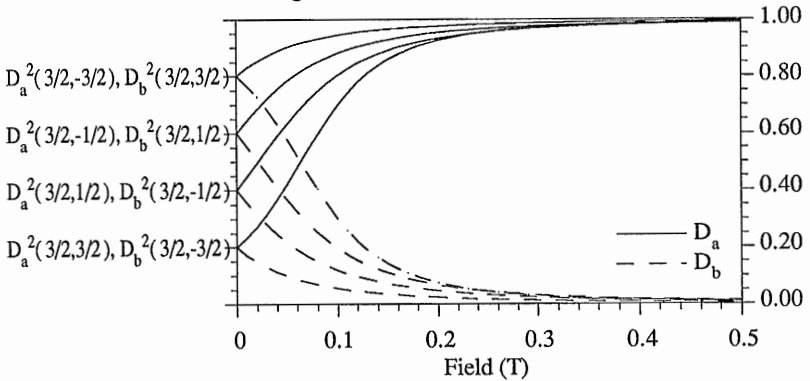


Figure 6.9b - Variation of Eigenstate Components of the 3D (J, m_j) levels with magnetic field, for the J=3/2 levels

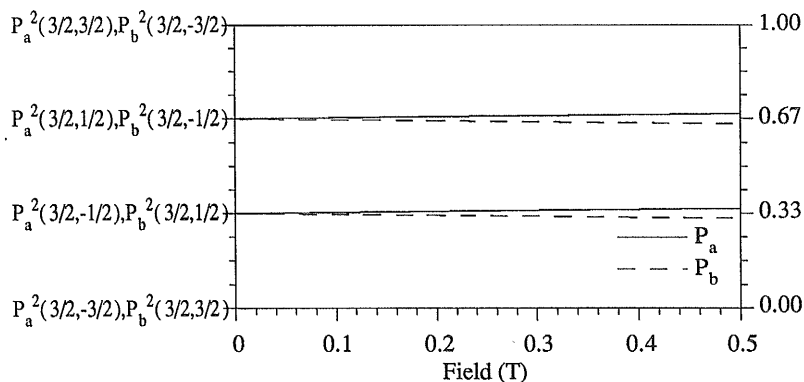


Figure 6.10a - Variation of Eigenstate Components of the $4P (J, m)$ levels with magnetic field, for the $J = 3/2$ levels

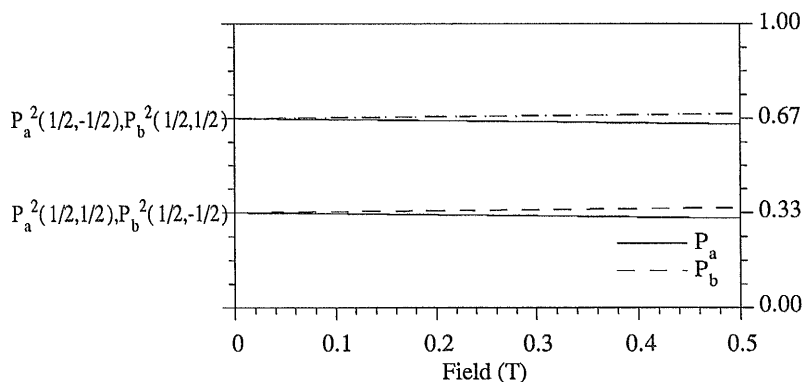


Figure 6.10b - Variation of Eigenstate Components of the $4P (J, m)$ levels with magnetic field, for the $J = 1/2$ levels

Selection Rules

The selection rules for dipole and quadrupole transitions¹⁴ are given in Table 6.1. These rules govern the allowable transitions between the eigenstates for the 3S-3P, 3P-3D and 4P-3S dipole transitions used in these experiments and also for the two quadrupole transitions, 3D-3S and 3P-4P.

Electric Dipole	Electric Quadrupole
$\Delta J = 0$ (except $0 \leftrightarrow 0$) $\Delta m_\ell = 0, \pm 1$ (except $0 \leftrightarrow 0$ when $\Delta J = 0$) Parity change One electron jumping with $\Delta \ell = \pm 1$	$\Delta J = 0, \pm 1, \pm 2$ (except $0 \leftrightarrow 0, 1/2 \leftrightarrow 1/2, 0 \leftrightarrow 1$) $\Delta m_\ell = 0, \pm 1, \pm 2$
Δn arbitrary $\Delta S = 0$ $\Delta L = 0, \pm 1$ (except $0 \leftrightarrow 0$)	No Parity change No change in electron config; or one electron jumping with $\Delta \ell = 0, \pm 2$ Δn arbitrary $\Delta S = 0$ $\Delta L = 0, \pm 1, \pm 2$ (except $0 \leftrightarrow 0, 0 \leftrightarrow 1$)

Table 6.1 - Selection rules for Atomic Transitions

For the two different routes (DDQ and DQD) these rules restrict which of the Zeeman components are present in the SFM output. Additional selection rules occur when using polarised laser beams and a magnetic field. In the scheme used in this work the lasers are linearly polarised, the direction of propagation of the light is perpendicular to the field, and the polarisation can be either parallel to the field or perpendicular to both the field and the direction of propagation. For these two polarisations the following selection rules occur for the upward routes:

Polarisation	Dipole	Quadrupole
Parallel (π)	0	± 1
Perpendicular (σ)	± 1	± 2

 Table 6.2 - Selection Rules for Δm_ℓ for Different Polarisations
of Light with respect to Magnetic Field Direction

Sub-components of Emission

The application of the selection rules to the upward transition in the 3S-3P-3D route for σ polarisation allows the change in Δm_ℓ from 3S to 3D to be either 0 or ± 2 . Therefore only the 3D levels in which $m_\ell = 0$ or ± 2 become populated. The quadrupole emission in the forward direction is only produced by the $\Delta m_\ell = \pm 2$ transitions while the $\Delta m_\ell = 0$ transition radiates to the sides and is not phase matched with the input waves. The upward routes possible for the population of the 3D sublevels responsible for the quadrupole radiation in the forward direction are shown in fig 6.11a. The figure shows the $|m_\ell, m_s\rangle$ eigenstates of each of the degenerate sublevels, with the eigenstates involved in the transition shown in bold type. There are six populated levels in the 3D

states, from each of which an electron can travel to one of seven lower levels. The strength of these transitions is proportional to the square of both upper and lower state Clebsch-Gordon coefficients and figures 6.7 and 6.8 show that for fields above 0.3T each of these coefficients is close to either 0 or 1 so that there are in effect only four populated upper state levels, each of which can decay to four lower levels in the Paschen Back region. These high field dominant states are surrounded by a dark square on the diagram. For each of the populated states in the 3D levels there can be either one or two routes via the 3P levels. The sum of the squares of the C-G coefficients of the intermediate levels is zero, which means that if the single photon detuning is large compared to the difference between intermediate levels then each of the upper states is equally likely to be populated. The strength of the return lines is therefore independent of the intermediate levels provided the input frequencies are far away from single photon resonance.

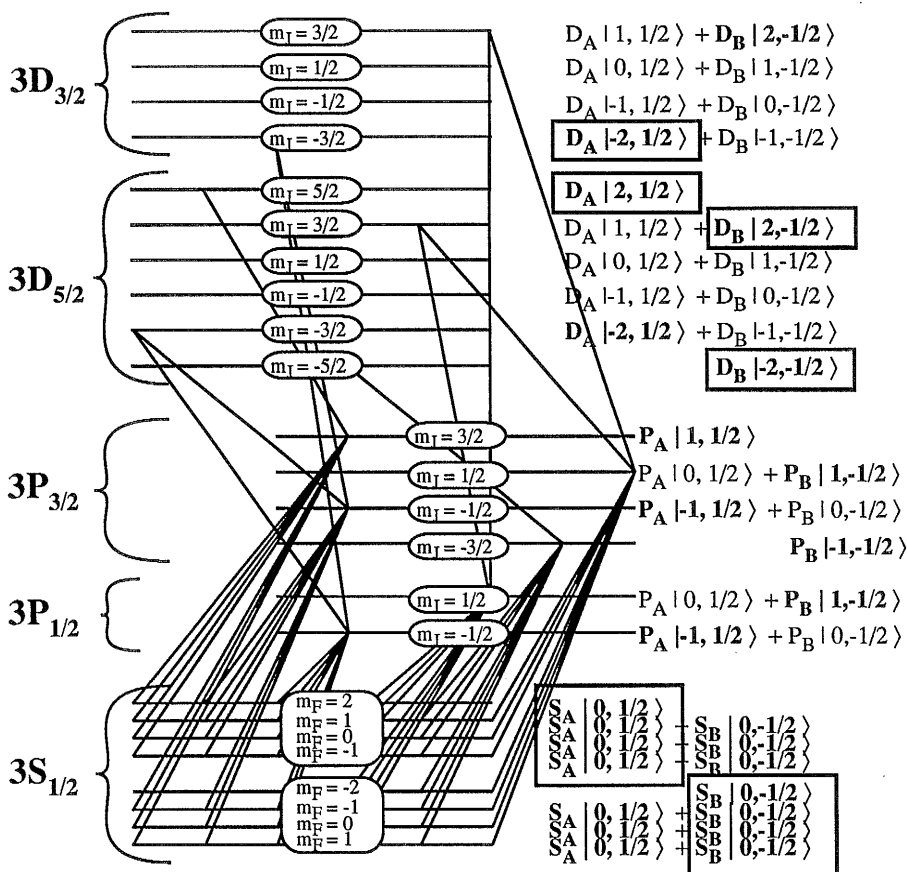


Figure 6.11a - Schematic Representation of all possible transitions between levels allowed by selection rules for the DDQ sum-frequency route using s polarisation. The bold type indicates the states which can take part in the transitions. If the levels collapse to one or the other of the spin eigenstates for the maximum field used in this work (0.5T) then the transitions are further limited. Where this happens then the eigenstates between which transitions are allowed for high magnetic fields are boxed.

The corresponding transition diagram for the DQD route is shown in figure 6.11b. In this case the second upward transition, 3P-4P, is a quadrupole transition while the return route is a dipole transition. Note that the selection rule for $J_{1/2} \leftrightarrow J_{1/2}$ comes into effect in that transitions between $3P_{1/2}$ and $4P_{1/2}$ are not allowed.

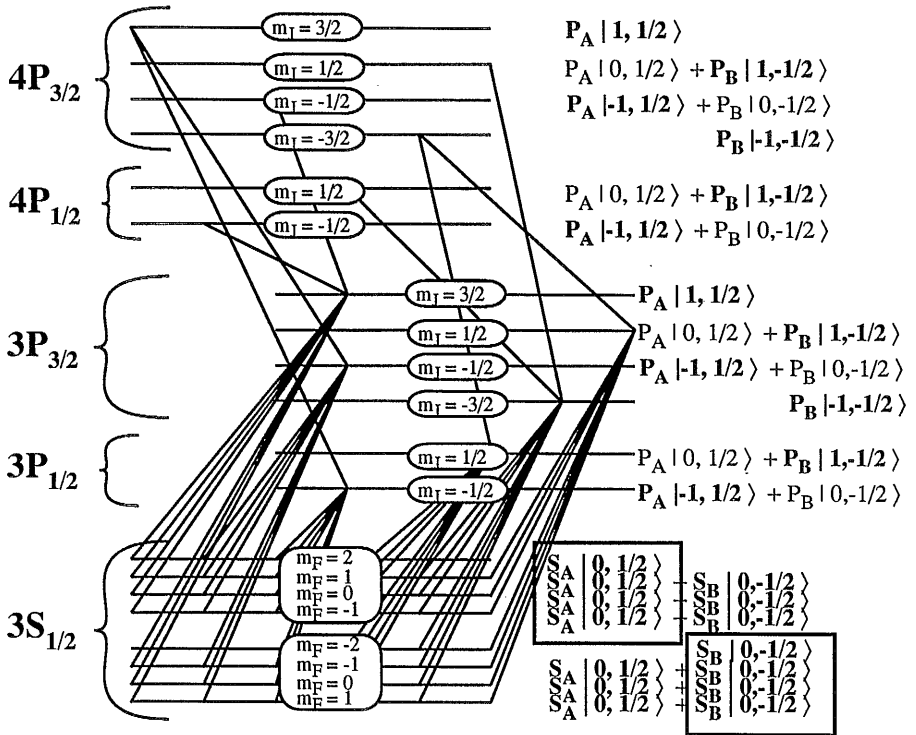


Figure 6.11b - Schematic Representation of all possible transitions between levels allowed by selection rules for the DQD sum-frequency route using s polarisation. The bold type indicates the states which can take part in the transitions. If the levels collapse to one or the other of the spin eigenstates for the maximum field used in this work (0.5T) then the eigenstates between which transitions are allowed for high magnetic fields are boxed. (Note that the Paschen-Back region is only reached by the 3S_{1/2} states, unlike in the previous route)

Derivation of Output Power at Sum Frequency

The previous sections have dealt with the behaviour of the energy levels and the possible transitions which may occur between them. A real atomic system such as that of sodium vapour is further complicated by the effects of Doppler broadening and spontaneous decay from the levels. It is impossible to know with any accuracy what is happening to a particular atom in the system, but it is possible to predict the average behaviour of a number of atoms¹⁵. This average behaviour is expressed in the form of a density matrix, where the off-diagonal elements of the matrix are the ensemble average of the expectation values of the interactions between states. If the wave function associated with a state is given by :

$$\Psi_a(\mathbf{r}, t) = \sum c_a(t) u_a(\mathbf{r}), \quad \text{Eqn. (6.9)}$$

where $u_a(\mathbf{r})$ are the eigenfunctions of the state, then an element of the ensemble average is defined by $\rho_{ab} = \overline{c_a^* c_b}$. For our system there are three main states (though each has a number of sub-levels as described previously) and so the density matrix is:

$$\rho_{ij} = \begin{bmatrix} \rho_{aa} & \rho_{ab} & \rho_{ac} \\ \rho_{ba} & \rho_{bb} & \rho_{bc} \\ \rho_{ca} & \rho_{cb} & \rho_{cc} \end{bmatrix} \quad \text{Eqn. (6.10)}$$

The elements ρ_{aa} , ρ_{bb} , and ρ_{cc} represent the populations of the three states and the off diagonal elements the transitions and coherences between the states. The off diagonal elements are related such that $\rho_{ab} = \rho_{ba}^*$. It is useful to treat the density matrix as a closed system in which the population is confined to the three levels, with no transitions to or from other levels, i.e. $\rho_{aa} + \rho_{bb} + \rho_{cc} = 1$.

If the system is subjected to a perturbation (such as a weak electromagnetic field) then one can describe the density matrix elements at some future time using a perturbation series:

$$\rho_{ij}(t) = \rho_{ij}^{(0)}(t) + \rho_{ij}^{(1)}(t) + \rho_{ij}^{(2)}(t) + \dots \quad \text{Eqn. (6.11)}$$

where $\rho_{ij}^{(0)}(t)$ is the unperturbed element, $\rho_{ij}^{(1)}(t)$ is the first order perturbation, $\rho_{ij}^{(2)}(t)$ the second order perturbation, etc.

The wave function of a perturbed system is found by solving Schrödinger's equation:

$$\mathcal{H}\Psi = i\hbar \frac{\partial \Psi}{\partial t}$$

As the density matrix resembles an ensemble average rather than a well defined wave equation, the application of Schrödinger's equation to the density matrix gives the Liouville Equation⁴:

$$\hbar \frac{\partial}{\partial t} \rho_{ij}(t) = -i \sum_k \mathcal{H}_{ik}(t) \rho_{kj}(t) + i \sum_k \rho_{ik}(t) \mathcal{H}_{kj}(t) \quad \text{Eqn. (6.12a)}$$

This is usually expressed as:

$$\frac{\partial}{\partial t} \rho_{ij} = -\frac{i}{\hbar} [\mathcal{H}, \rho]_{ij} \quad \text{Eqn. (6.12b)}$$

This equation is not quite a complete description of a real atomic system. Over a period of time the populations in each level will relax to the ground state via spontaneous emission as well as collision processes. The collisions within the system have the added effect of losing phase coherence between the levels. The overall effect of this is described by a loss term, Γ_{ij} , which when $i=j$ refers to the relaxation (population loss) from a level and when $i \neq j$ refers to the loss of phase information about a transition. Equation 6.12b can therefore be modified to:

$$\frac{\partial}{\partial t} \rho_{ij} = -\frac{i}{\hbar} [\mathcal{H}, \rho]_{ij} - \Gamma_{ij} (\rho - \bar{\rho})_{ij} \quad \text{Eqn. (6.13a)}$$

where $\bar{\rho}$ is the thermal equilibrium value of the density matrix as given by¹⁵:

$$\bar{\rho}_{ij} = \frac{\exp(-\mathcal{H}_0 / k_B T)}{\text{tr}[\exp(-\mathcal{H}_0 / k_B T)]}$$

$$\text{n.b. tr} = \text{trace, and } \text{tr}(ab) = \sum_i (ab)_{ii}$$

The perturbed Hamiltonian is such that $\mathcal{H} = \mathcal{H}_0 + \mathcal{H}'$, where \mathcal{H}' is the perturbation caused by the input waves. The unperturbed Hamiltonian can be described by $(\mathcal{H}_0)_{ij} = E_{ij} \delta_{ij}$. (For the three level atom shown in figure 6.1 the values of \mathcal{H}_0 are E_a , E_b and E_c). Using the relation $\omega_{ij} = (E_i - E_j)/\hbar$, equation (9.13a) can therefore be expressed in the form:

$$\frac{\partial}{\partial t} \rho_{ij} = -i\omega_{ij} \rho_{ij} - \frac{i}{\hbar} [\mathcal{H}', \rho]_{ij} - \Gamma_{ij} (\rho - \bar{\rho})_{ij} \quad \text{Eqn. (6.13b)}$$

This allows one to find a solution to the perturbation of the Hamiltonian in terms of an expansion as given in eqn 6.11. The terms in the expansion are given by the expression¹⁵:

$$\rho_{ij}^{(n)} = \frac{-i}{\hbar} \int_{-\infty}^t \exp(i(\omega_{ij} - i\Gamma_{ij})(t-t')) \left[\mathcal{H}'(t'), \rho^{(n-1)}(t') \right]_{ij} dt' \quad \text{Eqn. (6.14)}$$

Certain assumptions are necessary in order to simplify the solution of the expansion. The thermal equilibrium populations of all states above the ground state are assumed to be zero and the phase coherence between the states in the absence of the perturbing fields is also assumed to be zero. These assumptions are reasonable given that once the fields are turned off the atoms decay back to the ground state and

collisions between atoms destroy the phase information built up by the exciting fields. (This can be stated as $\rho_{aa}^{(0)} = 1$ and all other $\rho_{ij}^{(0)} = 0$).

The two types of interaction which take place in this work are dipole and quadrupole transitions. The geometry of the system for experiments is shown in figure 6.12. The experiments only use σ polarised light and so only the selection rules used in σ transitions are considered.

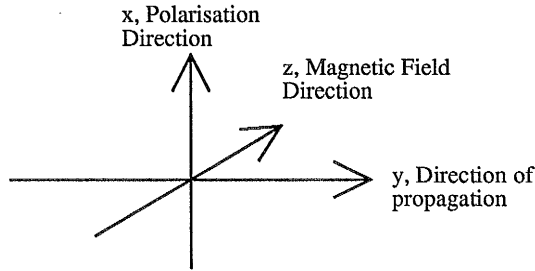


Figure 6.12- Designation of axes in Experiment.
Only σ polarisations are used

The perturbed element of the Hamiltonian \mathcal{H}' is $-\mathbf{d} \cdot \mathbf{E}$ for a dipole interaction, where $\mathbf{d} = e\mathbf{r}^{\hat{A}}$ and $\mathbf{E} = E\hat{\mathbf{e}}\cos(\omega t)^4$. (The ensemble average of the dipole moment induced by the field is represented in the Liouville Equation). The dipole moment is therefore given as $-d_x E \frac{1}{2}(e^{i\omega t} + e^{-i\omega t})$. This equation can be separated into two components, one of which contains the induced strength and phase of the transition, $-eE\cos(\omega t)$, and the other of which embodies the rules associated with the transition, $\langle b | D^{(1)} | a \rangle$ (as described previously). The phase component plays an immediate role in the following calculations, but the induced strength and the dipole matrix element will be treated later and are called V_{ij} now for convenience. This approach allows the derivation to be generic for both dipole and quadrupole induced transitions. For a quadrupole stimulated interaction the corresponding perturbation is $-\frac{1}{6}Q^{(2)} : \nabla \mathbf{E} = \frac{1}{6}Q_{yx}^{(2)} k E \frac{1}{2i}(e^{i\omega t} - e^{-i\omega t})$, which once again can be divided into two components, an $(e^{i\omega t} + e^{-i\omega t})$ term and a term dependent on the strength and transition type, V_{ij} .

The DDQ(3S-3P-3D) Route for Sum Frequency Mixing

For the sum frequency radiation generated via the 3S-3P-3D route the levels a, b, and c shown in figure 6.11 are the s, p, and d levels. The ground state is the s level. (It is split into 8 sublevels when the magnetic field is applied, but the splitting of these is much less than $k_B T$ and so they can be considered to be equally populated in thermal equilibrium).

The element $\rho_{ps}^{(1)}$ describes the strength of the transition from s to p. As the input fields are relatively weak and only the s level is significantly populated, the other values of $\rho^{(1)}$ are assumed to be zero.

Using equations 6.14 and 6.12 and incorporating the term $(e^{i\omega t} + e^{-i\omega t})$ in the calculations, the value of $\rho_{ps}^{(1)}$ is found to be:

$$\rho_{ps}^{(1)} = \frac{\rho_{ss}^{(0)} V_{ps} \exp(-i\omega_1 t)}{\hbar((\omega_1 - \omega_{ps}) + i\Gamma_{ps})} \quad \text{Eqn. (6.15)}$$

where ω_1 is the frequency of the light exciting the transition from level s to level p. (There is an additional term in which the denominator is $\hbar((\omega_{ps} + \omega_1) - i\Gamma_{ps})$, but if the rotating wave approximation (RWA) is used then only the terms near resonance are kept. The rotating wave approximation assumes that the changes of interest take place over many optical cycles and so the higher frequency components, such as those at $\omega_{ps} + \omega_1$ average to zero. In reference 4 the conditions under which one can use the RWA are discussed, and it is summarised as being a near resonance, weak field approximation.)

Similarly the value for ρ_{sd} ($=\rho_{sd}^{(2)}$ as $\rho_{sd}^{(0)}$ and $\rho_{sd}^{(1)}$ are zero) is :

$$\rho_{sd} = \sum_{3P \text{ states}} \left[\frac{\rho_{ss} \exp(-i(\omega_1 + \omega_2)t)}{\hbar^2(\omega_1 - \omega_{ps} + i\Gamma_{ps})} \int_{-\infty}^t \exp(i[(\omega_1 + \omega_2) - \omega_{sd} + i\Gamma_{sd}](t - t')) V_{dp} V_{ps} dt' \right] \quad \text{Eqn. (6.16)}$$

The electron could have taken any one of several different routes to get from the 3S to the 3D levels, as shown in figure 6.11a, which is why the summation over all the 3P states is part of the matrix element for the transition from 3D to 3S.

The strength of the generated output wave is proportional to the quadrupole moment between the 3D and the 3S levels. The ensemble average of the quadrupole moment of the generated radiation (as opposed to the dipole or quadrupole upward transitions incorporated in the Liouville equation) is: $\langle Q_{ij}^{(2)} \rangle = \text{tr}(\rho Q_{ij}^{(2)})$ (i, j = x, y, z axes). (If the generated radiation were dipole radiation then the ensemble average would be: $\langle D_{ij}^{(1)} \rangle = \text{Tr}(\rho D_{ij}^{(1)})$). This ensemble average of quadrupole moments is given by $\sum_{s,d} \rho_{sd} \langle Q_{ij}^{(2)} \rangle_{sd}$.

Substituting for ρ_{sd} from equation 6.16 gives the general equation:

$$\langle \tilde{Q}_{ij}^{(2)} \rangle = \sum_{s,d} \sum_p \left[\frac{\rho_{ss}}{i\hbar^2(\omega_1 - \omega_{ps} + i\Gamma_{ps})} \int_{-\infty}^t \exp(i[(\omega_1 + \omega_2) - \omega_{sd} + i\Gamma_{sd}](t - t')) V_{dp} V_{ps} (Q_{ij}^{(2)})_{sd} dt' \right]$$

Eqn. (6.17)

 where $Q_{ij} = \tilde{Q}_{ij} \exp(-i(\omega_1 + \omega_2)t)$ as explained below

The summation over all the 3S and 3D states reflects that there are several routes for an electron to take from the 3D to the 3S levels and, as stated earlier, each of these upper levels could have been reached through any one of the P levels. The routes are of course restricted by the selection rules which are represented in this equation by the dipole and quadrupole moments.

The optical frequency variation expressed in the term $\exp(-i(\omega_1 + \omega_2)t)$ is removed to look only at the more slowly varying components at the frequencies of single and two photon detuning. (We are only interested in the overall value of the transition strength not its optical frequency variation).

The only unresolved quantities in the equation are now the three moments V_{dp} , V_{ps} , and $(Q_{ij}^{(2)})_{sd}$. It is simpler to work in spherical tensor elements when manipulating the tensors associated with each of these moments. The conversion from Cartesian tensors to Spherical tensors for the first and second order tensors associated with dipole and quadrupole moments respectively⁴ is given in Table 6.3.

First Order Tensor:		
$T_0^{(1)} = \sqrt{2} i T_{xy}^{(1)}$	$T_{\pm 1}^{(1)} = T_{zx}^{(1)} \pm i T_{zy}^{(1)}$	
Second Order Tensor:		
$T_0^{(2)} = \sqrt{\frac{3}{2}} T_{zz}^{(2)}$	$T_{\pm 1}^{(2)} = \mp T_{xz}^{(2)} - i T_{yz}^{(2)}$	$T_{\pm 2}^{(2)} = \frac{1}{2} (T_{xx}^{(2)} - T_{yy}^{(2)} \pm 2i T_{xy}^{(2)})$

Table 6.3- Conversion of Tensors

As stated previously, the dipole moment V_{ps} has two components - one associated with the strength of the interaction as stimulated by the electric field E_1 , and one associated with the selection rules of the dipole transition. The second part is expressed as $\langle p | D_{q_1}^{(1)} | s \rangle$. The term q_1 indicates which of the three tensor components is present. This in turn depends on the polarisation of the stimulating electric field. E_1 is itself a first order tensor, formed by the product $\mathbf{E} \cdot \mathbf{r}$, where \mathbf{r} is the vector associated with the direction of oscillation of the dipole. This tensor is called $E_{q_1}^{(1)}$. This dipole interaction is therefore $-e E_{q_1}^{(1)} \langle p | D_{q_1}^{(1)} | s \rangle$. (For a stimulated quadrupole transition the electric field tensor part of the quadrupole moment would be a second order tensor).

Similarly the second dipole transition is $-eE_{q_2}^{(1)} \langle d | D_{q_2}^{(1)} | p \rangle$. The Quadrupole radiation from 3D to 3S is dependent on both q_1 and q_2 and so is expressed as $\langle s | Q_q^{(2)} | d \rangle$. With these substitutions for V_{dp} , V_{ps} , and $(Q_{ij}^{(2)})_{sd}$ equation 6.17 becomes:

$$\langle \tilde{Q}_q^{(2)} \rangle = \sum_{s,d} \sum_p \left[\frac{P_{ss}}{i\hbar^2(\omega_1 - \omega_{ps} + i\Gamma_{ps})} \int_{-\infty}^t \exp\left\{i[(\omega_1 + \omega_2) - \omega_{sd} + i\Gamma_{sd}](t - t')\right\} e^2 E_{q_1}^{(1)} E_{q_2}^{(1)} \langle p | D_{q_1}^{(1)} | s \rangle \langle d | D_{q_2}^{(1)} | p \rangle \langle s | Q_q^{(2)} | d \rangle dt' \right]$$

Eqn. (6.18)

Each of the matrix elements embodies the selection rules of the transition. The most fundamental rules are those for spin and angular momentum. If one breaks each transition into two parts (spin 1/2 and spin -1/2), then by use of the Wigner-Eckart theorem the coupling of the operators ($D^{(1)}$ or $Q^{(2)}$) with the basis states ($|s\rangle$, $|p\rangle$ or $|d\rangle$) can be expressed in a purely angular momentum basis.

This factorisation can be expressed in either of two ways:

$$\begin{aligned} \langle \alpha' J' M' | T_q^{(k)} | \alpha J M \rangle &= (-1)^{J'-M'} \begin{bmatrix} J & k & J \\ -M' & q & M \end{bmatrix} \langle \alpha' J' || T^{(k)} || \alpha J \rangle \\ &= \frac{1}{\sqrt{2J'+1}} (JM, kq | J' M') \langle \alpha' J' || T^{(k)} || \alpha J \rangle \end{aligned}$$

Eqn. (6.19 a&b)

This describes the transition from a state with magnetic quantum numbers J and M to one of J' , M' via the operator $T_q^{(k)}$. (α and α' represent all the other quantum numbers which describe the state, for example, n , the principle quantum number, which is 3 for all the levels taking part here). The term $\langle \alpha' J' || T^{(k)} || \alpha J \rangle$ is the reduced matrix element of the operator $T_q^{(k)}$ and is independent of the magnetic quantum numbers. For the three transitions considered here it will be called Q_d^s , D_p^d and D_p^s . The magnetic quantum numbers used are L and m_l . The coefficients are Clebsch-Gordon coefficients additional to those discussed earlier. The first notation of the transition uses a 3-j matrix⁴. A list of useful relations between coupling coefficients is given at the end of the chapter.

The three matrix elements can be evaluated by applying the Wigner-Eckart theorem to the transition moments for the dipole and quadrupole transitions using the applicable selection rules. These calculations are included only so that the train of reasoning can be followed. They are however repetitive and can be skipped if one is not particularly concerned with a mathematical statement of the underlying physics. For this reason the calculations are enclosed within dotted lines.

Mathematical representation of the transition moments $\langle p|D_{q_1}^{(1)}|s\rangle$, $\langle d|D_{q_2}^{(1)}|p\rangle$ and $\langle s|Q_q^{(2)}|d\rangle$, embodying the selection rules for Dipole and Quadrupole Transitions

1) For the **3D -3S** transition:

$$\begin{aligned}\langle s|Q_q^{(2)}|d\rangle &= \langle 0\ 0|Q_q^{(2)}|2\ m_d - \frac{1}{2}\rangle S_a D_a Q_d^s \\ &\quad + \langle 0\ 0|Q_q^{(2)}|2\ m_d + \frac{1}{2}\rangle S_b D_b Q_d^s \\ &\quad (m_d = m_J \text{ for the D state})\end{aligned}$$

Using the Wigner-Eckart (W-E) theorem this can be rewritten in the two ways described previously as :

$$a) = \begin{bmatrix} 0 & 2 & 2 \\ 0 & q & m_d - \frac{1}{2} \end{bmatrix} D_a S_a Q_d^s + \begin{bmatrix} 0 & 2 & 2 \\ 0 & q & m_d + \frac{1}{2} \end{bmatrix} D_b S_b Q_d^s$$

This gives $q = -(m_d - \frac{1}{2})$ for spin 1/2 and $q = -(m_d + \frac{1}{2})$ for spin -1/2.

$$\begin{aligned}b) &= (2\ m_d - \frac{1}{2}, 2q|00) D_a S_a Q_d^s + (2\ m_d + \frac{1}{2}, 2q|00) D_b S_b Q_d^s \\ &= \frac{(-1)^{2+q}}{\sqrt{5}} S_a D_a Q_d^s \delta(-(m_d - \frac{1}{2}), q) + \frac{(-1)^{2+q}}{\sqrt{5}} S_b D_b Q_d^s \delta(-(m_d + \frac{1}{2}), q)\end{aligned}$$

2) For the **3S-3P** Transition

$$\begin{aligned}\langle p|D_{q_1}^{(1)}|s\rangle &= \langle 1\ m_p - \frac{1}{2}|D_{q_1}^{(1)}|0\ 0\rangle S_a P_a D_s^p \\ &\quad + \langle 1\ m_p + \frac{1}{2}|D_{q_1}^{(1)}|0\ 0\rangle S_b P_b D_s^p\end{aligned}$$

a) In 3-j symbols:

$$\begin{aligned}&= (-1)^{2-(m_p - \frac{1}{2})} \begin{bmatrix} 1 & 1 & 0 \\ -(m_p - \frac{1}{2}) & q_1 & 0 \end{bmatrix} S_a D_a D_s^p \\ &\quad + (-1)^{2-(m_p + \frac{1}{2})} \begin{bmatrix} 1 & 1 & 0 \\ -(m_p + \frac{1}{2}) & q_1 & 0 \end{bmatrix} S_b D_b D_s^p\end{aligned}$$

(This gives $q_1 = (m_p - \frac{1}{2})$ for spin = 1/2 and $q_1 = (m_p + \frac{1}{2})$ for spin = -1/2)

$$\begin{aligned}
 b) &= \frac{1}{\sqrt{3}} \left(00, 1q_1 \left| l \left(m_p - \frac{1}{2} \right) \right. \right) S_a P_a D_s^P + \frac{1}{\sqrt{3}} \left(00, 1q_1 \left| l \left(m_p + \frac{1}{2} \right) \right. \right) S_b P_b D_s^P \\
 &= \frac{1}{\sqrt{3}} S_a P_a D_s^P \delta \left(q_1, m_p - \frac{1}{2} \right) + \frac{1}{\sqrt{3}} S_b P_b D_s^P \delta \left(q_1, m_p + \frac{1}{2} \right)
 \end{aligned}$$

3) For the **3P-3D** Transition:

$$\begin{aligned}
 \langle d | D_{q_2}^{(1)} | d \rangle &= \langle 2 m_d - \frac{1}{2} | D_{q_2}^{(1)} | 1 m_p - \frac{1}{2} \rangle P_a D_a D_p^d \\
 &\quad + \langle 2 m_d + \frac{1}{2} | D_{q_2}^{(1)} | 2 m_p + \frac{1}{2} \rangle P_b D_b D_p^d
 \end{aligned}$$

a) In 3-j symbols:

$$\begin{aligned}
 &= (-1)^{2-(m_d-\frac{1}{2})} \begin{bmatrix} 2 & 1 & 1 \\ -(m_d-\frac{1}{2}) & q_2 & m_p-\frac{1}{2} \end{bmatrix} P_a D_a D_p^d \\
 &+ (-1)^{2-(m_d+\frac{1}{2})} \begin{bmatrix} 2 & 1 & 1 \\ -(m_d+\frac{1}{2}) & q_2 & m_p+\frac{1}{2} \end{bmatrix} P_b D_b D_p^d \\
 &= (-1)^{2+q} \begin{bmatrix} 2 & 1 & 1 \\ q & q_2 & q_1 \end{bmatrix} P_a D_a D_p^d \\
 &+ (-1)^{2+q} \begin{bmatrix} 2 & 1 & 1 \\ q & q_2 & q_1 \end{bmatrix} P_b D_b D_p^d
 \end{aligned}$$

(This gives the relation $q = -(q_1 + q_2)$, which in angular momentum terms means that the change of momentum on the way down is equal and opposite to that on the way up).

b)

$$\begin{aligned}
 &= \frac{1}{\sqrt{5}} (1q_1, 1q_2 | 2(-q)) P_a D_a D_p^d \delta \left(q_1, m_p - \frac{1}{2} \right) \delta \left(q, -(m_d - \frac{1}{2}) \right) \\
 &+ \frac{1}{\sqrt{5}} (1q_1, 1q_2 | 2(-q)) P_b D_b D_p^d \delta \left(q_1, m_p + \frac{1}{2} \right) \delta \left(q, -(m_d + \frac{1}{2}) \right)
 \end{aligned}$$

This last expression has to be evaluated separately for each value of q_1 and q_2 , where q_1 is Δm_ℓ for the 3S-3P transition and q_2 is Δm_ℓ for the 3P-3D transition. For the polarisations used in the experimental work q_1 and $q_2 = \pm 1$. The value of q is therefore ∓ 2 . (The $\Delta m_\ell = 0$ transitions are not radiated in the forward direction). While evaluating $(1q_1, 1q_2 | 2(-q))$ it is convenient to also determine $E_{q_1}^{(1)}$ and $E_{q_2}^{(1)}$, which are part of the dipole interactions.

i) $q_1, q_2 = +1, q = -2$ (see relation 6 at end of chapter)

$$(1q_1, 1q_2 | 2(-q)) E_{q_1}^{(1)} E_{q_2}^{(1)} = \sqrt{\frac{2!2!4!0!}{4!0!2!0!2!}} E_1^{(1)}(\omega_1) E_1^{(1)}(\omega_2) = E_1^{(1)}(\omega_1) E_1^{(1)}(\omega_2)$$

Using the tensor relations given in Table 6.3 gives :

$$\begin{aligned} E_1^{(1)}(\omega_1)E_1^{(1)}(\omega_2) &= \left(E_y^{(1)}(\omega_1) + i E_x^{(1)}(\omega_1)\right)\left(E_y^{(1)}(\omega_2) + i E_x^{(1)}(\omega_2)\right) \\ &= \left(E_y^{(1)}(\omega_1)E_y^{(1)}(\omega_2)\right) - \left(E_x^{(1)}(\omega_1)E_x^{(1)}(\omega_2)\right) = -\left(E_x^{(1)}(\omega_1)E_x^{(1)}(\omega_2)\right) \end{aligned}$$

(there is no polarisation component in the y direction.)

ii) Similarly, for $q_1, q_2 = -1, q = +2$

$$(1q_1, 1q_2|2(-q)) E_{q_1}^{(1)} E_{q_2}^{(1)} = -\left(E_x^{(1)}(\omega_1)E_x^{(1)}(\omega_2)\right)$$

With these substitutions for the transition moments, equation 6.18 becomes:

$$\langle \tilde{Q}_q^{(2)} \rangle = \sum_{s,d} \sum_p \left[\frac{P_{ss}}{i\hbar^2(\omega_1 - \omega_{ps} + i\Gamma_{ps})} \int_{-\infty}^t \exp(i[(\omega_1 + \omega_2) - \omega_{sd} + i\Gamma_{sd}](t - t')) T_q dt' \right]$$

Eqn. (6.20)

where $T_q = - \left[\begin{aligned} &\frac{(-1)^{2+q}}{5\sqrt{3}} (S_a)^2 (P_a)^2 (D_a)^2 D_s^p D_p^d Q_d^s \delta(q, -(m_d - \frac{1}{2})) \delta(q_1, (m_p - \frac{1}{2})) \\ &+ \frac{(-1)^{2+q}}{5\sqrt{3}} (S_b)^2 (P_b)^2 (D_b)^2 D_s^p D_p^d Q_d^s \delta(q, -(m_d + \frac{1}{2})) \delta(q_1, (m_p + \frac{1}{2})) \end{aligned} \right]$

$$\times \left(e^2 \left(E_x^{(1)}(\omega_1) E_x^{(1)}(\omega_2) \right) \right)$$

Eqn. (6.21)

The two quadrupole moments which can radiate along the forward direction are $Q_{xy}^{(2)}$ and $Q_{zy}^{(2)}$. In terms of spherical tensor components these are $Q_{xy}^{(2)} = \frac{-i}{2} (Q_2^{(2)} - Q_{-2}^{(2)})$ and $Q_{zy}^{(2)} = \frac{i}{2} (Q_1^{(2)} + Q_{-1}^{(2)})$. Only the first of these quadrupole moments is driven by σ polarisation. If eqn 6.20 is converted to Cartesian co-ordinates and the constants are removed to a general term, $K = -\frac{e^2 P_{ss}}{\hbar^2 20\sqrt{3}} D_s^p D_p^d Q_d^s$, then the quadrupole moment is:

$$\begin{aligned} \langle \tilde{Q}_{xy}^{(2)} \rangle &= K \left(E_x^{(1)}(\omega_1) E_x^{(1)}(\omega_2) \right) \\ &\times \sum_{s,d} \sum_p \left[\frac{(B_2 - B_{-2})}{(\omega_1 - \omega_{ps} + i\Gamma_{ps})} \int_{-\infty}^t \exp(i[(\omega_1 + \omega_2) - \omega_{sd} + i\Gamma_{sd}](t - t')) dt' \right] \end{aligned}$$

Eqn. (6.22)

$$\begin{aligned} \text{where} \quad B_2 &= \left[\begin{aligned} &(S_a)^2 (P_a)^2 (D_a)^2 \delta(2, -(m_d - \frac{1}{2})) \delta(-1, (m_p - \frac{1}{2})) \\ &+ (S_b)^2 (P_b)^2 (D_b)^2 \delta(2, -(m_d + \frac{1}{2})) \delta(-1, (m_p + \frac{1}{2})) \end{aligned} \right] \\ \text{and} \quad B_{-2} &= \left[\begin{aligned} &(S_a)^2 (P_a)^2 (D_a)^2 \delta(-2, -(m_d - \frac{1}{2})) \delta(1, (m_p - \frac{1}{2})) \\ &+ (S_b)^2 (P_b)^2 (D_b)^2 \delta(-2, -(m_d + \frac{1}{2})) \delta(1, (m_p + \frac{1}{2})) \end{aligned} \right] \end{aligned}$$

Evaluating the integral gives the general expression:

$$\langle \tilde{Q}_{xy}^{(2)} \rangle = i K (E_x^{(1)}(\omega_1) E_x^{(1)}(\omega_2)) \sum_{s,d} \sum_p \left[\frac{(B_2 - B_{-2})}{(\omega_1 - \omega_{ps} + i\Gamma_{ps})((\omega_1 + \omega_2) - \omega_{ds} + i\Gamma_{ds})} \right] \quad \text{Eqn. (6.23)}$$

The final factor which has to be taken into account when predicting the line profile of the output is the effect of Doppler broadening. This is only significant on the 3D-3S transition where the lasers are tuned near two photon resonance. (The lasers are generally tuned well off single photon resonance to avoid complications with having two sets of resonances and absorptions). The frequency emitted by an atom travelling at a velocity v_y is $\omega' = \omega + kv_y$, where k is the wavevector of the transition of frequency ω . The distribution of velocities in a gas with mass M at a temperature T is given by the Maxwell velocity distribution, where $f(v_y) = \sqrt{\frac{M}{2\pi k_B T}} \exp\left(-\frac{Mv_y^2}{2k_B T}\right)$. With this variation in the transition frequency, Eqn. (6.23) becomes:

$$\begin{aligned} \langle \tilde{Q}_{xy}^{(2)} \rangle &= i K e^2 (E_x^{(1)}(\omega_1) E_x^{(1)}(\omega_2)) \sqrt{\frac{M}{2\pi k_B T}} \\ &\times \sum_{s,d} \sum_p \left[\frac{(B_2 - B_{-2})}{(\omega_1 - \omega_{ps} + i\Gamma_{ps})} \int_{-\infty}^{\infty} \frac{\exp(-Mv_y^2 / 2k_B T)}{((\omega_1 + \omega_2) + k_{ds} v_y - \omega_{ds} + i\Gamma_{ds})} dv_y \right] \end{aligned} \quad \text{Eqn. (6.24)}$$

Using the substitutions $K_2 = \sqrt{\frac{k_{ds}^2 2k_B T}{M}}$ and $v_y = \frac{K_2}{k_{ds}} t$, this equation simplifies to :

$$\langle \tilde{Q}_{xy}^{(2)} \rangle = \frac{i K}{K_2} (E_x^{(1)}(\omega_1) E_x^{(1)}(\omega_2)) \sum_{s,d} \sum_p \left[\frac{(B_2 - B_{-2})}{(\omega_1 - \omega_{ps} + i\Gamma_{ps})} Z \left(\frac{((\omega_1 + \omega_2) - \omega_{ds} + i\Gamma_{ds})}{K_2} \right) \right] \quad \text{Eqn. (6.25)}$$

Where $Z\left(\frac{((\omega_1 + \omega_2) - \omega_{ds} + i\Gamma_{ds})}{K_2}\right)$ is a plasma dispersion function defined by:

$$Z(a + i b) = \frac{1}{\sqrt{\pi}} \int_{-\infty}^{\infty} \frac{\exp(-t^2) dt}{t - (a + i b)}$$

This final equation describes the contribution to the quadrupole moment from each of the possible transitions between the 3D level and the 3S level, in terms of the detuning from both single and two photon resonance and the magnetic field mixing of the Zeeman sublevels. The intensity of the output as seen when scanning the combined laser frequencies is given by $I \propto \left\langle \left| \tilde{Q}_{xy}^{(2)} \right|^2 \right\rangle$. This has kindly been calculated by Mr. R. Moseley using a Sun workstation to give the theoretical lineshapes shown in figure 6.13.

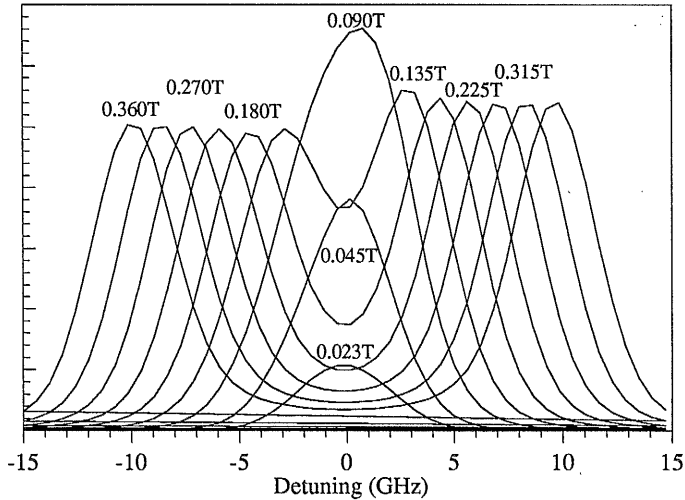


Figure 6.13- Theoretical Line Profiles

The figure shows the variation of the expected output as the magnetic field is increased. This has two effects - the first is that the output splits into two lines, corresponding to the settling of each of the 3S levels to a predominantly spin 1/2 or spin -1/2 eigenstate. The second is that the quadrupole transition moment (which depends on mixing of the Zeeman sub-levels) is proportional to the magnetic field until the Zeeman splitting of the two components is comparable to the Doppler broadening of the lines. At this point the quadrupole moment saturates and the output power is constant. As the output power is proportional to the square of the transition moments, the power is also

proportional to the square of the magnetic field until the line splitting is greater than the Doppler width. The experimental results of varying the magnetic field on the power are presented in chapter 7.

The DQD(3S-3P-4P) Route for Sum Frequency Mixing

For the DQD route the calculation of the output with detuning is largely similar. The main difference is that the two input fields at ω_1 and ω_2 now excite a dipole and a quadrupole transition, while the sum frequency radiation is a dipole transition. The density matrix element for this transition is :

$$\rho_{s4p} = \sum_p \left[\frac{\rho_{ss} \exp(-i(\omega_1 + \omega_2)t)}{i\hbar^2 (\omega_1 - \omega_{3ps} + i\Gamma_{3ps})} \int_{-\infty}^t \exp\left(i\left[(\omega_1 + \omega_2) - \omega_{s4p} + i\Gamma_{s4p}\right](t - t')\right) V_{4p3p} V_{3ps} dt' \right]$$

Eqn. (6.26)

Similarly the ensemble average of the dipole emission is $\langle D_{ij}^{(1)} \rangle = \text{Tr}(\rho D_{ij}^{(1)})$.

As the quadrupole transition is now on the upward route it is no longer the case that there will be no forward emission of the output without a magnetic field. Instead it is rather that the transition to the 4P level will not be excited unless the magnetic field is present. The quadrupole transition stimulated by the interaction with the EM field is:

$$\frac{1}{6} Q_{yx}^{(2)} kE \frac{1}{2i} (e^{i\omega t} - e^{-i\omega t})$$

When converted to spherical polar co-ordinates the transition from the 3P to the 4P level (for σ transitions) becomes:

$$\frac{-i}{12} k e \left\{ E_2^{(2)} \langle 4p | Q_2^{(2)} | 3p \rangle - E_{-2}^{(2)} \langle 4p | Q_{-2}^{(2)} | 3p \rangle \right\} (e^{i\omega_2 t} + e^{-i\omega_2 t}) \text{Eqn. (6.27)}$$

This leads to the general equation for the expectation value of the output as:

$$\begin{aligned} \langle \tilde{D}_q^{(1)} \rangle &= \left(\frac{-ik_2}{12} \right) \sum_{s,4p} \sum_{3p} \frac{\rho_{ss}}{i\hbar^2 (\omega_1 - \omega_{3ps} + i\Gamma_{3ps})} \int_{-\infty}^t \exp\left(i\left[(\omega_1 + \omega_2) - \omega_{s4p} + i\Gamma_{s4p}\right](t - t')\right) \\ &\times e^2 E_{q1}^{(1)} \langle 3p | D_{q1}^{(1)} | s \rangle \langle s | D_q^{(1)} | 4p \rangle \left[E_2^{(2)} \langle 4p | Q_2^{(2)} | 3p \rangle - E_{-2}^{(2)} \langle 4p | Q_{-2}^{(2)} | 3p \rangle \right] dt' \end{aligned}$$

Eqn. (6.28)

Each of these two parts can be resolved using the Wigner-Ekart theorem and the derivation then proceeds as shown previously. This leaves the final result for the slowly varying expectation value of the ensemble average of the output as:

$$\langle \tilde{D}_{xy}^{(1)} \rangle = \frac{i K'}{K_2} \left(E_x^{(1)}(\omega_1) E_x^{(2)}(\omega_2) \right) \sum_{s,d} \sum_p \left[\frac{(B_2 - B_{-2})}{(\omega_1 - \omega_{3ps} + i\Gamma_{3ps})} Z \left(\frac{((\omega_1 + \omega_2) - \omega_{4ps} + i\Gamma_{4ps})}{K_2} \right) \right]$$

Eqn. (6.29)

where:
$$K' = -\frac{e^2 P_{ss}}{\hbar^2 20\sqrt{3}} D_s^{3p} Q_{3p}^4 P_{4p}^s, \quad K_2 = \sqrt{\frac{k_{4ps}^2 2k_B T}{M}}$$

and

$$B_2 = \left[\begin{array}{l} (S_a)^2 (3P_a)^2 (4P_a)^2 \delta\left(1, (m_{4p} - \frac{1}{2})\right) \delta\left(-1, (m_{3p} - \frac{1}{2})\right) \\ + (S_b)^2 (3P_b)^2 (4P_b)^2 \delta\left(1, (m_{4p} + \frac{1}{2})\right) \delta\left(-1, (m_{3p} + \frac{1}{2})\right) \end{array} \right]$$

$$B_{-2} = \left[\begin{array}{l} (S_a)^2 (3P_a)^2 (4P_a)^2 \delta\left(-1, (m_{4p} - \frac{1}{2})\right) \delta\left(1, (m_{3p} - \frac{1}{2})\right) \\ + (S_b)^2 (3P_b)^2 (4P_b)^2 \delta\left(-1, (m_{4p} + \frac{1}{2})\right) \delta\left(1, (m_{3p} + \frac{1}{2})\right) \end{array} \right]$$

The form of the expected output with magnetic field is largely similar in both the DDQ and DQD cases. In practise bulk effects due to phase-matching also play a very significant part in the output power of any sum frequency interaction. Experimental results for both routes are shown in the following chapter.

Effects of Phase Matching, Dispersion and Focusing on Output Power

The theoretical derivation of the output moment is an average value for the system, taking into account the resonant enhancement of tuning near to the atomic levels and of the magnetic field mixing of the Zeeman sublevels. For any particular value of detuning and magnetic field it can be seen as a dependence on input intensities and an effective nonlinear coefficient. This means that we have calculated the generated output power per atom per unit length of vapour, however, as in the discussion of the theory of harmonic generation in crystals, there is an added dependence on both the phase matching of the three waves and the focusing of the beams. The focusing itself effects the optimum phase matching conditions. A general expression for the output power takes the form¹⁶:

$$P_{out} \propto P_1 P_2 \ell h(\sigma, \mu, \xi) \quad \text{Eqn. (6.30)}$$

where P_1 and P_2 are the input powers at ω_1 and ω_2 , ℓ is the length of the medium and $h(\sigma, \mu, \xi)$ is a focusing parameter dependent on phase mismatch, focal position and focal strength. The two extreme conditions of weak focusing and strong focusing will be addressed separately.

Weak/No Focusing

In the limit of weak focusing equation 6.30 has the form of the well known phase matching equation given in Chapter 2:

$$P_{out} \propto P_1 P_2 \frac{\omega_1 \omega_2}{n_1 n_2 n_3 w_{o1} w_{o2}} N^2 \ell^2 \frac{\sin^2(\Delta k \ell / 2)}{(\Delta k \ell / 2)^2} \quad \text{Eqn. (6.31)}$$

where w_{o1} and w_{o2} are the waists of the input waves, n_1 n_2 and n_3 are the refractive indices experienced by the three waves, and N is the number density of the sodium atoms (the average generated moment as given in eqn 6.25 is per atom, therefore the generated power is proportional to N^2).

There are several techniques with which to achieve phase matching in vapours⁵, but the one used in all this work is that which uses the dispersion associated with the atomic resonances of the sodium itself. The value of the phase mismatch, Δk , is:

$$\Delta k = 2\pi \left[\frac{n_3}{\lambda_3} - \frac{n_2}{\lambda_2} - \frac{n_1}{\lambda_1} \right] \quad \text{Eqn. (6.32)}$$

where the refractive index for each of the three wavelengths is given by the Sellmeier equation for atomic vapours⁵:

$$n(\lambda) - 1 = N \frac{r_e}{2\pi} \sum_{i,j} \frac{\alpha_i f_{ij}}{(1/\lambda_{ij})^2 - (1/\lambda)^2} \quad \text{Eqn. (6.33)}$$

This gives the refractive index experienced by a wave of wavelength λ , in terms of its dependence on each of the transitions from level i to level j , where f_{ij} is the oscillator strength of the transition, α_i is the fractional population of level i , and λ_{ij} is the resonant wavelength of the transition. The term r_e is the classical electron radius, 2.181×10^{-15} m. For both sum frequency routes it is assumed that the transfer of population out of the ground state is negligible when tuned off resonance with the D lines. This means that in both cases the refractive index of the wave at frequency ω_2 is close to 1. For the DDQ transition the oscillator strength of the 3D-3S quadrupole transition is tiny¹⁷ compared to that of the 3S-3P transition and can be ignored. The phase mismatch in this case is wholly dependent on the change in refractive index experienced by the 3S-3P (≈ 589 nm) radiation as one tunes near to the D lines and the variation in the atomic number density, N . For sodium this variation in N with temperature is given by the expression¹⁸:

$$N = 9.66084 \times 10^{18} \frac{\exp(-(12423.3/T) + 17.3914)}{T} \text{ atoms/cm}^3 \quad \text{Eqn. (6.34)}$$

(The number density in these experiments is usually up to $10^{21}/\text{m}^3$, for temperatures up to 400°C .) Figure 6.14 shows the phase mismatch values of the SFM output for two different temperatures, 250°C and 300°C , as the wavelength of the dye laser is set to different positions near the D lines.

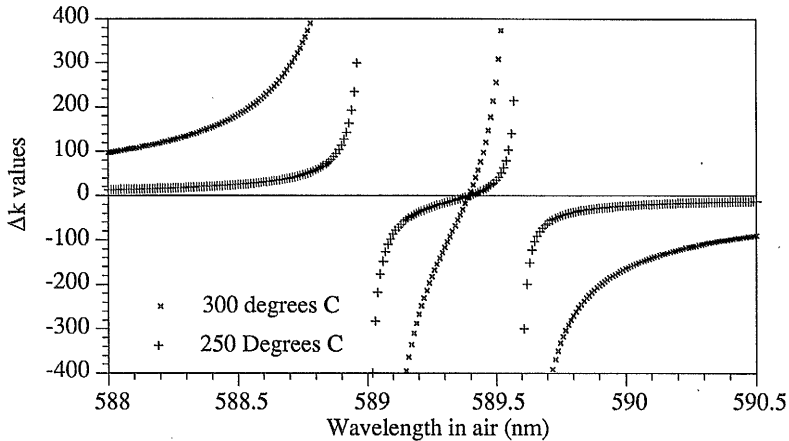


Figure 6.14 - Variation of Δk vs single photon detuning, both routes

The length of oven used in the experiments is 10 cm and so, even at relatively large detuning from single photon resonance, $\Delta k l/2$ will go through a couple of cycles as the temperature is raised. This effect is greater the nearer the dye laser is tuned to single photon resonance. This has the consequence that although it is advantageous to be near the D lines in order to enhance the output power, the maximum vapour density achievable before being limited by phase matching oscillations of the output power is also lessened. One further notable effect is that there is a point at which the Δk value is zero due to the competing influence of the lines. At this point there should always be perfect phase-matching no matter what the vapour density, and the power is proportional to N^2 . Figure 6.15 shows the variation in output power for three wavelengths, one at $\Delta k = 0$ (589.393nm), one near a D line resonance (588.5nm), and one at an in-between value (588nm). (All these wavelengths are for air rather than vacuum).

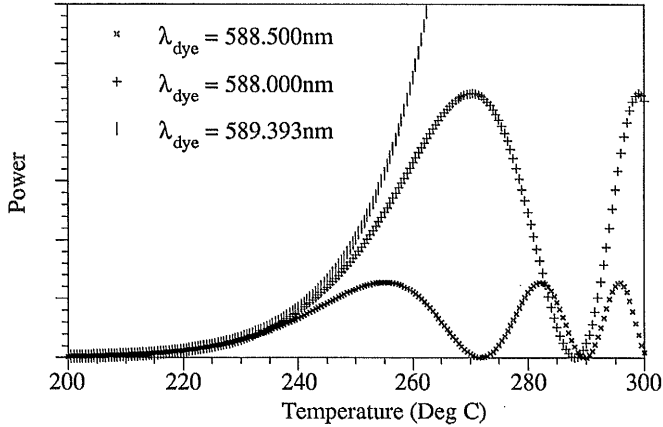


Figure 6.15 - Variation of Power vs. Temperature

For the DQD route there is an added contribution to the phase mismatch from the dispersion associated with the 4P-3S route. This contribution, ignoring the contribution from the dye laser detuning, is shown in figure 6.16 for two vapour temperatures. Although the oscillator strengths are not large (around a hundredth that of the 3S-3P transition), the lasers are tuned much closer to two photon resonance than to single photon resonance so that both contributions are significant. Although in theory the values of Δk at resonance change from positive to negative infinity, in practise the resonance peaks are blunted by the Doppler effect.

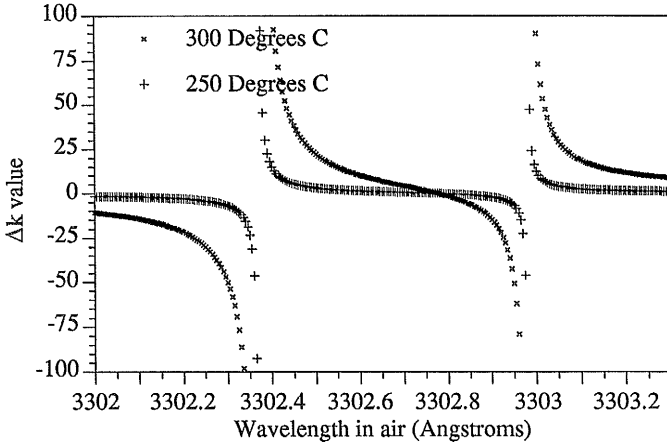


Figure 6.16 - Variation of Δk with two photon detuning on DQD route, assuming that the only dispersion is on the 4P-3S transition. In reality this variation of Δk is shifted up or down in value depending the dispersion on the 3S-3P transition.

Focused Case

The effect of focusing a Gaussian beam within a parametric medium is treated in detail by several authors^{16,19}. The approach given here is that of Boyd and Kleinman. In their treatment they look at the propagation into the far field of the second harmonic of a focused beam and then assume that the power in the second harmonic is generated by a small section of the beam around the focus and integrate over that length. The relation is then rearranged into certain key parameters related to the confocal parameter of the beam, the phase mismatch, the position of the focus within the medium, absorption and double refraction. The last three can be ignored as the vapour is tuned off resonance, is not birefringent and in general the beam is assumed to be focused into the centre of the oven. This reduces Eqn (6.30) to :

$$P_{\text{out}} \propto P_1 P_2 l h(\sigma, \xi), \quad \text{where } h(\sigma, \xi) = \frac{1}{4\xi} \left| \int_{-\xi}^{\xi} \frac{\exp(i \sigma r) dr}{1 + i r} \right|^2 \quad \text{Eqn. (6.35)}$$

The two parameters are $\xi = l/b$, where l is the length of the medium and b is the confocal parameter of the input waves and $\sigma = -\frac{1}{2} b \Delta k$. (Note that in this paper Δk is opposite in sign to the convention usually used so that here the sign of σ is changed to keep to the standard convention given in Eqn. 6.32). The focusing parameter, ξ , is used

in the following graphs to indicate the strength of focusing, where 0.01 is the unfocused case and 1 is a reasonably tight focus.

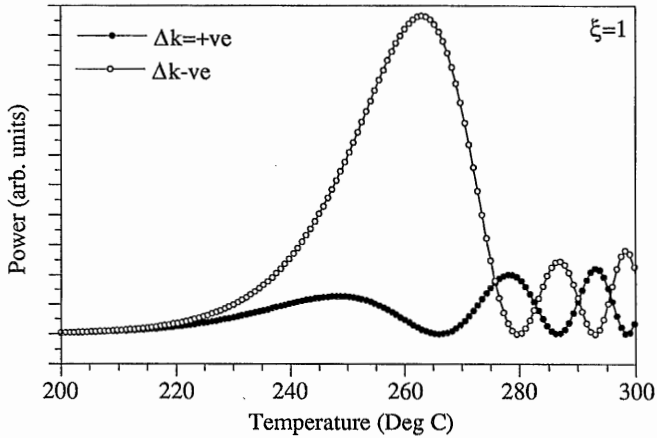
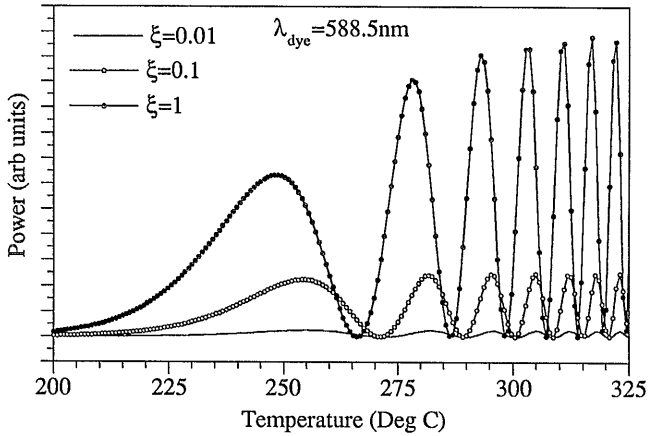
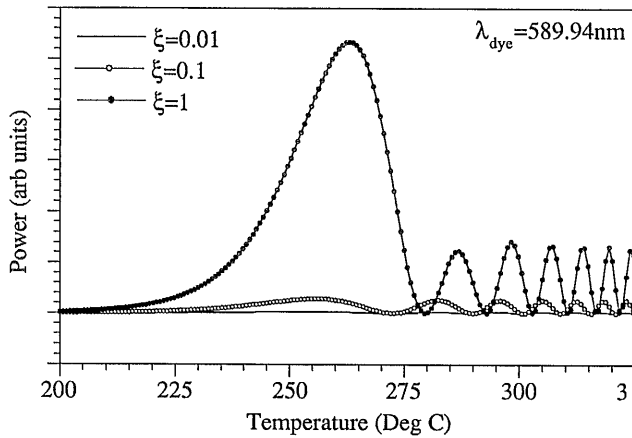


Figure 6.17 - Effect of focusing with opposite sign of Δk

Figure 6.17 shows that the effect of focusing on the output power is dramatically affected by the sign of the phase mismatch caused by the absorption lines. The two traces on the graph correspond to wavelengths which have equal but opposite values of Δk . For regions in which Δk is negative strong focusing causes an extremely large first peak in power followed by relatively small subsidiary peaks whereas the Δk positive region has a much smaller initial peak and a series of slightly larger later peaks. This appears to indicate that the phase change on passing through the focus is negative in the Δk -ve case, and +ve in the Δk +ve case. Having a negative phase change increases the temperature at which back conversion of the SFG occurs and as the power is also proportional to temperature, greater outputs are possible in this region of the spectrum than in the Δk +ve region. The effect of changing the position of the first maxima and minima are also seen in figures 6.18 and 6.19.

Figure 6.18 - Effects of focusing on Δk +ve regionFigure 6.19- Effects of focusing on Δk -ve region

Both figures 6.18 and 6.19 show the output power vs. temperature for three different values of the focusing parameter. The lowest powers in each case are for unfocused beams, but as the foci become tighter it can be seen that in the Δk +ve case the increase in power is offset by the lower temperatures at which the maxima occur. The effect of focusing is most dramatic in the Δk -ve case in which the increase in power due to focusing is complemented by the shifting of the first maxima, which leads to the conclusion that the greatest SFM power will be in this region.

Conclusion

This chapter has looked at the theory behind sum-frequency generation in vapours with regard to two different transition routes. The two routes differ in that one uses two dipole transitions in the upward route and emits via a quadrupole transition, while the other uses both a quadrupole and a dipole transition in the upward route and emits via a dipole transition. The expected dependence of the output power on magnetic field, two-photon detuning, vapour temperature and input beam focusing have all been examined and the experimental results will be presented in the following chapter.

Relations Between Coupling Coefficients

- 1) Three j symbols are invariant under cyclic permutations:

$$\begin{bmatrix} a & b & c \\ \alpha & \beta & \gamma \end{bmatrix} = \begin{bmatrix} c & a & b \\ \gamma & \alpha & \beta \end{bmatrix} = \begin{bmatrix} b & c & a \\ \beta & \gamma & \alpha \end{bmatrix}$$

but not under non-cyclic permutations:

$$\begin{bmatrix} a & b & c \\ \alpha & \beta & \gamma \end{bmatrix} = (-1)^{a+b+c} \begin{bmatrix} c & b & a \\ \gamma & \beta & \alpha \end{bmatrix}$$

2) $\alpha + \beta + \gamma = 0$

3) $(JM, kq|J' M') = (-1)^{J-M'} \sqrt{2J+1} \begin{bmatrix} J & k & J \\ -M' & q & M \end{bmatrix}$

4) $(JM, 00|J' M') = (00, JM|J' M') = \delta(J, J') \delta(M, M')$

5) $(JM, kq|00) = \frac{(-1)^{J-M}}{\sqrt{2J+1}} \delta(M, -q)$

- 6) When $J'=J+k$ then:

$$(JM, kq|J' M') = \sqrt{\frac{(2J)!(2k)!(J+k+M+q)!(J+k-M-q)!}{(2J+2k)!(J-M)!(J+M)!(k-q)!(k+q)!}}$$

Note: These relations are mainly compiled from Shore, but typographical errors in the book have led to contradictions within the work with regard to conversion to and from $3j$ symbols. The correct relations can be found by comparison of Shore with Condon and Odabassi²⁰ and with I I Sobelman²¹.

References

- 1 B D Sinclair - Second Harmonic Generation in Sodium Vapour Induced by a Magnetic Field- Ph. D Thesis, St. Andrews University, 1987
- and:* B D Sinclair and M H Dunn - Continuous-wave second harmonic generation in sodium vapour - Phys. Rev. A, Vol. 34, No. 5, pgs 3989-3999, 1986
- 2 A J Poustie - Magnetic-field induced sum frequency Mixing in Sodium Vapour - Ph. D Thesis, St. Andrews University, 1990
- and:* A J Poustie and M H Dunn - Magnetic-field induced sum-frequency mixing in sodium vapour - Phys. Rev. A, Vol. 47, No. 2, pgs 1365-1377, 1993
- 3 H Uchiki et al - Optical Second Harmonic Generation in Gases in Magnetic Field - J. Phys. Soc. Japan, Vol. 52, No. 9, pgs 3010-3018, 1983
- 4 B W Shore - The Theory of Coherent Atomic Excitation - Vols 1 and 2, J Wiley and Sons, New York, 1990
- 5 D C Hanna et al - Nonlinear Optics of Free Atoms and Molecules - Springer-Verlag, Berlin, 1979
- 6 D S Bethune et al - Optical Quadrupole Sum-Frequency Generation in sodium Vapour - Phys. Rev. Lett., Vol. 37, No. 7, pgs 431-434, 1976
- 7 G K Woodgate - Elementary Atomic Structure - Second Edition, Oxford Science Publications, Oxford, 1986
- 8 R S Finn and J F Ward - dc-Induced Optical Second Harmonic Generation in the inert Gases - Phys. Rev. Lett., Vol. 26, No. 6, pgs 285-289, 1971
- 9 K Miyazaki et al - Spontaneous-Field-Induced Optical Second-Harmonic Generation in Atomic Vapours - Phys. Rev. Lett., Vol. 43, No. 16, pgs 1154-1157, 1979
- 10 L Windholz and M Musso - Zeeman and Paschen-Back-effect of the hyperfine structure of the sodium D_2 line - Z Phys D - Atoms, Molecules and Clusters 8, pgs 239-249, 1988
- 11 E U Condon and G H Shortly - The Theory of Atomic Spectra - Cambridge University Press, Cambridge, 1953
- 12 N F Ramsey - Molecular Beams - Clarendon Press, Oxford, 1956
- 13 G Breit and I I Rabi - Measurement of Nuclear Spin - Phys. Rev., Vol. 38, Letter, pg 2082, 1931
- 14 W L Wiese and G A Martin - Atomic Spectroscopy - A Physicist's Desk Reference: The Second Edition of Physics Vade Mecum, Section 5, American Institute of Physics, 1989
- 15 A Yariv - Quantum Electronics - Second Edition, J Wiley and Sons, New York, 1975

References

- 16 G D Boyd and D A Kleinman - Parametric Interaction of Focused Gaussian Light Beams - J.App.Phys, 39, 1968, pgs 3597-3639
- 17 C E Tull and M Jackson - Electric Quadrupole Transitions in Na I, Mg II and Al III - Can. J. Phys, Vol. 50, pgs 1169-1174, 1972
- 18 R B Miles and S E Harris - Optical Third Harmonic Generation in Alkali Metal Vapours - IEEE J. QE, Vol. QE-9, No. 4, pgs 470-484, 1973
- 19 S Guha and J Falk - The Effects of Focusing in the three-frequency parametric upconverter - J App. Phys, Vol. 51, No. 1, pgs 50-60, 1980
- 20 E V Condon and H Ahabassi - Atomic Structure - Cambridge University Press, Cambridge, 1980
- 21 I I Sobelman - Atomic spectra and Radiative Transitions - Springer-Verlag, Berlin, 1979

Chapter 7

Sum Frequency Generation In Sodium Vapour via Two Contrasting Routes

In the previous chapter the theory behind second order frequency conversion using an atomic vapour was described, in particular with regard to the expected behaviour of the two sodium transitions 3D-3S and 4P-3S as the outputs in resonantly enhanced sum frequency generation. This chapter deals with the experimentally observed behaviour of these two transitions and discusses both their lineshapes and phase-matching characteristics. The two transitions differ in that the first is a quadrupole and the second a dipole transition and it was found that the change in the type of coupling between the upper and lower levels had a significant effect on phase-matching. Despite the fact that dipole transitions are usually far stronger than quadrupole transitions, it is the quadrupole output route that is here by far the stronger. This is due to the fact that the enhancement depends on the product of the three transition moments. Although both have two dipole and one quadrupole transition, the 3S-3P-3D-3S route has a product 25 times stronger than the 3S-3P-4P-3S route. This, coupled with the adverse effects on the dipole transition due to its greater dispersion, make the quadrupole emission the more efficient sum frequency converter.

Experimental Equipment

In order to look at the two transitions, two lasers were used to provide the uptake routes. One of these was the Ti:sapphire laser described previously and the other was a Spectra Physics 380D dye laser. This particular laser has been used at St. Andrews in previous experiments involving atomic vapours and its operation is described in detail both in the theses relating to that work¹⁻³ and in the manufacturers literature⁴. The dye laser is very similar to the Ti:sapphire laser in construction, being a unidirectional ring laser with a birefringent filter and etalon for tuning and mode selection. The etalon in the dye laser, however, is an air-spaced, piezo-controlled etalon and it and two counter-rotating plates allow the output to be scanned by 30GHz without mode hops. The laser is locked to two reference etalons, one of which has a tunable length which feeds back to scan the laser, and the system as a whole has a specified linewidth of 500kHz. A schematic of this laser is shown in figure 7.1.

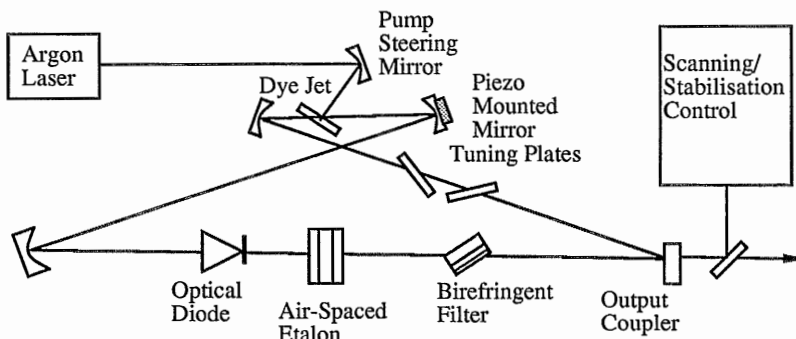


Figure 7.1 - Schematic of Dye Laser Cavity

The dye used was Rhodamine 6G which covers the tuning range from 570nm-630nm. The pump laser was a Spectra-Physics 2030 argon ion laser operating on all lines. This laser was also used to pump the Ti:sapphire laser and was usually run at 14W output with the power split by a 50:50 beam splitter. (Although the pump is capable of 20W, the beam profile degrades from TEM₀₀ to TEM^{*}₀₁ at higher powers and the Ti:sapphire laser output decreases instead of increasing at pump powers above 14W). The outputs were typically 200mW at 589nm and 300mW in the IR (750nm or 818nm). As an absolute frequency reference for the dye laser the leakage power through the high reflector opposite the output coupler was passed through an iodine cell.

A schematic of all the equipment used in this experiment is shown in figure 7.2. (The main dye, Ti:sapphire and UV beams are drawn in bold and the monitoring beams are shown as lighter lines. The dotted lines are electrical connections.) The output polarisations of both the sum-frequency lasers were controlled by rotators - in the case of the dye laser this was by a telescopic arrangement which could rotate the polarisation from horizontal to vertical and for the Ti:sapphire laser there was a polariser cube and half-wave plate capable of changing the polarisation to any plane. The longitudinal mode structure of each could be seen by the transmission of two scanning confocal etalons. Each laser also had its own full or partial scanning control and stabilisation system. The output of the dye laser was usually chopped so that even small amounts of sum frequency power could be seen by phase-sensitive detection. The outputs of each laser were combined using a dichroic mirror and focused (or not as the case might be) into the sodium over. The oven itself is described in both references 1 and 2. It is a heat pipe arrangement with a central heated body 10cm long and protruding tubes tipped by quartz windows which bring the total length to 27cm. The oven could be pumped down to a pressure of .01mbar by a rotary pump and a diffusion pump. The oven was filled to a pressure of 1mbar of argon buffer gas before heating for all the experiments reported

here. The sodium itself was deposited in lumps inside the tube in sufficient quantities that the vapour density was controlled by the oven temperature and not by the available sodium. Over a number of cycles the sodium would migrate from the centre of the oven towards the ends where the temperature was cooler and had to be periodically scraped back into the centre. There was also an occasional problem which occurred if the temperature was raised too high or cycled too often in which all the sodium became dispersed or oxidised and the vapour pressure 'crashed'. This was always characterised by an increase in the temperature of the first phase-matched peak of the output and a decrease in the absorption of the dye laser radiation on the 589nm resonance, either of which could be used to confirm that the sodium needed to be replaced.

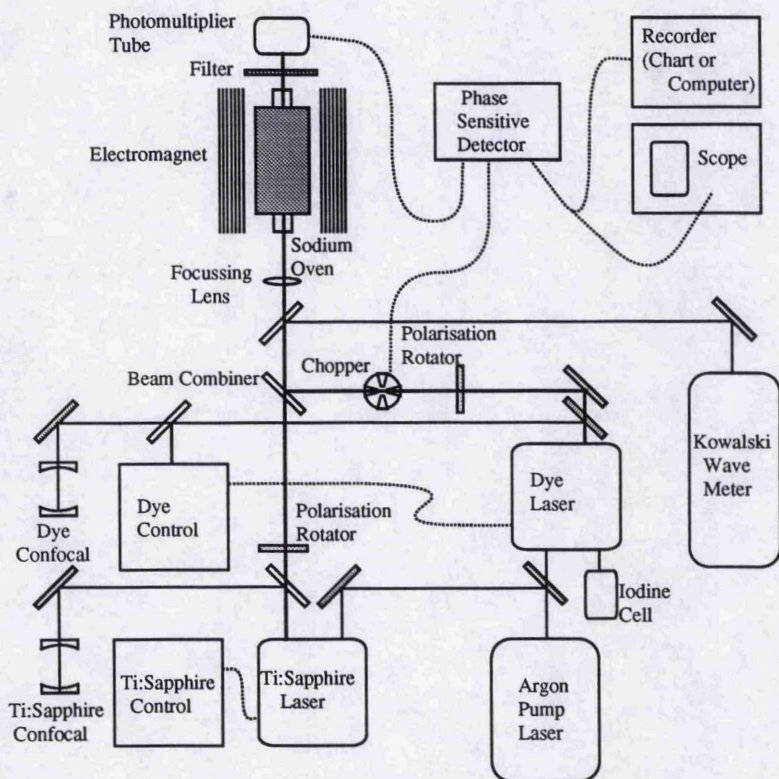


Figure 7.2 - Schematic of Sum-Frequency Experiment

The oven was enclosed between the pole pieces of a Newport Instruments Type A electromagnet. The field within the oven was calibrated by measuring the splitting of the sodium D (589nm) lines which can be theoretically calculated as described in chapter 6. (Agreement between theory and experiment in the splitting of the D lines has

been well documented over the years and this technique provides the best method of calibrating the field actually experienced by the vapour as opposed to that generated at the pole pieces). This field was found to be 0.045T/A and as the current through the coils could be run at up to 12A the maximum field was 0.54T. The detector used for the sum-frequency radiation was a Hamamatsu photomultiplier, Type 931B. The light was filtered using two UG11 filters to screen out the dye and IR radiation. For the 4P-3S transition the IR is at 750nm where the UG11 filter has a secondary peak and during these experiments an additional BG38 filter was used. Both the chopped signal and the chopper frequency were input to a Brookdeal Type 401 lock-in amplifier, and the output was displayed on a digital storage scope and recorded on either a chart recorder or computer (Elonex PC). The wavelengths of both the dye and the Ti:sapphire lasers could be measured to an accuracy of 10^{-6} by a Kowalski wavemeter (detailed in ref 3).

Wavelengths - Vacuum or Air

The first sum-frequency route studied was the DDQ route 3S-3P-3D-3S. In both this and the DQD route the dye laser is used for the 3S-3P dipole transition. The vacuum wavelength of the $3S_{1/2}$ - $3P_{1/2}$ (D_1 line) transition is 589.755nm. The refractive index correction for dry air at 15°C for 590nm is $n^5 (n-1) \times 10^7 = 2765$. The wavelength in air is therefore 589.592nm. The corresponding vacuum and air values for the D_2 line ($3S_{1/2}$ - $3P_{3/2}$) are 589.158nm and 588.995nm respectively. During this thesis all experimental wavelengths are for air unless stated otherwise. The wavelengths of the 3P-3D, the 3D-3S, the 3P-4P and the 4P-3S transitions all have similar refractive index corrections for air. Tables 7.1-7.5 give the vacuum and air wavelengths for all the transitions investigated here.

Transition	Vacuum Wavelength (nm)	Air Wavelength (nm)
$3S_{1/2}$ - $3P_{3/2}$ (D_2 line)	589.158	588.995
$3S_{1/2}$ - $3P_{1/2}$ (D_1 line)	589.755	589.592

Table 7.1 - Dye Laser Wavelengths on Resonance

Transition	Vacuum Wavelength (nm)	Air Wavelength (nm)
$3P_{1/2}$ - $3D_{5/2}$	818.553	818.328
$3P_{1/2}$ - $3D_{3/2}$	818.550	818.326
$3P_{3/2}$ - $3D_{5/2}$	819.707	819.482
$3P_{3/2}$ - $3D_{3/2}$	819.704	819.479

Table 7.2 - Ti:sapphire Laser Wavelengths on Resonance for DDQ transition

Transition	Vacuum Wavelength (nm)	Air Wavelength (nm)
$3P_{1/2}-4P_{3/2}$	750.958	750.751
$3P_{3/2}-4P_{3/2}$	751.929	751.722
$3P_{3/2}-4P_{1/2}$	752.247	752.041

Table 7.3 - Ti:sapphire Laser Wavelengths on Resonance for DQD Transition

Transition	Vacuum Wavelength (nm)	Air Wavelength (nm)
$3D_{5/2}-3S_{1/2}$	342.7844	342.6864
$3D_{3/2}-3S_{1/2}$	342.7838	342.6859

Table 7.4 - Ultraviolet SFM Output for DDQ Transition

Transition	Vacuum Wavelength (nm)	Air Wavelength (nm)
$4P_{3/2}-3S_{1/2}$	330.3327	330.2379
$4P_{1/2}-3S_{1/2}$	330.3941	330.2993

Table 7.5 - Ultraviolet SFM Output for DQD Transition

In general the last two Tables are the most important for the sum-frequency experiments as the lineshapes are usually examined well away from the dye laser resonances. For the 3D-3S output the $3D_{5/2}$ and $3D_{3/2}$ lines are extremely close in zero field and in most of the experiments are well into the intermediate/strong field region where the Zeeman components of the two transitions overlap. The 4P-3S transition on the other hand is always in the weak field region during these experiments and there are always two distinct lines. In order to calculate the dye and Ti:sapphire laser wavelengths for any off-resonance position the energy conservation rule is used such that:

$$\frac{1}{\lambda_{\text{Dye(air)}}} + \frac{1}{\lambda_{\text{Ti:Sapphire(air)}}} = \frac{1}{\lambda_{\text{UV(air)}}} \quad \text{Eqn(7.1)}$$

Lineshapes and Power

In chapter 6 the theoretical lineshape of the UV output as the frequency is scanned across the 3D-3S line at different magnetic field values is predicted and shown in figure 6.13. The experimental line shape is shown in figure 7.3. For this scan the dye laser was tuned to 587.94nm, well off the D line resonances to avoid complications with having both single and two photon resonance. The beams are both 140mW in power and are focused into the oven using a 20cm lens. The oven was at 280°C.

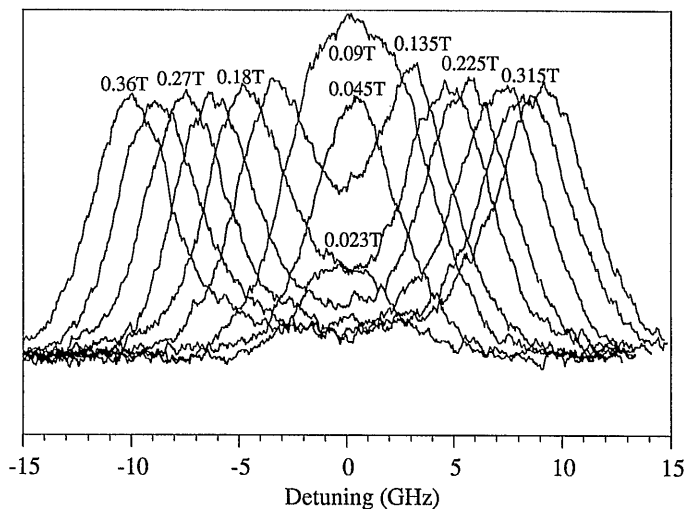


Figure 7.3 - Experimental Line Profile of $3D-3S_{1/2}$ Quadrupole transition

The experimental profile is a good fit to the theory and shows the expected behaviour of the transition in a magnetic field. The output power of the transition is proportional to the square of the product of the moments of the two dipole transitions and the moment of the quadrupole transition. The latter is directly proportional to the strength of the magnetic field for low field strengths, but when the Zeeman splitting of the transitions to the two $3S$ levels rivals their Doppler widths this relation saturates and the heights of the individual peaks is constant thereafter.

In figure 7.4 the corresponding lineshape for the DQD transition from $4P_{1/2}$ to $3S_{1/2}$ is shown for three different field strengths. This was taken at a temperature of 320°C with 130mW at 588.8nm and 50mW at 752.4nm . The figure also shows the theoretical lineshape expected for these three fields.

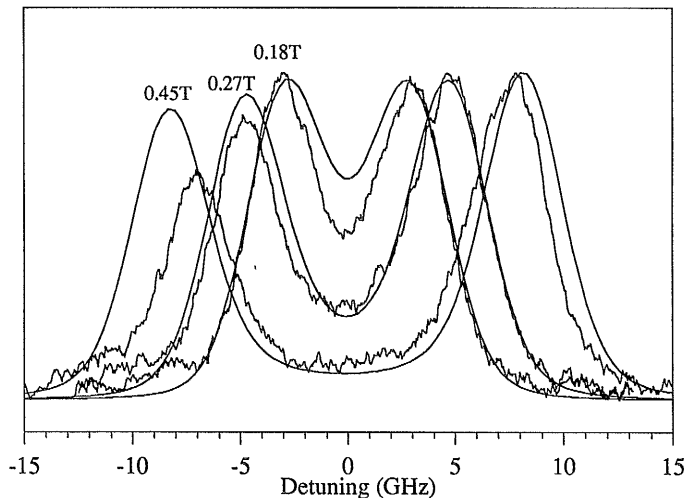


Figure 7.4 - Experimental Line Profile of $4P_{1/2}$ - $3S_{1/2}$ Dipole transition

Once more the lineshape shows the typical detuning and field characteristics. This however was only true at low temperatures unlike in the DDQ case. At higher temperatures quite drastic deviations from this classical shape appeared in the DQD profiles. These will be shown and discussed later.

The maximum output power in each of the two transitions was found to differ by about two orders of magnitude. Part of this is due to the fact that the DDQ moment product is 25 times stronger than the DQD product and part is due to the reabsorption of the dipole radiation. The $4P$ - $3S$ radiation was too low in power to be measured by our calibrated 100UV photodiode, but the $3D$ - $3S$ radiation could be easily detected. When the dye laser was tuned close to the D_2 line resonance and the powers were 140mW from the dye laser and 300mW from the Ti:sapphire laser, both focused by a 20cm lens into the oven at 300°C , the output in the UV at 342nm was optimised to a maximum of $17\mu\text{W}$. (This maximum power was obtained by balancing the benefit of tuning close to the D_2 lines against the increased absorption when close to the resonance.) This power was easily visible to the eye as a bright fluorescence spot on white card. This fluorescence is shown in figure 7.5. The figure is looking directly into the sodium oven with an UG11 filter screening out the visible and infrared and the ultraviolet showing as blue fluorescence through a white screen.



Figure 7.5 - Fluorescence of 3D-3S (DDQ) Radiation on white screen

Both routes also showed the expected linear dependence of output power on each of the two input powers. Figure 7.6 shows this dependence for the $4P_{1/2} - 3S_{1/2}$ (DQD) radiation.

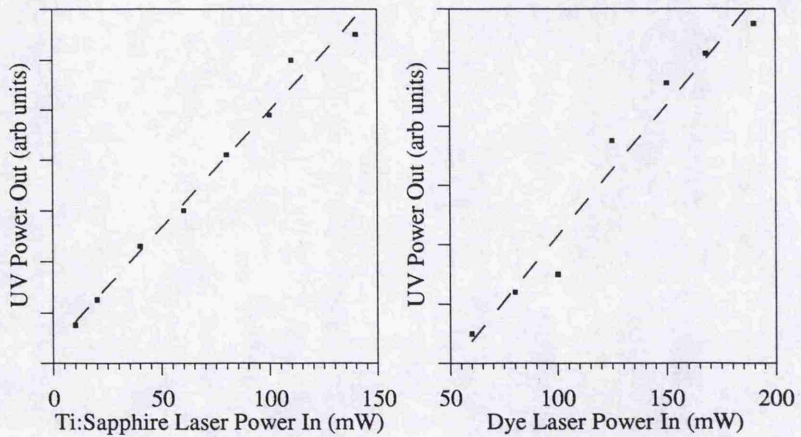


Figure 7.6 - Output Power in UV vs Input Powers (DQD Route)

The output power is also dependent both on the atomic vapour density, N , and the phase-matching of the nonlinear interaction. As the temperature of the vapour is increased both the vapour density and the refractive index of the 3S-3P transition change (the populations of all levels except the ground state are assumed to be zero so that only transitions linked to the ground state by a dipole interaction have a significant effect on the refractive index). The change in the refractive index leads to a change in the phase-mismatch, Δk , and this superimposed on the change in vapour density leads to the output power oscillating as the temperature increases. This was modelled in the last chapter and is shown in figure 6.15. Figure 7.7 shows an experimental trace of the variation of output power with temperature for an unfocused beam. The data was taken as the oven heated and is for laser frequencies such that the phase-mismatch is positive. The data was taken for a fixed dye wavelength and with the Ti:sapphire laser repetitively scanning back and forth so that the power maximum could always be found as the temperature changed. The shape of the curves was the same whether the heating occurred quickly or was done slowly enough for an equilibrium to be reached for each temperature. Each bar on the graph represents the ultraviolet lineshape in one of the Ti:sapphire laser scans.

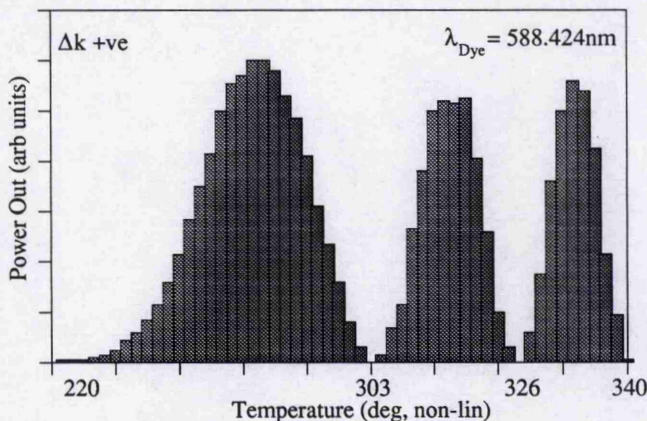


Figure 7.7 - Power vs Temperature for unfocused beam
with Δk positive on DDQ route

It can be seen that the shape of the curve is in excellent agreement with the theory with each of the peaks well defined and of roughly the same height. The slight drop in maximum power from peak to peak can be attributed to the increased absorption of the beams at higher temperatures. As the wavelength of the dye laser is tuned nearer either of the D lines the increased dispersion causes the output power to start oscillating sooner and to undergo more cycles over the same temperature range. This is shown in

figure 7.8, in which the temperature change is the same as in the previous figure but the dye laser wavelength is closer to the sodium D₂ line.

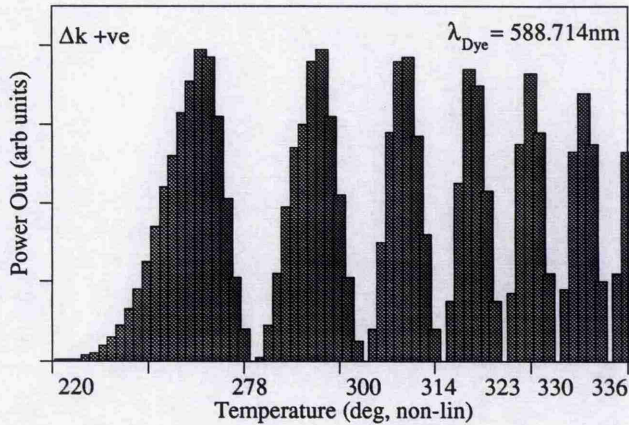


Figure 7.8 - Power vs Temperature for unfocused beam tuned nearer D₂ line

If the dye laser is tuned between the two D lines then there exists a point where the two dispersions cancel and the phase-mismatch parameter is zero. At this point the Sinc² power dependence of eqn. 6.31 vanishes and the output power of an unfocused beam no longer oscillates as the temperature is increased. Figure 7.9 shows the output power dependence of the DDQ transition when the dye laser is tuned to 589.393nm, the $\Delta k=0$ point. The first figure shows the power against temperature as the temperature was raised as high as possible. It can be seen that there is no observable tail off and the power increases in an exponential fashion. As the vapour density is not directly proportional to temperature (eqn. 6.34), the second figure shows the power dependence against the square of the calculated vapour density. This shows that up to the maximum temperature the power rises as the square of the vapour density, as expected. Although it may seem that this could allow up to 100% conversion efficiency from the vapour, the dye laser is very far from single photon resonance. Therefore the generated power levels are small compared to those when the dye laser was tuned to be close to resonance, even at the high temperatures used here. (Note: the temperature shown is that obtained experimentally from the thermostat in the oven. In general this is about 37°C less than the actual temperature in the vapour, as measured by the absorption of the dye laser when on resonance at low temperatures. The vapour densities have been amended accordingly for an offset of 37°C).

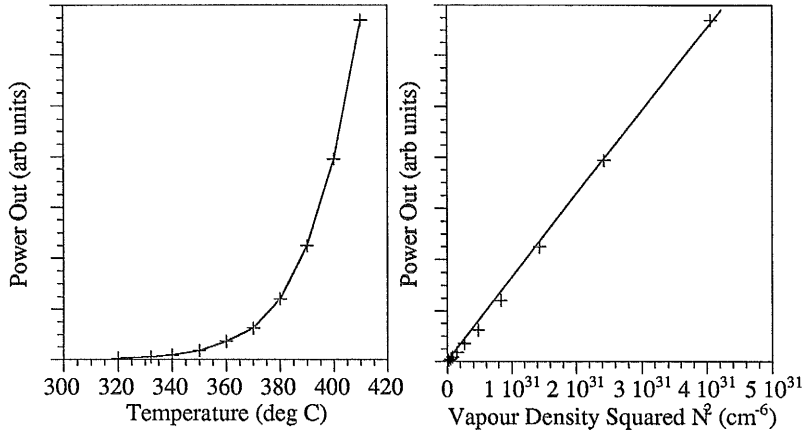


Figure 7.9 - Output Power dependence on Temperature at $\Delta k=0$

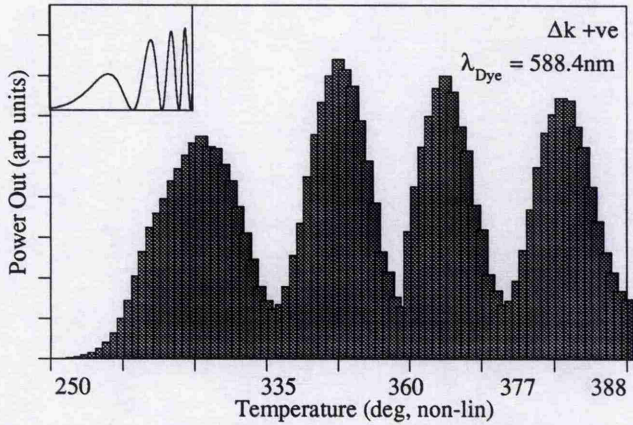
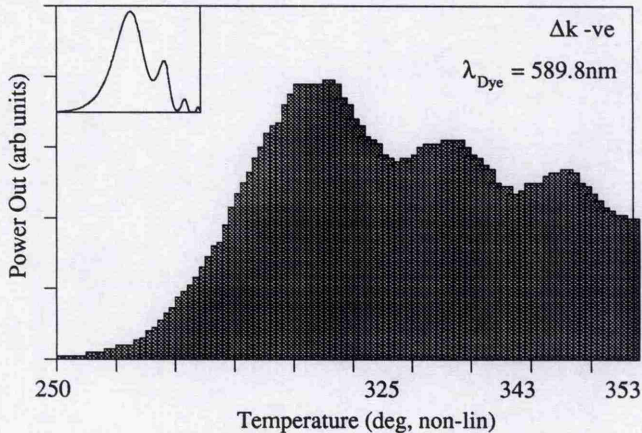
So far the lineshapes and power dependence have behaved as expected and are directly comparable to the 3S-3P-4D (DDQ) route explored in ref 1. The more interesting features appear as the temperature is raised and phase-matching begins to play a more significant part in the sum frequency process.

Phase-Matching- Focusing and Dispersion Sources

As the experiment progressed two bulk features began to stand out as deviations from the expected features. The first was observable in both routes studied and the second only occurred on the DQD route. The common linking factor was that both effects were due to phase-matching and so of particular importance in understanding nonlinear processes in vapours.

Effect of Focusing

In the previous chapter, 6, the effects of focusing the input beams were discussed and analysed with respect to the focusing parameter, ξ , and the positioning of the intermediate state by the two wavelengths. At a position in which the dispersion induced by the sodium D lines causes a positive phase-mismatch, increasing the vapour density shows that the first phase-matched peak is at a lower temperature than in the unfocused case and is smaller than subsequent peaks. In a region of negative Δk the first peak is at a higher temperature and is far larger than subsequent peaks. Figures 7.10 and 7.11 show typical traces of output power vs temperature as observed experimentally using a 20cm lens for regions in which Δk is positive or negative. In the top left hand corner of each is a trace of the expected theoretical shape.

Figure 7.10 - Output Power vs Temperature for Δk +ve with 20cm lensFigure 7.11 - Output Power vs Temperature for Δk -ve with 20cm lens

It can be seen that although the general shape of the phase-matching curves is similar to that expected theoretically there is a major discrepancy in the size of the minima. In the positive Δk region the minima were predicted theoretically to all be zero and in the negative Δk region only the first minima was expected to be non zero. Experimentally the bulk phase-matching curves never have zero minima and although the Δk +ve region always has matching curves similar to that of figure 7.10, the curves in the Δk -ve region vary wildly. The experiments described here show that there are at least 6 factors which affect the bulk phase-matching behaviour of the vapour. These are:

- a) Position of focus in vapour
- b) Strength of focus
- c) Δk value (+ve, -ve)
- d) Uniformity of vapour density in oven
- e) Collinearity of beams
- f) Radial Δk function

The two factors which don't effect the phase-matching, though they might reasonably be expected to do so are the position of the oven in the magnetic field and the dissimilarity of the confocal parameters of the two beams. The dye and Ti:sapphire laser beams have waist sizes at the focusing lens of $638\mu\text{m}$ and $913\mu\text{m}$ respectively. (Coincidentally the different waist sizes mean that the focused waists of the two beams are roughly similar - 59 and $57\mu\text{m}$ for a 20cm lens). The confocal parameters of the two focused beams for a 20cm lens are 3.65 and 2.5cm which means that the focusing parameters are 2.7 and 4 for the dye and Ti:sapphire lasers. The 20cm lens was found to give the best output power and this fits well with the predictions of Boyd and Kleinman⁶, who quote 2.8 as the optimum focusing parameter. (The next available lenses were either 10 cm or 30 cm lenses which give average ξ values of 13.4 or 1.5 as opposed to the average here of 3.35). Although it is known that different confocal parameters can enhance the output power under certain conditions⁷ this does not actually affect the shape of the phase-matching curve under the conditions used here, and the simpler model of Boyd and Kleinman is valid. The data from the Hilber paper in ref 7 and another paper by the same group⁸ were used in a more rigorous model which included the effect on the phase-matching of different focal positions within the vapour⁹. These are shown in figure 7.12 for a positive mismatch regions and in figure 7.13 for a negative mismatch region. The figures marked in the top left hand corner of each graph are the distances of each of the foci from the centre of the oven. The calculations are all for a 20 cm focal length lens.

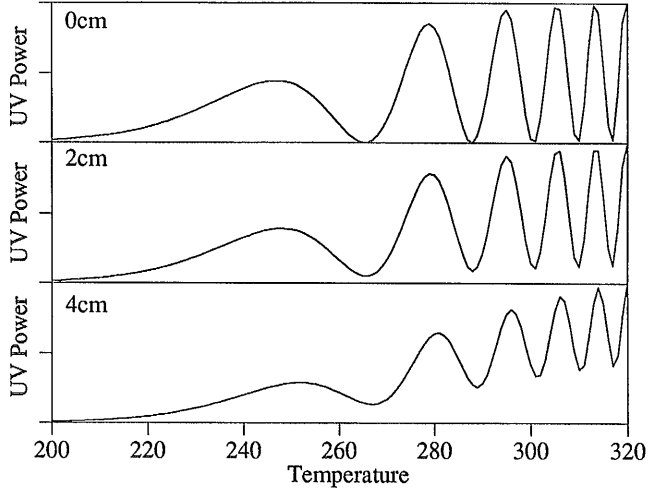


Figure 7.12 - Theoretical Calculation of Effect of Displacing the Beam Waists from the Centre of the Oven on the Phase-matching Curves for a $\Delta k + ve$ region

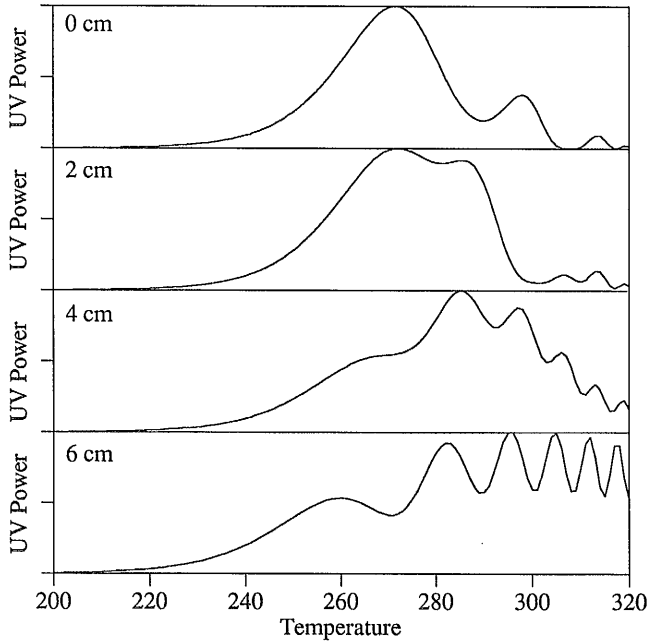


Figure 7.13 - Theoretical Calculation of Effect of Displacing the Beam Waists from the Centre of the Oven on the Phase-matching Curves for a $\Delta k - ve$ region

These theoretical curves tie in well with the experimental results. The Δk +ve curves are all similar in shape but with minima larger and larger the further the focus is from the central position. Given that the focusing lens was usually positioned to an accuracy of roughly 1 cm it is not surprising that the experimental minima are never zero. However it cannot be the sole cause of the distorted phase-matching curves because the figure of 7.10 appears to have larger minima than would be expected from a displacement of 2 cm or less but not the increasing peak sizes which would be associated with a larger displacement. (It is also very unlikely that one could misjudge a length by 4 cm, even using a cm ruler.) The effects of different focal positions is most apparent in the Δk -ve curves. The corresponding experimental curves are shown in figure 7.14. These were taken with a 20cm lens and the lengths marked are the distances of the lens from the centre of the oven.

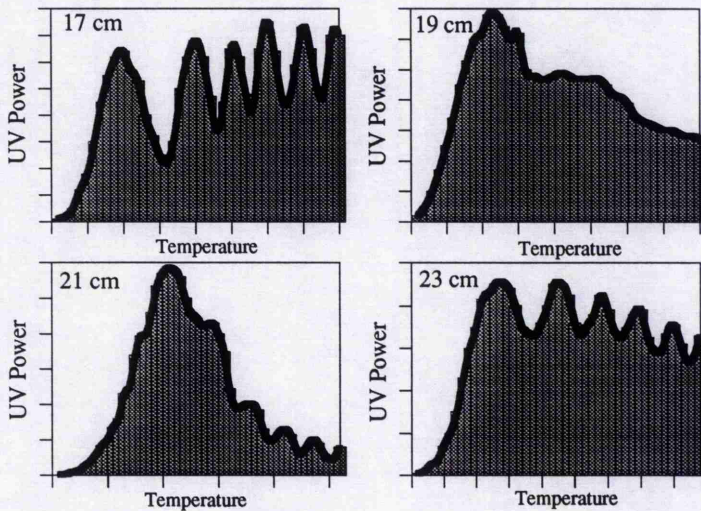


Figure 7.14 - Experimental Effect of Displacing a 20cm Lens from the Centre of the Oven on the Phase-matching Curves for a Δk -ve region

It is apparent once more that the shapes are very similar to those expected from theoretical considerations but at no time do the curves equal that expected for a 0 cm displacement, with that for a 21cm displacement being the closest. There is also no focal position which gives the very lumpy shape seen for a 19cm displacement, and this is the shape often seen for regions of negative dispersion. Changing the focal position is, however, a very significant part of the general phase-matching behaviour.

Two of the other factors which affect the phase-matching, which have already been discussed, are the strength of the focusing into the vapour and the sign of the Δk

mismatch. In the positive dispersion region, as mentioned before, the shapes of the curves both theoretically and experimentally do not alter much with increased focusing. In the negative dispersion region the expected shapes differ quite radically with increasing values of ξ , and these are shown in figure 7.15 for ξ values of 1, 2, 3 and 4.

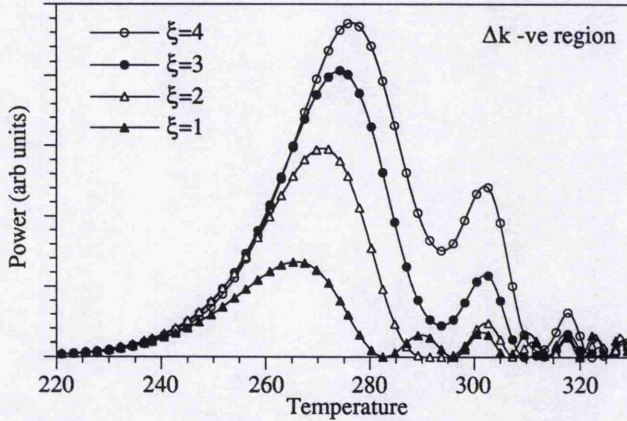


Figure 7.15 - Theoretical comparison of Phase-matching curves for different values of the focusing parameter, ξ , in the Δk -ve region

The experimental curves of phase-matching for lenses of 30cm and 40cm are shown in figure 7.16.

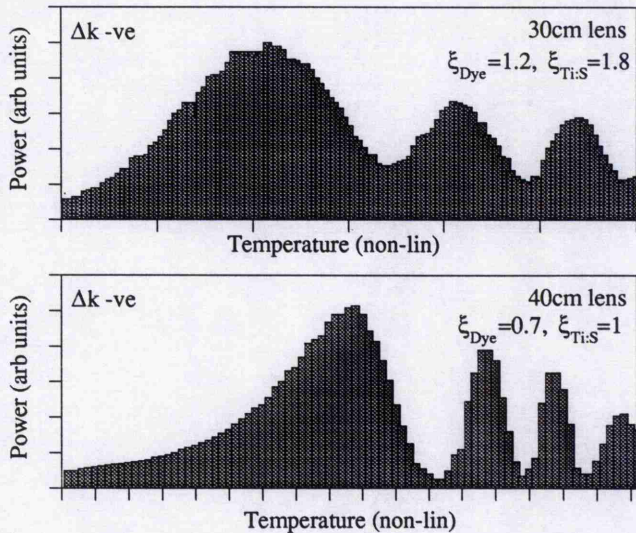


Figure 7.16 - Experimental variation of phase-matching curves with ξ

As expected, the longer the focal length of the lens the more the shape starts to resemble the unfocused case. The minima become more defined and the secondary peaks become larger. Although neither trace is exactly as expected they do show the evolution from focused to unfocused.

The effect of the vapour density along the length of the oven is analogous, though naturally of far less importance, than the position of the focus. If the oven undergoes rapid heating, as in most of the traces shown here, then the vapour density will vary along the oven as the hot vapour in the centre migrates to the cooler edges. If this variation was exactly symmetrical and the focus was exactly in the centre of the oven then no effect would be expected, but if the focus is slightly shifted then a slight increase in the blurring effect can be expected. Figure 7.17 shows traces for the two dispersion regions with the temperature allowed to reach equilibrium at each stage.

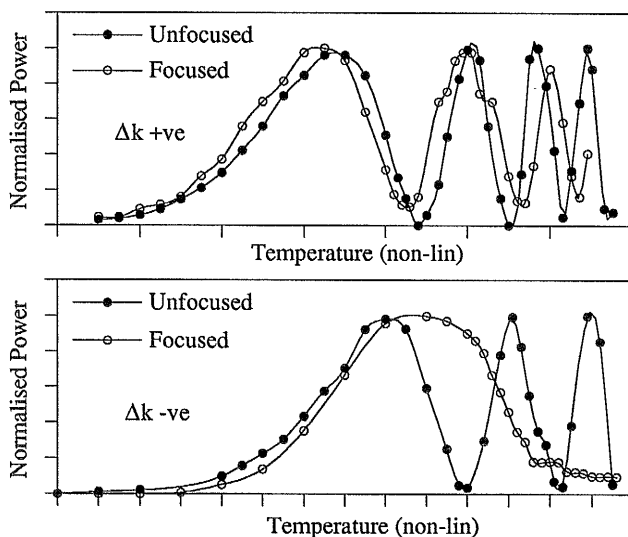


Figure 7.17 - Contrasting Unfocused and Focused Behaviour for Positively and Negatively Dispersive Vapour Regions taken with Temperature always at Equilibrium

The $\Delta k +ve$ region does show better minima than in figure 7.10 but the $\Delta k -ve$ region is still very blurred. These traces do however show the expected displacement of the first maxima in the focused as opposed to the unfocused cases - down for $\Delta k +ve$ and up for $\Delta k -ve$.

The last major influence on the phase-matching was not expected from any theoretical treatment so far seen for frequency mixing in vapours. This was the observed strong radial dependence of the SF power. The model based on references 7 and 8 predicts a near Gaussian output in which the whole profile varies with the

expected total power output. This is in agreement with the calculations of Hilber et al (ref 7) in which the only change from this type of profile is for DFM in a positively dispersive medium. For SFM the output should always be strongest in the centre and falling off to the sides. This is in direct contrast to the behaviour seen experimentally. Figures 7.18 and 7.19 show the SF output as observed by a CCD camera. The dye wavelength is well off D line resonance so that there is no self focusing or defocusing and both the visible and IR wavelengths have been filtered from the output.

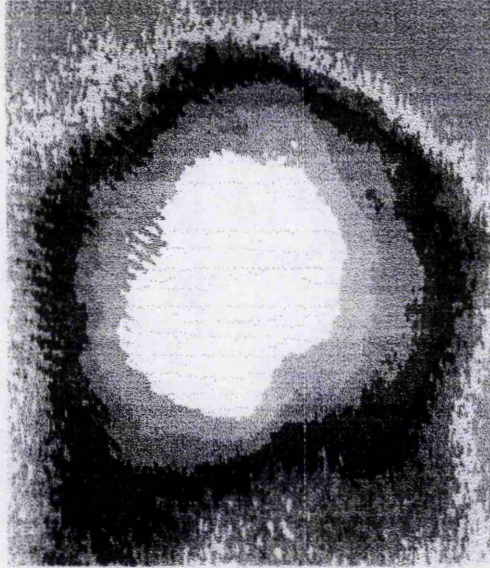


Figure 7.18 - UV Output at Vapour Temperature Before First Phase-Matching Peak

Figure 7.18 shows the output power in the UV when the vapour temperature is below the first phase-matching peak. As expected theoretically the beam profile is near Gaussian with the most intense part of the beam represented by the bright circle in the centre of the beam. As the temperature is raised past the first phase-matched peak the intensity in the centre increases and the central spot expands, then the outer part of the centre spreads outwards and creates a secondary ring around the centre. As the temperature is raised still further this ring continues to expand outwards and a second subsidiary ring breaks away from the centre in the same manner as the first. The outer rings decrease in intensity the further they are from the centre and the maximum seen was two at once. Figure 7.19 shows the SF output at a temperature well above the first phase-matching peak. The ring structure is clearly visible with one subsidiary surrounding the centre maximum.

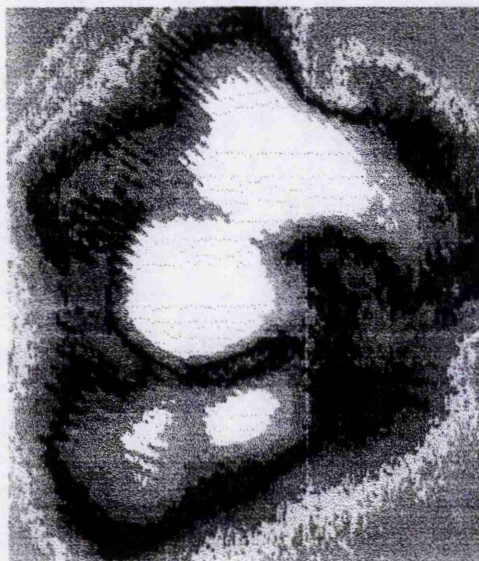


Figure 7.19 - UV Output at Vapour Temperature After First Phase-matching Peak

These figures show an apparently symmetric radial Δk function across the SF beam, causing parts of the beam to be phase-matched while others are not. If the beams are misaligned with respect to one another then the ring structure changes to a set of fringes in the plane in which the beams have been misaligned. Non-collinear phase-matching can be expected if the beams are misaligned, but this is a relatively small effect and no output was seen in the absence of a magnetic field. Also, if it were just a non-collinear effect then it should also appear when the beams are unfocused, which it does not. The behaviour at any one position across the beam profile was examined by looking at the output through a pinhole. In figure 7.20 the output is examined through a $25\mu\text{m}$ pinhole when a 20cm lens is used to focus into the vapour. The upper trace is for a position near the edge of the beam and the lower for a position nearer the centre. The behaviour in the centre of the beam was (even with a $25\mu\text{m}$ pinhole) similar to that of the beam as a whole and in this case looked like figure 7.11. There are two obvious trends from the two scans. The first is that the minima occur at different temperatures, partly accounting for the blurring of the trace as a whole, and the second is that the further away from the centre the pinhole is placed the less focused that part of the beam appears to be.

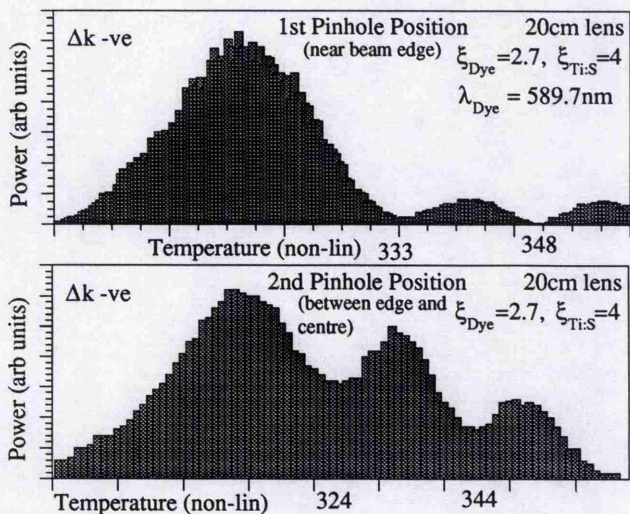


Figure 7.20 - Variation of Output with Temperature at Different Positions from Beam Centre

Although this radial behaviour was not expected by the modelling used in this work it was clearly not an experimental fluke as it was always present and evidence of the same behaviour can be seen in ref 1. One possible explanation is that the beams themselves are astigmatic, but when a curved mirror at an angle was used to gently focus the dye laser beam ($f=1\text{m}$), thereby introducing noticeable astigmatism, the behaviour was not markedly different. It seems more probable that the radial distribution is fundamental with the focusing of two different beams in the vapour and that a complete theoretical understanding of the experimental behaviour of phase-matching in vapours needs to include not only focusing strength and position but non-collinear beams and a varying vapour temperature in the oven. This was not attempted here but is a possible basis for future work.

Dispersion on Sum Frequency Route

The second bulk phase-matching feature which was not originally expected was encountered in the line profile of the DQD route. This is shown in figure 7.21 where the line profile as the dye laser is tuned across the $4P_{1/2}$ - $3S$ transition is shown for two different detunings of the laser from single photon resonance.

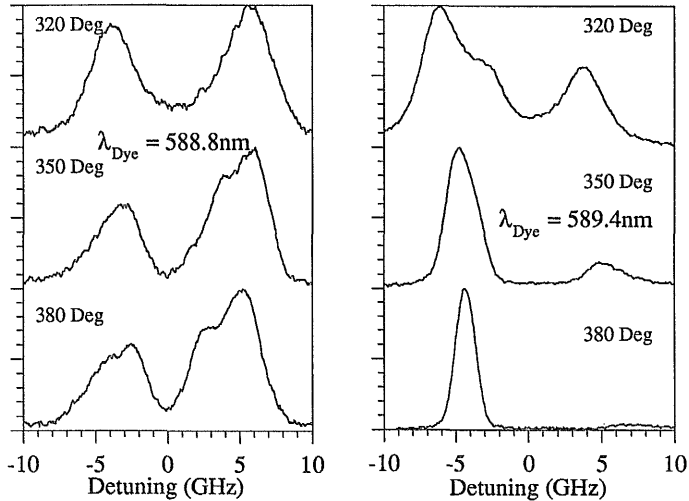


Figure 7.21 - $4P_{1/2}$ - $3S$ Lineshape for Different Detunings from Intermediate D line Resonances, Field = 0.27T

The figure shows the lineshape of the UV output at a field strength of 0.27T for three different vapour temperatures and two different values of detuning from the D line resonances. It can be seen that in each picture there is a marked tendency as the temperature is increased for one of the two lines to predominate. In all of the experiments undertaken at different detunings from single photon resonance the same pattern is repeated. It is however not always the same line that dominates, nor, as can be seen in the figure, does the ratio of the peak heights stay even remotely constant even at the same temperature.

On closer examination of the dispersion across the line the reason for the change becomes clearer. In Chapter 6 the phase-mismatch, Δk , caused by the dispersion of the 3P lines is shown in figure 6.14 and that caused by the 4P lines in figure 6.15. For the DDQ route only the first dispersion source is present and all lineshapes resemble that shown in figure 7.3, where the phase mismatch, Δk is constant as the tuning laser is scanned across two photon resonance. (This is only true if the tuning laser is not scanning through single as well as two photon resonance. In the latter case the lineshape is severely distorted as the different routes from the lower to the upper level through the D lines assume greater or lesser enhancement as the laser is tuned through the resonance of each. All of the lineshapes looked at here are at detunings far off single photon resonance as are the theoretical models.)

For the DQD route however both dispersion sources are present. The dispersion of the 3S-3P transition must be added to that of the 4P-3S lines. This addition of dispersions spoils the previously symmetric dispersion profile shown in figure 6.16. To add to the complications, not only does the phase-mismatch vary as the tuning laser is tuned across two photon resonance but the single dispersion source of the $4P_{1/2} - 3S$ transition splits into two dispersion sources as the magnetic field is raised. The variation of the overall phase-mismatch as the laser is tuned across two photon resonance for a magnetic field value of 0.27T is shown in figure 7.22. Each figure covers a wavelength range equivalent to about 60GHz around the $4P_{1/2} - 3S$ line and represents a different value of detuning from single photon resonance (hence a different contribution to the overall phase mis-match from the dispersion on the 3S-3P transition). Unlike figure 6.16 the calculations of the dispersion across the $4P_{1/2}$ lines have been modified to include a damping term which represents the Doppler broadening of the peaks.

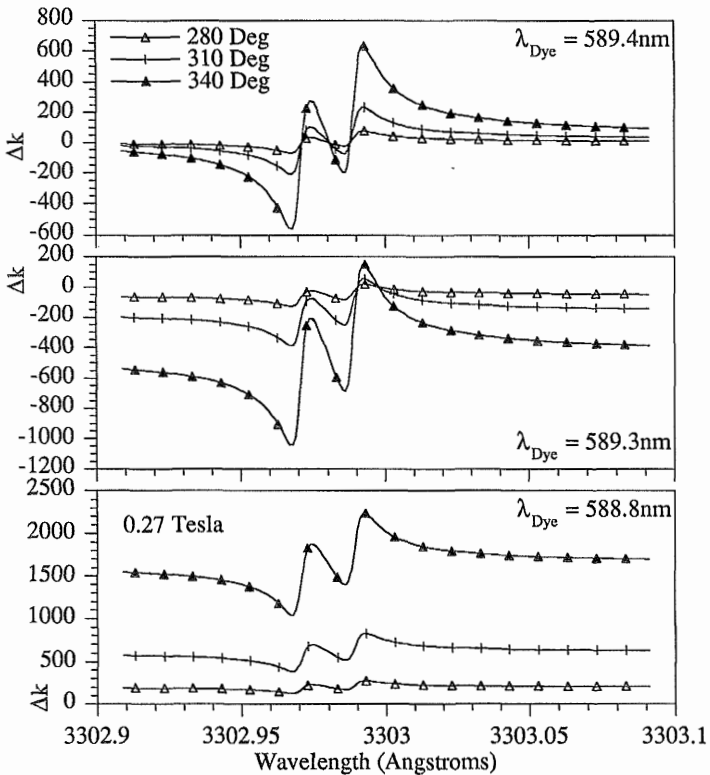


Figure 7.22 - Effect of Dispersion of 3S-3P Route on Phase-Mismatch in 4P-3S Route at a field of 0.27T

It can be seen that as the tuning laser is tuned across two photon resonance with the $4P_{1/2}$ line the phase-mismatch varies widely, and in fact the transition passes through many phase matching cycles. The higher the vapour temperature the greater this variation is as the laser is tuned. It is this variation of phase matching across the Zeeman split line which causes the power in one peak to be preferentially phase-matched while the other is less so. In some cases this variation of phase-matching leads to the appearance of three or four peaks in the line profile as the sides of the two main lines are preferentially phase-matched above the middle. Traces of this kind of behaviour can be seen in figure 7.21. Even at the supposedly $\Delta k=0$ point, ($\lambda_{dye} = 589.393\text{nm}$), where the dispersion curve is exactly symmetric about line centre, phase matching effects were observed. As the experiments were usually conducted by tuning the laser frequencies to maximise the power before taking a scan, it is probable that at the nominal $\Delta k=0$ position the laser frequency has been optimised to be slightly to one side or the other. The first two curves of fig 7.22 show that even at 0.1nm away from the $\Delta k=0$ point the phase-matching has changed dramatically as the tuning laser is scanned over two-photon resonance.

Conclusion

This chapter has examined two contrasting routes for sum frequency generation in sodium vapour, one involving quadrupole emission on the 3D-3S transition and the other dipole radiation on the 4P-3S transition. It was found that the route involving the quadrupole emission was the best in terms of radiated power, generating $17\mu\text{W}$ at 342nm. The difference in the generated powers was in line with that expected from the product of the transition moments. In addition, the factors affecting phase-matching on the two routes were studied, with emphasis on the experimental variables which govern the behaviour of phase-matching in a focused sum-frequency interaction. The differences in emission lineshape due to having two dispersion sources in the interaction are shown and discussed in terms of the variation in phase-mismatch across the line profiles at different detunings from single-photon detuning and different vapour temperatures.

References

- 1 A J Poustie - Magnetic field Induced Sum Frequency Mixing in Sodium Vapour - Ph. D Thesis, St. Andrews University, 1990
- 2 B D Sinclair - Second Harmonic Generation in Sodium Vapour Induced by a Magnetic Field- Ph. D Thesis, St. Andrews University, 1987
- 3 D M Kane - Atomic Laser Spectroscopy in the UV and Visible - Ph. D Thesis, St. Andrews University, 1983
- 4 Spectra-Physics Model 380D Frequency Stabilised Dye Laser - Instruction Manual, Spectra Physics Publications Ltd., California,
- 5 Handbook of Chemistry and Physics - CRC Press - 53rd Edition, Chemical Rubber Publishing Company, USA, 1973
- 6 G D Boyd and D A Kleinman- Parametric Interaction of Focused Gaussian Light Beams- J.App.Phys, 39, 1968, pgs 3597-3639
- 7 G Hilber et al - Optical frequency conversion in gases using Gaussian laser beams with different confocal parameters - Phys Rev A, vol38, number 12, pgs 6231-6239, 1988
- 8 A Lago et al - Optical -Frequency Conversion in Gaseous Media - Phys Rev A, Vol. 36, number 8, pgs 3827 -3836, 1987
- 9 Program Courtesy Mr R Moseley

Conclusions

The work described in the previous chapters looks at ways to develop the cw Ti:sapphire laser as a spectroscopic tool, and shows the use of this laser in exploring some of the atomic excitation routes within Sodium vapour.

As there are to date few tunable sources of coherent radiation in the blue/green part of the spectrum, stable high power frequency doubling of the Ti:sapphire laser offers the possibility of covering the previously difficult to obtain range of wavelengths between 350nm and 500nm. In Chapter 4 there is an account of the intracavity cw doubling of a Ti:sapphire laser using the nonlinear crystal potassium niobate (KNbO_3). potassium niobate has been a very promising new nonlinear material, as it has one of the largest effective nonlinear coefficients in the near infrared, at 20.8pm/V. It is also capable of being temperature as well as angle tuned, which allows a range of wavelengths to be doubled by using only one cut of crystal instead of the series of crystals needed when using angle tuned crystals. The experiments describe a relatively simple method of adapting the cavity for intracavity doubling to attain maximum powers of 50mW at 430nm. The efficiency of the process per Watt was constant over the entire tuning range from 860nm to 905nm, and the tuning range was only limited by the reflectivity of the mirrors. Using this method it should be possible with the correct mirrors to extend the tuning range to ~970nm. The limitations of the system are the low damage threshold in potassium niobate, which limits the extent to which the fundamental can be focused, and the poor thermal qualities of the crystal. These thermal properties have been investigated, and were found to be the main cause of power fluctuations in the second harmonic. This arises from the narrow thermal bandwidth of the crystal, which requires stabilisation to less than a hundredth of a degree to limit fluctuations in the phase-matched wavelength. The low thermal bandwidth was also responsible for thermal phase-mismatching within the crystal, in which the absorption of the fundamental itself leads to a temperature change across the profile of the beam. As a point of general interest in the use of temperature tunable birefringent crystals for intracavity doubling of ring cavities, the effects of temperature changes in the crystal on the preferred direction of lasing within the cavity were noted. It was found that the rotation of the fundamental polarisation by the nonlinear crystal was sufficient to counteract the effects of the optical diode and switch the direction of lasing. This was attributed to changes in the optical length of the crystal as the temperature was varied causing the crystal to act as a variable waveplate.

Chapter 5 examines ways to stabilise the Ti:sapphire laser to sub-MHz noise levels. For any spectroscopic study the resolution of the experiment is limited by the noise levels of the laser. Reducing these noise levels requires both passive and active stabilisation. The laser used in these experiments was initially stabilised to noise levels of about 5 MHz using passive stabilisation techniques. These noise levels were then further reduced by use of a 'side of fringe' locking scheme, in which an external confocal Fabry-Perot etalon was used as the discriminator. The frequency deviations were fed back to the Ti:sapphire laser cavity as corrections to the cavity length. Slow but large frequency changes were corrected by two Brewster-angled tilt plates while fast but smaller frequency corrections were made via a piezo mounted mirror. Using a simple self built electronic servo system the active stabilisation reduced the laser noise to 550kHz. This chapter also examined means of obtaining a 30 GHz frequency scan of the laser output and concluded that although 'dead reckoning' schemes will give scans of approximately 10GHz, the only method of obtaining reliable 30GHz scans is to use some form of dither and lock scheme to keep the resonance frequency of the etalon centred over the scanning laser mode.

In Chapter 7 is presented work on sum-frequency generation in sodium vapour. This work has produced what is to our knowledge the largest output power from a quadrupole transition via sum-frequency mixing. The experiments looked at two contrasting routes for sum-frequency generation in a vapour using both a Ti:sapphire and a dye laser. The first route used two dipole transitions in the upward route and a quadrupole transition on the return route, 3S-3P-3D-3S (DDQ route), while the second used both a dipole and a quadrupole transition on the upward route and a dipole transition on the return route, 3S-3P-4P-3S (DQD route). It was found that although the ratio of maximum output powers obtained from each route was in line with the product of their transition moments, they exhibited wildly different line profiles as the vapour temperature was increased. The line profiles of the DDQ transition were always in good agreement with theory but those of the DQD route were severely distorted. This was due to the additional dispersion source from the 4P-3S transition on the DQD route, which, in combination with the dispersion on the 3S-3P transition which is present in both routes, causes the phase-matching on the DQD route to have a number of different values as the tuning laser is tuned across two photon resonance. This variation of phase-matching means that the expected Zeeman-split two lobed line profile is often distorted, with one of the lines being preferentially phase-matched and dominating the line profile.

In addition the experiments on sum-frequency generation looked at the overall phase-matching behaviour as the vapour temperature was varied and identified at least six variables which affect the bulk phase-matching behaviour. Each of these variables was shown or discussed and one of them was found to be outside the parameters of any

current theoretical model. This factor was a radial variation in phase-matching across the beam profile, which appeared as the vapour temperature was increased, and is affected both by the focusing strength of the fundamental beams and by their orientation with respect to each other.

The origin of this radial phase-matching effect, which could be due to either radial temperature variations in the vapour or a mixture of non-collinear phase-matching and focusing effects, or all three together is a possible basis of some future work. Of more immediate interest is the use of the two laser, atomic vapour system used in the sum-frequency experiments to investigate the growing field of electromagnetically induced transparency (EIT). In recent years there have been a number of theoretical papers on setting up atomic coherences within a three level system, in which a very strong coupling field between two levels can interfere destructively with the absorption between two adjoining levels. This is particularly relevant in the work discussed here, in which the maximum powers available always involve a compromise between tuning close to the enhancement of single photon resonance and the increased absorption of the dye laser beam as it is tuned close to the enhancing resonance. The theory of electromagnetically induced transparency raises the possibility of increasing the sum-frequency powers obtained here by reducing the absorption of the dye laser radiation on resonance, while still keeping a strong second order nonlinearity¹.

Reference

- ¹ R R Moseley, B D Sinclair and M H Dunn - Enhanced conversion efficiency in three wave mixing via electromagnetically reduced fundamental wave absorption - Opt. Comm., Vol. 101, No. 3,4, pgs 139-143, 1993